UNIVERSITÀ DEGLI STUDI DI PADOVA

Dipartimento di Fisica e Astronomia "Galileo Galilei"

Master Degree in Physics

Final Dissertation

Investigating the binary neutron star merger event GW170817 via general relativistic magnetohydrodynamics simulations

Thesis supervisor

Dr. Riccardo Ciolfi

Thesis co-supervisor

Dr. Jean-Pierre Zendri

Candidate

Massimo Griggio

Academic Year 2018/2019

Abstract

Magnetohydrodynamics simulations performed in full general relativity represent the ideal tool to unravel the dynamics of binary neutron star (BNS) mergers as well as the post-merger evolution of the resulting remnant object. This approach allows us to study in particular (i) the magnetic field amplification and the possible formation of collimated relativistic outflows or jets, which is fundamental to make the connection with the resulting short gamma-ray bursts (SGRBs), (ii) the associated gravitational wave (GW) emission, and (iii) the properties of the massive and metastable neutron star remnant before it eventually collapses into a black hole (BH), depending on the properties of the progenitor binary system. In this Thesis we carry out this type of investigation for two models (with mass ratio $q = 0.9$ and $q = 1.0$) consistent with the observed properties of GW170817, the first BNS merger observed in GWs by the Advanced LIGO and Virgo interferometers. Specifically, we use the Lorene code to build the initial data for an irrotational BNS model with the same total mass of GW170817, where we employ the APR4 equation of state for the description of matter at supra-nuclear densities. We further assume a high initial magnetization corresponding to a maximum magnetic field strength of 5×10^{15} G. This system is then evolved up to merger and beyond with the numerical relativity evolution codes Einstein Toolkit and WhiskyMHD. Our results provide important hints for the interpretation of the multi-messenger observation of this breakthrough event.

Contents

List of Figures

1 Introduction

On August 17, 2017 the LIGO-Virgo interferometers observed a gravitational wave signal (GW170817), while a gamma-ray burst (GRB 170817A) was observed independently by the Fermi Gamma-ray Burst Monitor. An extensive observing campaign was launched across the electromagnetic spectrum leading to the discovery of a bright optical transient (AT2017gfo) in the galaxy NGC 4993 less than 11 hours after the merger. These observations support the hypothesis that GW170817 was produced by the merger of two neutron stars followed by a short gamma-ray burst and a so-called kilonova powered by the radioactive decay of r-process heavy nuclei synthesized in the material ejected during the merger process. Combining gravitational and electromagnetic signals, this event is not only the very first binary neutron star merger gravitational wave observation in history but also the first multi-messenger observation of a gravitational wave source.

Binary neutron star mergers have in fact always been the most prominent candidate for a multi-messenger observation. These systems provide a very rich laboratory to study physics at energies and conditions that are not reproducible on Earth. The coalescence of two neutron stars, differently from two black holes, is expected to produce strong electromagnetic counterparts to the gravitational wave signal. An electromagnetic counterpart is of fundamental importance, beside the fact that it allows for further tests of general relativity, as it let us infer key independent information on the properties of the binaries and of the remnant.

The detector network is growing fast, both in the number of detectors and in the sensitivity, and this will allow for more and more precise observations. The expected binary neutron star merger detections per year are expected to increase from the current 2^{+8}_{-2} to 8^{+42}_{-7} just with the addition of the KAGRA interferometer to the Advanced LIGO and Virgo network.

However, even if this event is a great breakthrough, there are still open questions. As an example, from GW170817 we finally managed to see the long awaited smoking gun of the connection between compact binary mergers and short gamma-ray bursts, but the mechanism through which a relativistic jet can be launched is still unclear. Moreover, the impossibility to directly test the behaviour of matter at supra-nuclear densities on Earth leaves the equation of state for neutron stars unknown. New observations will help to shed some light on these unresolved questions, and now more than ever we need theoretical models and simulations as they represent the most powerful tool to study the dynamics of these catastrophic events.

In this work we perform binary neutron star merger simulations of a system with properties consistent with those of GW170817. We consider two cases, one with equal masses and one with different masses of the two neutron stars composing

the binary. These simulations are performed in full general relativity, taking into account magnetohydrodynamics and thus including the key role of magnetic fields. The systems are evolved up to about 60 ms after the merger.

The Thesis is organized as follows. We start with a brief introduction to the physics of binary neutron star mergers, focusing on the expected signals. In particular, we will describe the gravitational wave emission, the short gamma-ray bursts and their candidate central engines, and the kilonova. We will then discuss the GW170817 event and its electromagnetic counterparts. After that we will review some important concepts on numerical relativity, describing the formalism that is employed in the codes we used and the numerical methods adopted. The models setup, the parameters that we set and the tools we used to build the initial conditions will follow. Lastly, we will present and discuss the results of the simulations.

2 The physics of binary neutron star mergers

2.1 Neutron stars

Neutron stars (NSs) are compact objects in which the degeneracy pressure provided by neutrons prevents the collapse into a black hole (BH). The idea of a neutron star was first proposed by Baade and Zwicky in 1934 [1], but was mostly ignored until 1967, when Bell and Hewish observed [2] a repeating signal at a fixed point in the sky. The signal was explained to be generated by a rotating NS (pulsar) by Gold and Pacini [3, 4]. This collimated emission is due to very strong dipolar magnetic fields ($B \sim 10^8 - 10^{15}\,G$) which characterize these objects. NSs have densities as high as $\sim 10^{15}\,g/cm^3$, and are formed by core-collapse of massive stars, but their radius is much smaller ($\sim 10\,km$) than an ordinary star.

Compact objects, and more generally static spherically symmetric bodies in general relativity, are described by the Tolman-Oppenheimer-Volkoff equation. From Einstein's equations[1]

$$R_{\mu\nu} - \frac{1}{2} g_{\mu\nu} R = 8\pi T_{\mu\nu}, \tag{2.1.1}$$

with

$$T^{\mu\nu} = (p + \rho)\, u^\mu u^\nu + p g^{\mu\nu} \tag{2.1.2}$$

the stress-energy tensor of a perfect fluid, p being its pressure, ρ its density and u^μ its four-velocity, and assuming a static, spherically symmetric metric, one can find [5, 6]

$$\frac{dm}{dr} = 4\pi r^2 \rho \tag{2.1.3}$$

and

$$\frac{dp}{dr} = -\frac{\rho m}{r^2}\left(1 + \frac{p}{\rho}\right)\left(1 + \frac{4\pi p r^3}{m}\right)\left(1 - \frac{2m}{r}\right)^{-1}. \tag{2.1.4}$$

The function $m(r)$ is the total mass inside the radius r. Equation 2.1.4 is known as the Tolman-Oppenheimer-Volkoff (TOV) equation and describes a spherical symmetric body in hydrostatic equilibrium.

In addition to the TOV equation we need an equation of state (EOS), to relate pressure and density (i.e. $p = p(\rho)$). For matter up to $\rho = \rho_d = 4 \times 10^{11}\,g/cm^3$ the properties of matter can be determined directly from experiments. As ρ increases, inverse β-decay becomes more efficient, and neutrons are produced in large number,

[1] we will adopt a geometrized unit system, where $G = c = 1$.

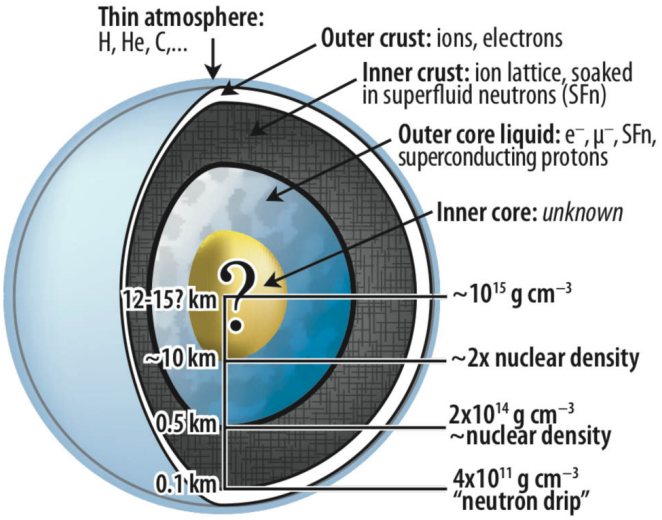

Figure 2.1: Neutron stars internal structure. [7]

while the associated neutrinos leave the star. When ρ reaches ρ_d, there are no more free energy levels available for the neutrons, that must then drip out from the nuclei, forming a neutron gas. This process is called neutron drip. For densities $\rho_d < \rho < \rho_0 = 2.67 \times 10^{14}\,\mathrm{g/cm^3}$, models of the EOS are based on extrapolations of the available empirical data, as the extremely neutron rich nuclei are not observed on Earth. For densities above the nuclear density ρ_0, there is no data available, and we must rely on theoretical models. The study of NSs systems in fact offers a unique opportunity to test these models thus shedding some light on the properties of matter at supra-nuclear density.

Employing different EOSs in the TOV equation we get different models of for the interior structure of the NS. The EOSs can be divided into soft, moderate and stiff; an EOS with higher pressure for a given density is said to be stiffer, while the opposite is deemed as softer. A stiff EOS will generate a NS with larger radius and lower central density as compared to a soft EOS with the same total mass.

2.1.1 Internal structure

The structure of a NS will depend on the EOS we adopt, but in general it can be described as a series of layers with different composition and thickness. We can see an illustration of these layers in Figure 2.1. Starting from the exterior we find:

- *the surface*, with densities of the order of $10^6\,\mathrm{g/cm^3}$, a region in which the temperatures and the strong magnetic fields can significantly affect the EOS;

- *the outer crust*, with densities up to the neutron drip density ρ_d. This is a solid region where a lattice of heavy nuclei coexists in β-equilibrium with a degenerate electron gas;

- *the inner crust*, with densities from ρ_d to the nuclear density ρ_0. In this layer we find a lattice of proton-rich nuclei together with a neutron gas and an electron gas;

- *the outer core*, with density between ρ_0 and $\rho_{\rm core}$. This region is far above the neutron drip, so it contains mainly free neutrons, with a smaller concentration of protons and electrons;

- *the core* is a region with density $\rho = \rho_{\rm core} \sim 10^{15}\,{\rm g/cm}^3$. The physics of the core is unclear and what lies in this region is still an open question. Such extremely high densities may lead to the formation of hyperons, bosons condensates and deconfined quark matter.

2.2 Binary neutron stars

The most promising scenario for a multi-messenger observation is a binary neutron star (BNS) merger. A BNS is a system of two NS orbiting around their centre of mass. The coalescence of such a system would generate a wide range of signals as gravitational waves, electromagnetic emission and neutrinos. As we already anticipated, NSs are the endpoint of the evolution of massive stars. In particular, the fate of a star depends on its mass: for masses $8\,M_\odot \lesssim M \lesssim 25\,M_\odot$ the star will undergo a supernova explosion, possibly leaving a NS remnant. In this section we are interested in the evolution of BNS system from its formation to the merger.

2.2.1 Formation channels

The standard formation channel for a BNS system is illustrated in Figure 2.2. We start from a system composed by a massive couple of stars (both with masses between $8-25\,M_\odot$ to ensure a pair of supernovae). The heavier one evolves reaching its giant phase and finally undergoes a Type Ib, Ic or II supernova, leaving behind what will become a NS. If the system is not destroyed by the explosion, the second star evolves in turn overflowing its Roche lobe. The first NS starts accreting matter from the companion and later a common envelope phase can be established, if the mass is transferred too fast to be accreted. Dynamical friction dramatically shrinks the binary separation, until sufficient energy is released to expel the envelope. Without this step the separation would be too wide to lead to a merger within

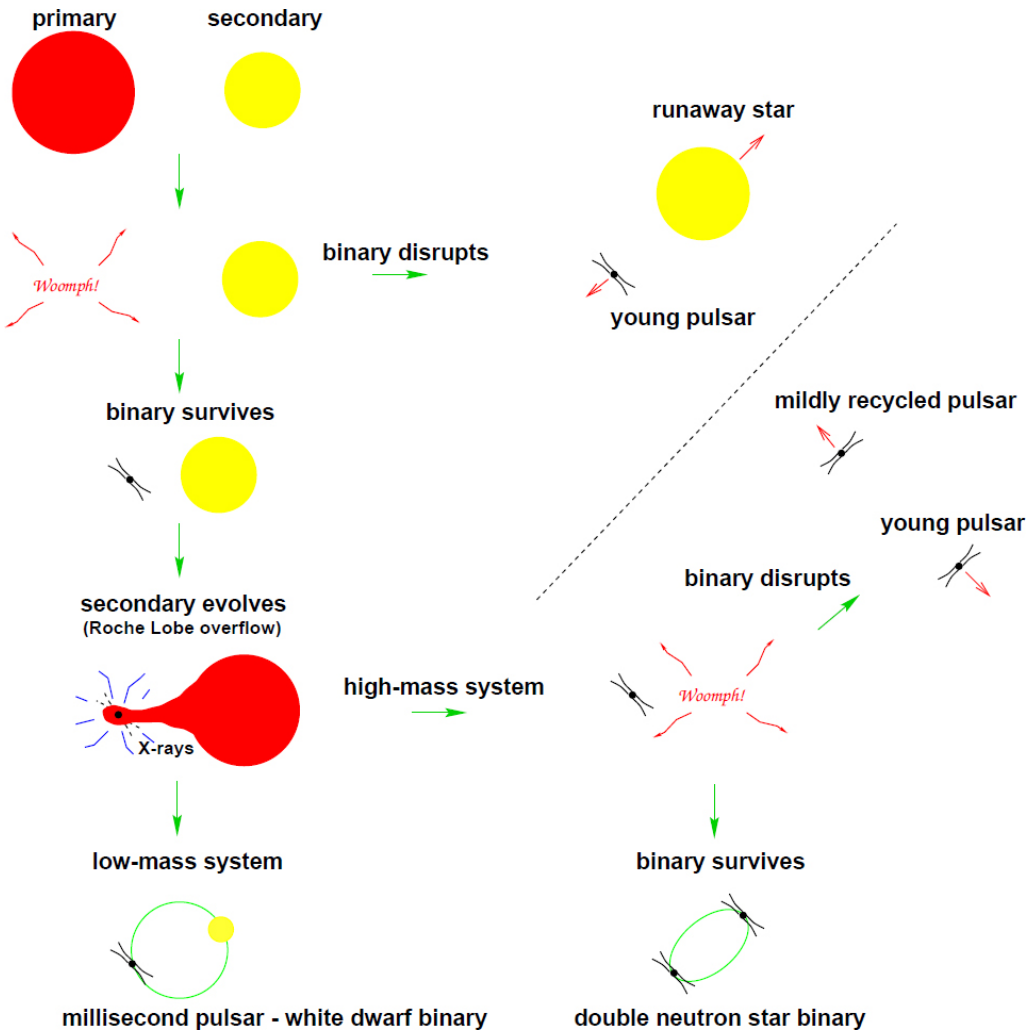

Figure 2.2: Binary neutron star standard formation channel. [8]

a Hubble time. The core of the secondary will eventually undergo a supernova too, either unbinding the system or leaving a tight binary.

2.2.2 Merger dynamics

A BNS merger is characterized by strong gravitational waves (GWs) emission, with a typical form which is illustrated in Figure 2.3. The evolution of the system can be divided into three stages, known as *inspiral*, *merger* and *ringdown*.

Inspiral: in this phase the two objects follow an inspiralling orbit around their centre of mass. The orbit gradually shrinks due to energy loss through GWs emission. The inspiral phase starts when the binary is formed and it takes a long time

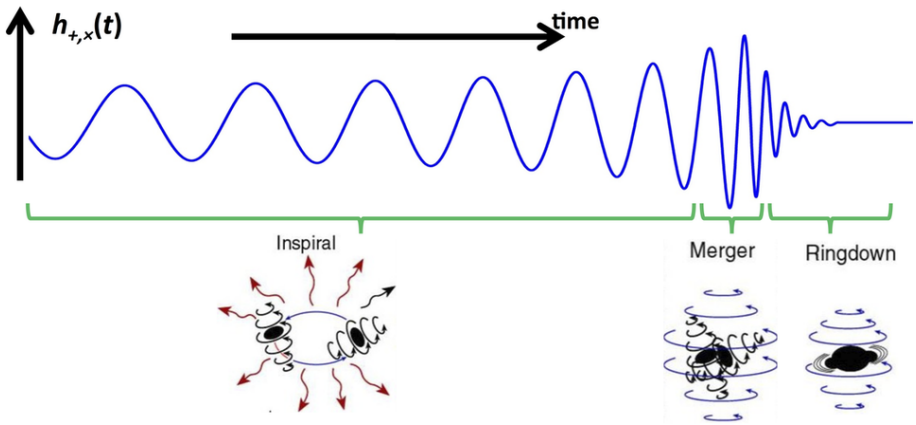

Figure 2.3: Binary merger phases. [9]

(mainly depending on the initial separation) to get to the second stage. This is due to the fact that during this phase the radiation emitted has very low power. The GW signal produced by an inspiralling binary is a sinusoid with amplitude and frequency varying in time while the separation decreases. In this phase we can treat the object as point-masses and we can derive the waveform analytically.

Merger: the merger phase begins shortly before the two objects come into contact. The point-mass approximation is no longer valid here, as the system is governed by strong gravitational field and involves tidal deformation and disruption. To understand the dynamics in this phase we need full general relativistic simulations, which are also predicting the GW emission. The merger of two NSs is not well understood principally due to the uncertainty about the EOS and the effect of the magnetic fields. Gravitational waves produced during this stage carry important information about the structure of the NS and thus about the EOS for supra-nuclear density. This phase takes very short time: from milliseconds to seconds, depending on the masses.

Ringdown: after the merger phase the emitted radiation can be computed by perturbation theory. It consists of a superposition of quasi-normal modes of the remnant, which can give information about the object: in case of a BH remnant, the quasi-normal modes depend on the mass and angular momentum. For a NS remnant instead there is a relation with the EOS. The remaining object will "ring", namely will be oscillating in shape around an equilibrium, emitting GWs due the oscillation asymmetry. The oscillating modes are damped by the GW emission. Signals in this stage are emitted in a very short time, varying from milliseconds to seconds as the previous phase, depending again on the mass of the remnant.

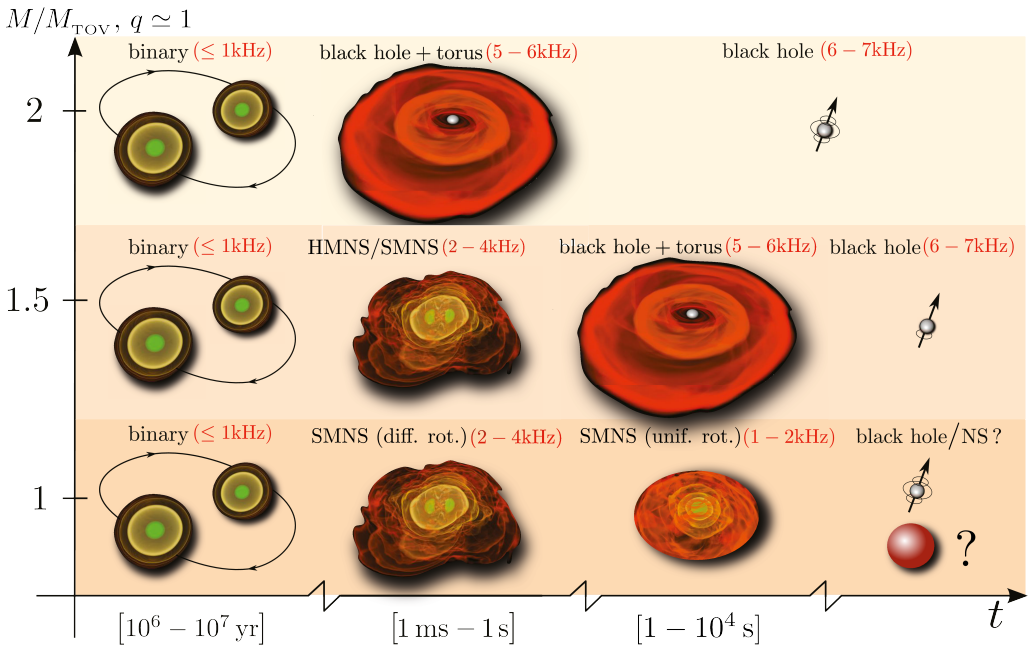

Figure 2.4: Post-merger scenarios for a binary neutron star system. [10]

2.2.3 Post-merger scenarios

While NS-BH mergers will unavoidably end up in a BH, possibly surrounded by a massive accretion disk, after a NS-NS merger there are different possible scenarios (Figure 2.4), depending on the EOS and the rate $M/M_{\rm TOV}$, with M the total mass of the binary. The TOV mass $M_{\rm TOV}$ is the maximum mass allowed for hydrostatic equilibrium of an isolated non-rotating star.

- For $M/M_{\rm TOV} \gtrsim 1.5$ we expect a prompt collapse to a BH surrounded by a torus over a timescale of few ms. The torus will eventually disappear after a few seconds or less after being entirely accreted onto the BH.

- For $1 \lesssim M/M_{\rm TOV} \lesssim 1.5$, the binary NS will merge into a hypermassive NS (HMNS), a NS with mass above the maximum mass allowed for uniformly rotating configurations. Typically, HMNSs will collapse into a BH on a timescale of $10 - 100\,\mathrm{ms}$. HMNSs are believed to be supported by the rapid rotation of the core, and undergo a collapse when enough differential rotation is carried away by gravitational radiation emission or electromagnetic torque.

- For $M/M_{\rm TOV} \lesssim 1$ the binaries will merge into a long-lived NS, which we assume to be either supramassive (SMNS, a NS with mass above the maximum allowed for non rotating configurations) or indefinitely stable. SMNSs can survive for minutes or even longer, against the $10 - 100\,\mathrm{ms}$ of the HMNS. They are

believed to be supported by uniform rotation and to collapse when enough angular momentum is removed via magnetic dipole radiation.

The mechanism leading to the collapse to a BH of HMNSs and SMNSs is still poorly understood, since a growing number of simulations indicate that they both have slowly rotating cores and that collapse is avoided because a significant amount of matter in the outer layers approaches Kepler velocity [11, 12, 13]. Binary NS mergers leading to a NS (hypermassive, supramassive or stable) are characterized by a post-merger phase in which the GWs emission can be significant for several milliseconds and much stronger than those emitted by a BH remnant ringdown signal. The post-merger signal carries information about the remnant structure, thus representing another promising way to constrain the NS EOS.

2.3 Gravitational wave emission

Gravitational waves arise as solutions to the linearized Einstein's field equations. In the weak field limit we can decompose the metric as

$$g_{\mu\nu} = \eta_{\mu\nu} + h_{\mu\nu}, \tag{2.3.1}$$

where $h_{\mu\nu}$ is a small perturbation (i.e. $|h_{\mu\nu}| \ll 1$) over the flat background metric $\eta = diag\,(-1, 1, 1, 1)$. To simplify the expressions we introduce the trace-reversed metric

$$\bar{h}_{\mu\nu} = h_{\mu\nu} - \frac{1}{2}\eta_{\mu\nu}h \tag{2.3.2}$$

and we impose the gauge condition

$$\partial_\nu \bar{h}^{\mu\nu} = 0. \tag{2.3.3}$$

From 2.1.1, at first order in $h_{\mu\nu}$, we find

$$\Box \bar{h}_{\mu\nu} = -16\pi T_{\mu\nu}, \tag{2.3.4}$$

with $\Box = \partial^\mu \partial_\mu$ and $h = \eta^{\mu\nu}h_{\mu\nu}$. Equations 2.3.4 are the linearized field equations. In empty space, where $T_{\mu\nu} = 0$, the solution is a monochromatic plane-wave

$$\bar{h}_{\mu\nu} = C_{\mu\nu} e^{ik_\alpha x^\alpha}, \tag{2.3.5}$$

where $C_{\mu\nu}$ and k_μ satisfy the conditions $k_\mu k^\mu = 0$ and $C_{\mu\nu}k^\nu = 0$.

The solution of equation 2.3.4 is given by [14]

$$\bar{h}^{\mu\nu}\,(t, \mathbf{x}) = \int \frac{4T^{\mu\nu}\,(t - |\mathbf{x} - \mathbf{y}|, \mathbf{y})}{|\mathbf{x} - \mathbf{y}|} d^3y, \tag{2.3.6}$$

and is obtained in analogy with electrodynamics by the convolution of the source term with the Green function

$$G\left(x-y\right)=-\frac{1}{4\pi|\mathbf{x}-\mathbf{y}|}\delta\left(|\mathbf{x}-\mathbf{y}|-x^0-y^0\right).$$

Equation 2.3.6 shows that the metric perturbation at time t depends on the stress-energy tensor evaluated at the retarded time $t_r = t - |\mathbf{x}-\mathbf{y}|$.

For the sake of conciseness, we will state some results without further details, which can be found for example in [14] and [15].

Let's consider our source to be isolated, far away and slowly moving, at distance r from the observer. We define the quadrupole moment tensor of the energy density as

$$I^{ij}=\int y^i y^j T^{00}\left(t,\mathbf{y}\right)d^3y, \tag{2.3.7}$$

and the reduced mass quadrupole as

$$\mathcal{I}_{ij}=I_{ij}-\frac{1}{3}\delta_{ij}I, \tag{2.3.8}$$

with $I = I^k_{\ k}$ the trace of I_{ij}. These quantities allow us to drastically simplify the equations. The metric $\bar{h}_{\mu\nu}$ is related to the quadrupole moment by the relation

$$\bar{h}_{ij}\left(t,\mathbf{x}\right)=\frac{2}{r}\ddot{I}_{ij}\left(t_r\right). \tag{2.3.9}$$

As one can notice, in the previous equations we considered only the spatial components of the tensors involved. This is a consequence of the fact that the constraint $\partial_\mu \bar{h}^{\mu\nu}=0$ implies a relation between the 0ν-components and the $i\nu$-components, such that we can derive the former from the latter.

A useful gauge which is usually imposed when dealing with GWs in empty space (e.g. at the detector, far from the source) is the transverse-traceless gauge (TT-gauge), in which $\bar{h}_{\mu\nu}=h_{\mu\nu}$. In this gauge (for a GW propagating along the z-axis) the metric takes the simple form

$$h_{ij}^{\mathrm{TT}}=\begin{pmatrix}h_+ & h_\times & 0\\ h_\times & -h_+ & 0\\ 0 & 0 & 0\end{pmatrix}_{ij}\cos\left[\omega\left(t-z\right)\right], \tag{2.3.10}$$

where $\omega = k^0$ is the frequency of the wave. The TT-gauge is interesting as it removes all but the physical degrees of freedom, showing that in fact gravity waves have two polarization states. The effect of h_+ and $h_\times$ polarizations on a ring of particle can be seen in Figure 2.5. To extract the transverse-traceless part of a second order tensor we can use the transverse-traceless projector $\mathcal{P}$, defined as

$$\mathcal{P}_{jkmn}\equiv P_{jm}P_{kn}-\frac{1}{2}P_{jk}P_{mn}, \tag{2.3.11}$$

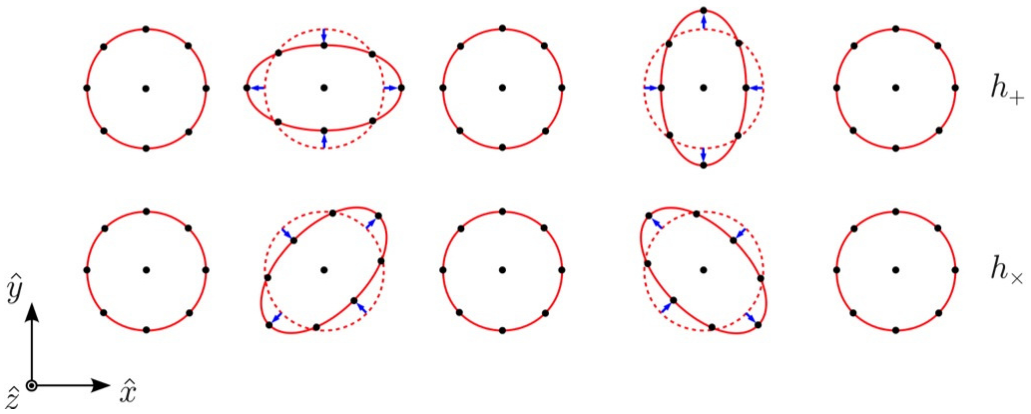

Figure 2.5: Effect of a gravitational wave on a ring of points in the xy-plane. [16]

where $P_{jk} \equiv \delta_{jk} - n_j n_k$ is the operator which projects a vector onto the plane orthogonal to n^μ, which is the propagation direction of the wave (a GW from 2.3.9 is a spherical wave, but locally and far from the source can be seen as a plane-wave propagating along n^μ).

Finally, it is possible to calculate the power emission by GW radiation, which is given by

$$P = \frac{1}{5} \left\langle \dddot{\mathcal{I}}_{ij} \, \dddot{\mathcal{I}}^{ij} \right\rangle , \tag{2.3.12}$$

where $\langle \dots \rangle$ denotes an average over several wavelength; this expression is valid as long as the slowly moving condition is satisfied.

2.3.1 Gravitational waves from inspiralling binaries

As an example we consider a system of two point masses in circular orbit around their common centre of mass. Let m_1 and m_2 be the masses of the two objects, with $M = m_1 + m_2$ the total mass and $\mu = m_1 m_2 / (m_1 + m_2)$ the reduced mass, and $l = r_1 + r_2$ (with reference to Figure 2.6). The orbital frequency is given by $\omega = \sqrt{M/l^3}$. In the reference system depicted in Figure 2.6 the coordinates for m_1 and m_2 are given by

$$x_1 = \frac{m_2}{M} l \cos(\omega t) \qquad x_2 = -\frac{m_1}{M} l \cos(\omega t) \tag{2.3.13}$$

$$y_1 = \frac{m_2}{M} l \sin(\omega t) \qquad y_2 = -\frac{m_1}{M} l \sin(\omega t) \tag{2.3.14}$$

and $z_1 = z_2 = 0$, and the 00-component of stress-energy tensor is

$$T^{00} = \sum_{n=1}^{2} m_n \delta(x - x_n) \, \delta(y - y_n) \, \delta(z) . \tag{2.3.15}$$

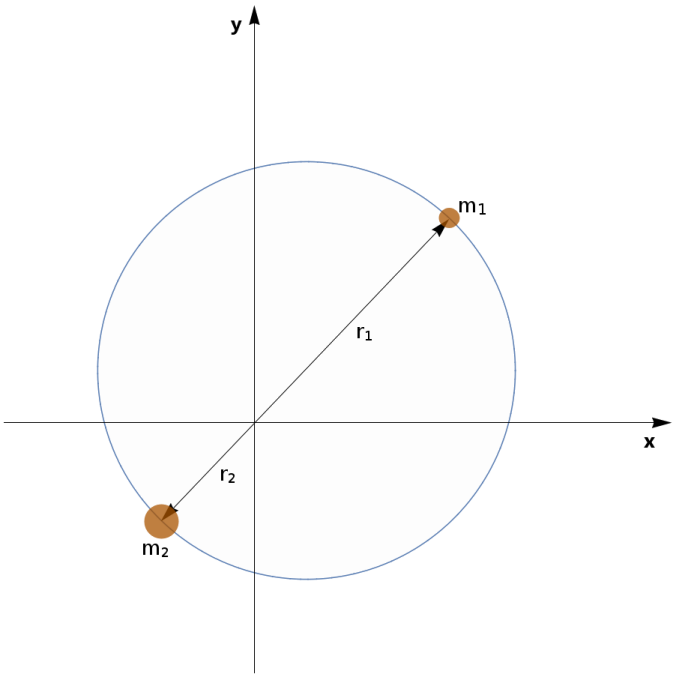

Figure 2.6: Centre of mass frame for binary system. Angular velocity is perpendicular to the xy-plane.

The time-varying part of the reduced quadrupole moment then follows from the definition 2.3.8, and it can be written as

$$\mathcal{I}_{ij} = \frac{\mu}{2} l^2 A_{ij}, \tag{2.3.16}$$

with the matrix $A_{ij}(t)$ given by

$$A_{ij}(t) = \begin{pmatrix} \cos(2\omega t) & \sin(2\omega t) & 0 \\ \sin(2\omega t) & -\cos(2\omega t) & 0 \\ 0 & 0 & 0 \end{pmatrix}_{ij} \tag{2.3.17}$$

In the TT-gauge $\mathcal{I}_{ij}^{\mathrm{TT}} = \mathcal{P}_{ijkl}\mathcal{I}_{kl} = \mathcal{P}_{ijkl} I_{kl}$, so from Equation 2.3.9 we have

$$h_{ij}^{\mathrm{TT}}(t, \mathbf{x}) = \frac{2}{r} \ddot{\mathcal{I}}_{ij}^{\mathrm{TT}}(t - r) = h_0 A_{ij}^{\mathrm{TT}}(t - r), \tag{2.3.18}$$

where $A_{ij}^{\mathrm{TT}} = A_{ij}$ if the line of sight coincide with the z-axis, and $h_0 = \frac{4\mu M}{rl}$ is the wave amplitude. From Equation 2.3.18 we see that the radiation is emitted at twice the orbital frequency.

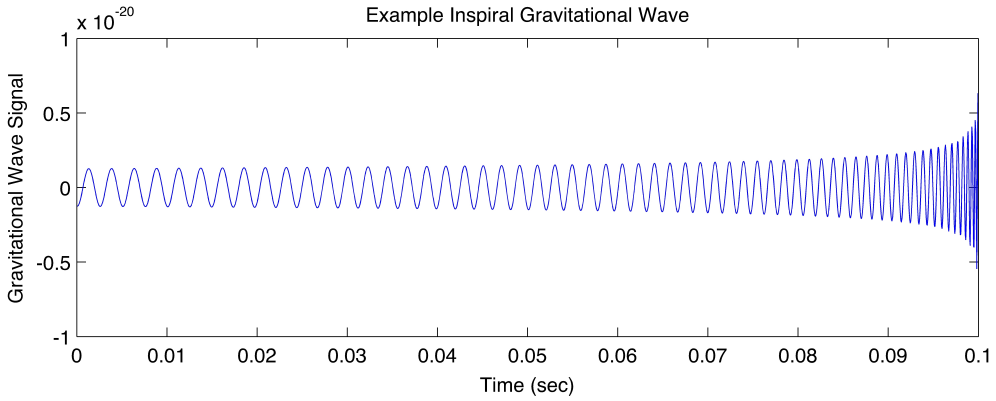

Figure 2.7: Example of an inspiral waveform.[17]

Consider now the time-evolution of the system. The power emitted is given by Equation 2.3.12

$$W_{\mathrm{GW}} = \frac{32}{5}\frac{\mu^2 M^3}{l^5}. \tag{2.3.19}$$

Supposing that the system has the time to adjust the orbit to compensate the energy loss by gravitational radiation, i.e. $\dot{E}_{\mathrm{orbital}} + W_{\mathrm{GW}} = 0$, where E_{orbital} is the sum of kinetic and potential energy, one can derive how the orbital separation l changes with time due to the emission of GWs:

$$l\left(t\right) = l_0\left(1 - \frac{t}{t_{\mathrm{coal}}}\right)^{\frac{1}{4}}, \tag{2.3.20}$$

where $l_0 = l\left(t=0\right)$ and $t_{\mathrm{coal}} = \frac{5}{256}\frac{l_0^4}{\mu M^2}$ is the time at which the separation becomes null. Since in a realistic case the two masses are not point-like, the merger starts before t_{coal}. Furthermore, when the two objects are close enough, the weak field approximation and the slow motion assumption are not satisfied, making the quadrupole formalism failing. However, t_{coal} gives an indication of the time that the system needs to merge starting from an orbital distance l_0.

From the definition of the orbital frequency we can compute how it changes in time:

$$\omega = \sqrt{M/l\left(t\right)^3} = \omega_0\left(1 - \frac{t}{t_{\mathrm{coal}}}\right)^{-\frac{3}{8}}, \tag{2.3.21}$$

where $\omega_0 = \sqrt{M/l_0^3}$. The GW frequency $\nu_{\mathrm{GW}} = \omega/\pi$ is twice the orbital frequency. The amplitude can be written as

$$h_0\left(t\right) = \frac{4\pi^{\frac{2}{3}}\mathcal{M}^{\frac{5}{3}}}{r}\nu_{\mathrm{GW}}^{\frac{2}{3}}\left(t\right), \tag{2.3.22}$$

where $\mathcal{M} = \mu^{3/5} M^{2/5}$ is the so-called "chirp mass". We then see that the amplitude and frequency emitted by a coalescing binary system increase with time, with a characteristic signal similar to the chirping of bird. An example of such signal is depicted in Figure 2.7.

2.4 Short gamma-ray bursts

Gamma-ray bursts (GRBs) are among the brightest events known in the Universe. They consist of highly energetic photon beams (observable in the gamma-ray band) that light up a tiny region in the sky, with a duration from a fraction of second up to hundreds or even thousands of seconds. They are characterized by a random distribution, and a current rate of the order of few hundreds per year.

Two classes of GRBs have been identified based on duration and spectral hardness. We refer to the long-soft bursts as long GRBs, while the short-hard bursts are known as short GRBs (SGRBs). The distinction from long to short is given by $T_{90} \gtrless 2\,\mathrm{s}$, where T_{90} is the time window containing the 90% of the energy released. This distinction is indicative of two types of GRBs, associated with different progenitor systems. Observational results allowed to link long GRBs with the death of massive stars [18]. In particular, these events have only been observed in star-forming galaxies and often found in the brightest star-forming regions of the host galaxy [19, 20]. Moreover, starting with the supernova 1998bw [21], there are a number of direct associations of long GRBs with type Ic core-collapse supernovae that have been collected over the last 20 years, confirming the connection between the two phenomena.

On the other side, SGRBs' progenitor has not been confidently identified until 2017 (see Section 2.6). While the association with supernovae seemed to be excluded by the observations, the leading candidates as a source of SGRBs were in fact compact binary systems composed of two NSs or a NS and a BH. This idea was supported by a broadly consistent event rates and the fact that these systems are compatible with short-duration and powerful central engine, having dynamical timescales of milliseconds, and baryon-poor environments [22]. In addition, the lack of supernova associations, the observation in all type of host galaxies, and the larger offset from the centre of the host galaxies, which suggests a progenitor system with large natal kick and significant time delay between its formation and the SGRB, strengthened the hypothesis of a binary merger as a central engine while on the other side disfavoured the connection with core-collapse supernovae [23].

Another fact supporting the binary merger scenario was provided by the observation of an optical/infrared afterglow emission in the GRB event 130603B, which was interpreted as a signature of a binary merger [24, 25]. BNS and NS-BH systems eject a significant amount of matter in the surroundings, in particular neutron-rich

nuclei. In this environments r-process nucleosynthesis is expected to take place [26, 27, 28], and the radioactive decay of the produced elements could lead to a potentially observable thermal emission [29]. The resulting signal is known as "kilonova" or "macronova" (which will be discussed in Section 2.5), and is a possible EM counterpart to the GW signal expected from a compact binary merger. The GRB 130603B was compatible with a kilonova, suggesting a merger event as a progenitor system for the burst.

The August 17th 2017 event (see Section 2.6) proved the binary merger hypothesis on SGRB progenitors. The long-awaited smoking gun evidence was a SGRB detection in coincidence with a GW signal from the merger. While this discovery represents a great breakthrough, the mechanism by which a binary merger can power a SGRB is still unclear. In the following, we will focus on three main scenarios leading to the formation of a relativistic jet.

2.4.1 Central engine scenarios

While numerous GRB observations provided information on the jet structure and evolution, as well as constraints on the mechanisms responsible for the gamma-ray emission and the multi-wavelength afterglows, much less observational constraints exist on the nature of the central engine, on the launching mechanism and on the initial properties of the incipient jet. This lack of information, together with the very rich but yet partially unknown physics, makes this investigation extremely challenging.

In the most prominent scenario the role of central engine is played by a BH surrounded by a massive accretion disk (BH-disk). This is a very natural outcome of a BNS merger, and can also be the outcome a NS-BH merger under certain (realistic) conditions. These systems offer an almost baryon-free environment along the BH spin axis, which allows the launch of a relativistic outflow; moreover, the merger dynamical timescales are consistent with the requested duration of the SGRB central engine. The prompt SGRB emission, assuming an opening angle of $\theta_{\rm jet} \sim 10^\circ$, results in luminosities of the order of $L \sim 10^{49} - 10^{50}\,{\rm erg/s}$. We then need a mechanism which can produce such energies. There are two leading mechanisms that have been proposed: the $\nu\bar{\nu}$ annihilation along the BH spin axis [26] and magnetohydrodynamics effects possibly including the Blandford-Znajek mechanism [30].

Massive disks around hyperaccreting stellar-mass BHs are expected to emit a large number of neutrinos and antineutrinos. The cumulative energy deposition at the poles of the BH via $\nu\bar{\nu}$ annihilation is of the order of $\sim 10^{49}\,{\rm erg}$, as found by recent simulations [31, 32], thus being at the lower bound of the energy budget. An additional problem may be the baryon pollution along the spin axis of the BH. For a BNS the surroundings of the merger site can be polluted by dynamical ejecta, post-

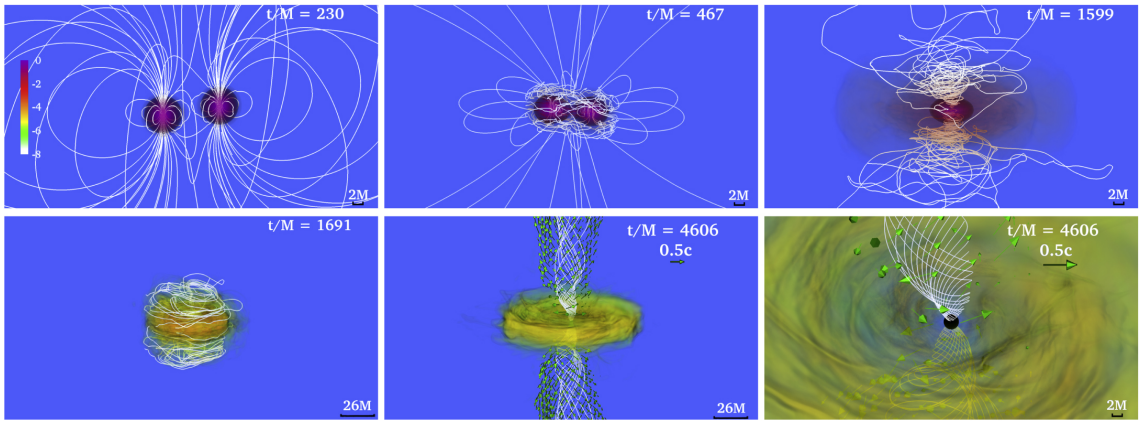

Figure 2.8: Simulation of a BNS merger showing the formation of a jet-like structure in the magnetic field lines. [34]

merger baryon winds and possibly metastable NS remnant. Simulations studying the jet-ejecta interaction seem to agree that a neutrino-powered jet would not have enough energy to successfully emerge from the environment, nor to explain a typical SGRB. For a NS-BH merger (where there is less pollution) the neutrino-powered jet energy would only be sufficient to explain SGRBs of relatively low luminosity. Due to above difficulties this mechanism is not the most promising one.

Although there are different magnetohydrodynamics mechanisms, the most discussed is the Blandford-Znajek mechanism. The energy to launch a jet comes from a Kerr BH threaded by a strong magnetic field connected to an external load of material (e.g. a magnetized accretion disk). This combination can power a Poynting flux dominated outflow, at the expense of the BH rotational energy, which is extracted via magnetic torque. The resulting luminosity is approximately given by [33]

$$L_{\rm BZ} \sim 10^{51}\,(\chi/0.8)^2\,(M_{\rm BH}/6\,M_\odot)^2\left(B_{\rm BH}/10^{15}\,{\rm G}\right)^2\ {\rm erg/s}, \tag{2.4.1}$$

where χ and $M_{\rm BH}$ are the dimensionless spin and mass of the BH and $B_{\rm BH}$ is the characteristic magnetic field strength close to the BH. As we can see strong magnetic fields are necessary. This mechanism has been already seen at work in numerical simulations; in Figure 2.8 we see the magnetic field lines forming a jet structure along the spin axis of the BH.

As we already pointed out, a BNS can merge into a metastable or even stable NS. A HMNS will collapse into a BH within few to about 100 milliseconds, falling in the BH-disk scenario already described. A long-lived NS instead is the central engine of the so-called magnetar scenario. A suggestion that a fraction of SGRBs might be produced by a NS remnant comes from specific features in the soft X-ray emission detected from the Swift satellite [35]. These features possibly indicate an

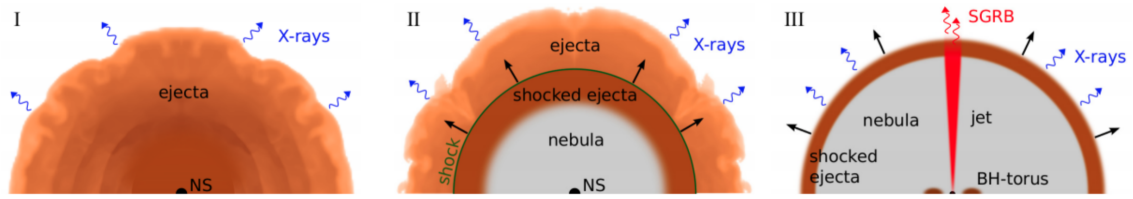

Figure 2.9: Evolution of a BNS merger in the time-reversal scenario. **Phase I**: A BNS merger forms a differentially rotating NS that emits a baryon-loaded wind. **Phase II**: the NS eventually settles down to uniform rotation and inflates a pulsar wind nebula that sweeps up all the ejecta material into a thin shell. **Phase III**: the NS collapses into a BH, and a jet is launched. [36]

ongoing activity on timescales greater that the typical accretion timescale of a disk onto a BH.

In the magnetar scenario the jet is expected to be launched by a strongly magnetized NS. In particular, the mechanism by which the jet is produced is still unclear, but the large rotational energy of the magnetar, if efficiently channelled via its strong magnetic field, would in principle be sufficient to power a SGRB. This model is interesting as it can explain the X-ray plateaus in the afterglow that accompanied a significant fraction of the observed SGRBs. In fact, these X-ray transients can be produced by the EM spin-down radiation of the magnetar, as after launching the jet there is still a very large energy reservoir given by the NS rotational energy that can be extracted via the magnetic field.

A major issue with this scenario is the presence of a baryon polluted environment, which is expected to be of higher density as compared to the BH-disk, and can thus prevent the jet from escaping. A recently proposed scenario which can overcome the difficulties of the magnetar model and at the same time can explain the X-ray afterglows is the time-reversal scenario [36]. In this scenario the BNS merge into a long-lived but metastable NS (i.e. a SMNS). At some point the centrifugal support will become insufficient to prevent the collapse into a BH. The time-reversal assumes that after the collapse we have a BH surrounded by an accretion disk, which can launch a jet as described in the BH-disk scenario. Conversely to the magnetar, the jet here is launched after the spin-down radiation has been emitted. At this time, the surroundings is no longer heavily baryon polluted, and therefore the jet finds no obstacles to its propagation. Because of the high optical depth of both the nebula and the ejecta, the spin-down energy remains trapped for a long time before emerging and producing the X-ray plateau. This means that the SGRB and the X-ray transient are observed in a reverse order with respect to their respective energy emission from the central object. In Figure 2.9 we see the evolution of the system in the time-reversal scenario.

2.5 Kilonovae

Kilonovae are isotropic thermal transients at optical/infrared wavelengths lasting days to weeks, providing a robust EM counterpart to the GW signal. They are expected to accompany essentially all BNS mergers and a fraction of BH-NS mergers. To understand the physics of kilonovae we start considering the merger ejecta of total mass M, expanding at a constant mean velocity v, with mean radius $R \approx vt$ at time t after the merger. The ejecta is extremely hot immediately after being ejected, however this thermal energy cannot escape as radiation because of the high optical depth at early times, and correspondingly long photon diffusion timescales. As the ejecta expands, the diffusion time decreases, until radiation can escape, determining the characteristic timescale at which the light curve peaks. This timescale can be written as [37]

$$t_{\rm peak} \equiv \left(\frac{3M\kappa}{4\pi\beta v}\right)^{\frac{1}{2}} \approx 1.6\,{\rm d}\left(\frac{M}{10^{-2}\,M_\odot}\right)^{\frac{1}{2}}\left(\frac{v}{0.1\,c}\right)^{-\frac{1}{2}}\left(\frac{\kappa}{1\,{\rm cm^2 g^{-1}}}\right)^{\frac{1}{2}}, \qquad (2.5.1)$$

where $\beta \approx 3$ is a constant and depends on the precise density profile of the ejecta and κ is the opacity (cross section per unit mass). For values of $\kappa \sim 0.3 - 30\,{\rm cm^2 g^{-1}}$, which characterize the range from lanthanide-free to lanthanide-rich matter (the reason to do this distinction will be clear later), Equation 2.5.1 predicts timescales from 1 day to 1 week. The freshly ejected matter has temperatures which in general exceed $10^9 - 10^{10}\,{\rm K}$, but without a source of heating, this matter will cool through adiabatic expansion, loosing almost all of its initial thermal energy before reaching the radius at which the ejecta becomes transparent. These losses would leave the ejecta too cold to be visible at large distances. In a realistic situation the ejecta will be heated by the radioactivity of newly synthesized heavy elements, with the peak luminosity of the observed emission depending on the heating rate. At this point it is clear that we need to know three main ingredients: the mass and velocity of the ejecta, its opacity, and the heating source.

In BNS (and BH-NS) mergers there are mainly three important sources of ejecta. First, the matter is ejected on dynamical timescales of milliseconds either by tidal forces or due to compression-induced heating at the interface between merging bodies. Secondly, if there is a massive NS remnant phase (only for BNS), neutrino or magnetically induced baryon winds can be launched. Finally, further mass ejection is expected from the accretion disk surrounding the final BH. The properties of these different types of ejecta are well described in literature (see [37] and references therein). Typical values of mass and velocity for BNS merger ejecta are $M \sim 10^{-3} - 10^{-2}\,M_\odot$ and $v \sim 0.1 - 0.3\,c$, thus the parametrization in 2.5.1.

The opacity of the ejecta will depend on its conditions after the merger. In Figure 2.10 we can see a schematic illustration of the opacity of the ejecta as function of the

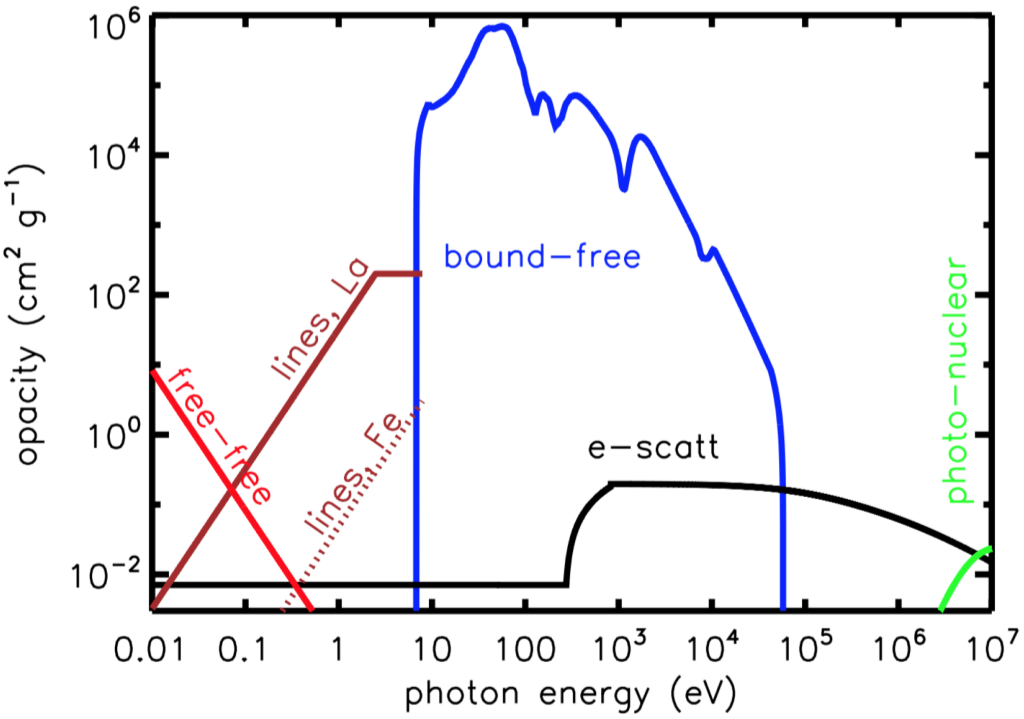

Figure 2.10: Schematic and approximate illustration of the opacity of a BNS merger ejecta as function of photons energy. See the text for a more detailed description. [37]

photon energy at a fixed epoch near the peak light. At the lowest frequencies the free-free absorption dominates. After the ejecta has expanded, the decreasing density and the fewer number of free electrons (as the ejecta cools down and recombination takes place) make the free-free opacity decrease rapidly, leaving the IR band transparent. At optical wavelength the opacity depends sensitively on the ejecta composition, i.e. on the outcome of the heavy element nucleosynthesis (more details below). To simplify, we can distinguish between lanthanide-free and lanthanide-rich. For lanthanide-free ejecta the opacity follows the dashed line of Fe. A lanthanide-rich ejecta follows the solid line La, and the opacity can be orders of magnitude higher. Throughout the far UV and X-ray bands the bound-free transitions of the partially neutral ejecta dominates the opacity. This prevents radiation from escaping at these frequencies. At hard X-rays and gamma-ray energies the electron scattering provides an important opacity, while for gamma-ray energies greater than 10^6 GeV the opacity is due to electron/positron pair production on nuclei. The low opacity in the $\approx$ MeV energy range implies that gamma-rays largely escape before the optical/NIR peak. Gamma-rays with energies up to $\approx$ TeV (not shown in figure) can also undergo pair production by interacting with lower energy optical or X-ray photons. The optical

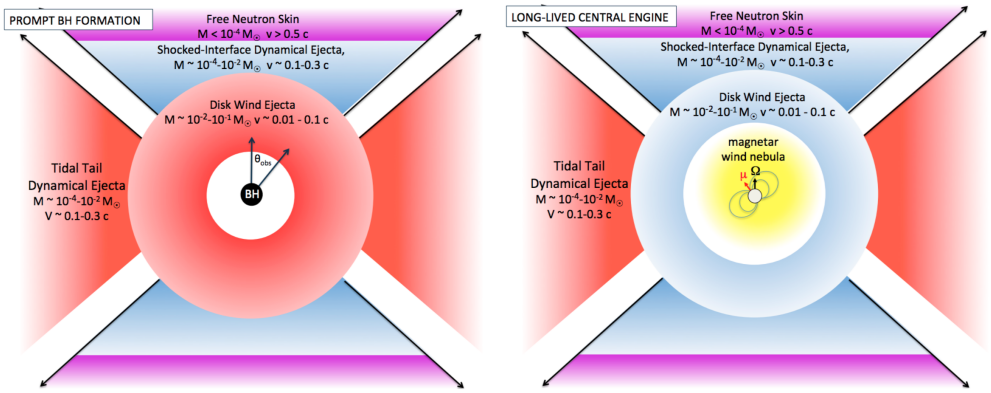

Figure 2.11: Schematic representation of the different components of the ejecta leading to either a red or a blue kilonova. [37]

depth for these energies shows ([37]) that $\sim$ GeV $-$ TeV photons will be trapped for days to weeks after the merger. We can then conclude that a prompt gamma-ray emission (e.g. GRBs) is unlikely to come from the merger ejecta.

The ejecta material is very hot and highly neutron rich ($Y_e \equiv n_p/\left(n_n + n_p\right) \lesssim 0.25$). This creates the ideal conditions for r-process nucleosynthesis, with the formation of heavy unstable isotopes. The radioactive decay of these nuclei can act as a dominant heating source for the ejecta [37]. The luminosity and color evolution of kilonovae encode information on the quantity of r-process ejecta and, in principle, the abundance of lanthanide/actinide elements. The ejected matter with $Y_e \lesssim 0.25$, capable of forming heavy r-process nuclei, will produce a high-opacity lanthanide-rich layer within the equatorially focused tidal tail, or in more spherical outflows from the accretion disk. The emission will peak at NIR wavelength on timescale of several days, while the UV/optical wavebands are suppressed due to the high lanthanide opacity (see Figure 2.10). This results in a "red" kilonova. Some ejected matter may also contain a lower neutron abundance (i.e. $Y_e \gtrsim 0.30$), being then low-opacity and lanthanide-free, as the r-process nucleosynthesis is not efficient as in the first case. This matter can reside in the polar regions, due to dynamical ejection, or in more isotropic outflows from the massive NS remnant or the accretion disk. As shown in Figure 2.10, this condition leaves the optical (up to UV) band transparent, which is where the emission now peaks. The timescale of this "blue" kilonova is about 1 day, and can be $2-3$ magnitudes brighter than the red one. Figure 2.11 shows the different components of the ejecta and their kilonova emission. In general both the blue and red components can be present at the same time, so the total kilonova can be though as a combination of the two.

2.6 The first multi-messenger observation of a binary neutron star merger

On August 17, 2017, the LIGO-Virgo detector network observed a gravitational wave signal from the inspiral of two objects consistent with a BNS. This event was also accompanied by a multi-wavelength emission of photons across the whole EM spectrum. Being the first observation combining GW and EM signals, this breakthrough event marked the beginning of multi-messenger astrophysics with GW sources. In the following we discuss the most important signals associated with this merger: GW signal, SGRB, and kilonova.

2.6.1 The gravitational wave signal GW170817

The gravitational wave signal [38] had a duration of about 100 s (calculated starting from 24 Hz, when it emerged from the instrumental noise), and it was identified as a BNS merger inspiral by matched filtering the data against post-Newtonian waveform models. With a combined signal-to-noise ration of 32.4, it is the loudest yet observed. Thanks to the combination of the data from LIGO and Virgo detectors, the event was localized with relatively high precision. The first localization enabled an EM follow-up campaign that ultimately identified a counterpart near the galaxy NGC 4993, consistent with the localization and distance inferred from the GW signal. In Figure 2.12 we see the time-frequency representation of GW170817. The signal is clearly visible in the LIGO data, while it does not appear in the Virgo panel due to the disfavourable direction of the source with respect to the detector's antenna pattern. The Virgo data however contributed to the sky localization of the source in a sky area of about $28\,\mathrm{deg}^2$ at a luminosity distance of $\sim 40\,\mathrm{Mpc}$. The chirp mass is well constrained from the data, while the masses of the two object are affected by the degeneracy between the mass ratio and the aligned spin components. For high-spin assumption the mass ration q can be restricted to $q \in (0.53 - 1.0)$, while for the low-spin case $q \in (0.73 - 1.0)$, while the chirp mass is $\mathcal{M} = 1.186^{+0.001}_{-0.001}\,M_\odot$ [39]. The GW signal carries information about the internal structure (i.e. on the EOS). In particular, the tidal deformability $\Lambda = 2/3\,k_2\,(R/m)^5$, where k_2 is the second Love number, which is an EOS-sensitive quantity, affects the waveform inducing a mass-quadrupole moment and accelerating the coalescence. The tidal deformability parameters inferred from the data of GW170817 allowed to rule out some stiff EOS [40], deeming soft EOS as the APR4 used in our simulations more favourable (motivating our choice).

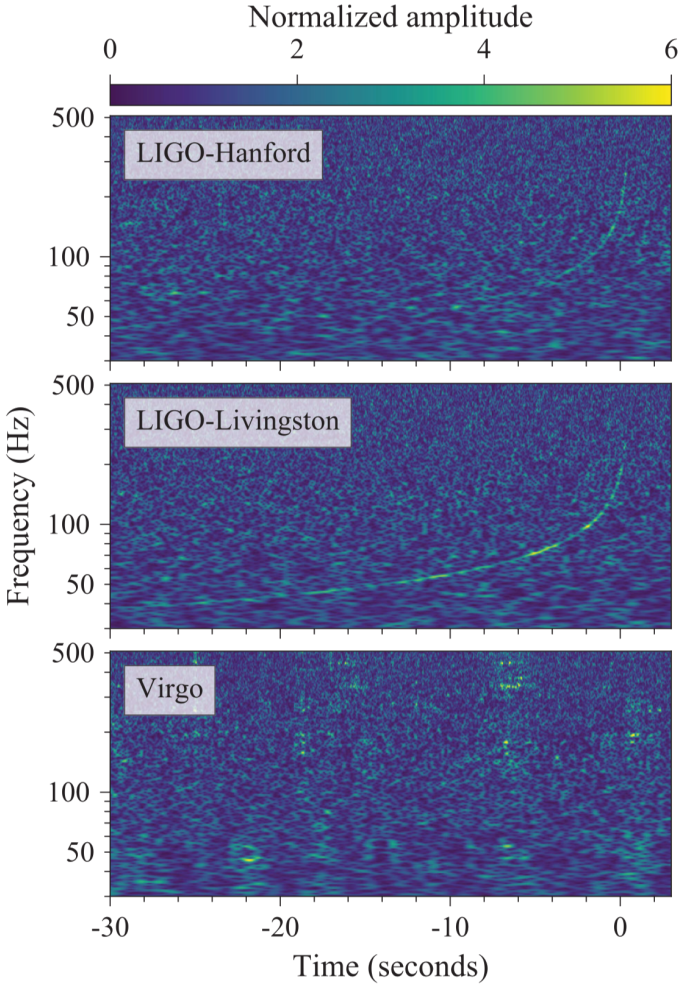

Figure 2.12: Time-frequency representation of GW170817. [38]

2.6.2 The gamma-ray burst GRB 170817A

After about 1.7 s after the BNS merger a signal in the gamma-ray band was detected [41]. The combined constraints on the sky position of the event from GW and gamma-ray signals was fundamental for the optical follow-up search that eventually identified the host galaxy, NGC 4993, at a distance consistent with the GW estimate. The duration ($T_{90} = 2.0 \pm 0.5$ s) and the spectrum of GRB 170817A are compatible with a SGRB event, enforcing the idea of BNS mergers as central engine for SGRBs. At the beginning, however, it was not possible to firmly establish the nature of GRB 170817A for several reasons. Considering the distance of the event, the observed burst resulted in a much less energetic ($\sim 10^{46}$ erg) and luminous ($\sim 10^{47}$ erg/s) than expected in a canonical SGRB. Moreover, X-ray and radio

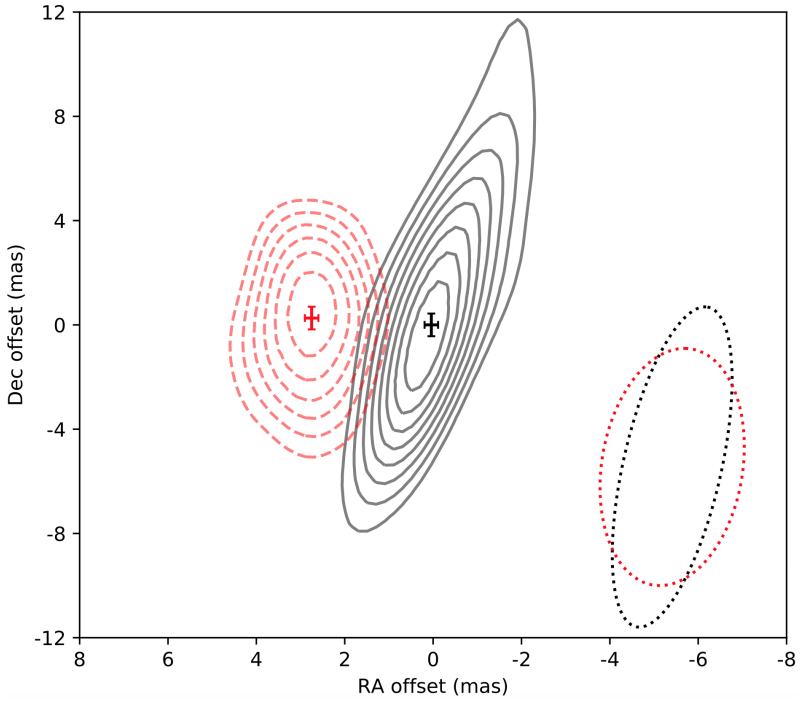

Figure 2.13: Proper motion of the radio counterpart of GW170817. [43]

afterglows emerging 9 and 16 days after the merger were inconsistent with an ultra-relativistic jet pointing towards us. Further modelling of the prompt and afterglow emission suggested that the observed event was produced by a mildly relativistic outflow along the line of sight, allowing for different interpretations.

Two main ideas were proposed [42]. One possibility is that the event produced a canonical SGRB jet pointing away from us. The jet core has not been observed, while we detected a sub-energetic prompt gamma-ray emission produced by the mildly relativistic and wide angle cocoon formed around the jet by the interaction of the latter with the baryon polluted environment. This hypothesis is broadly compatible with the BH-disk scenario, while the magnetar scenario is disfavoured, but it cannot be completely excluded.

Another possible interpretation is that the incipient jet launched by the merger was not powerful enough to escape the baryon-polluted surroundings, forming a choked jet. This resulted into a jet-less, wide angle and mildly relativistic outflow. The main difference with the canonical SGRB is that the choked jet is more favourable for the magnetar scenario, as the difficulty in the production of a successful jet would be in agreement with the observations.

Further investigations [43, 44] allowed to solve the puzzle. In Figure 2.13 we see that the position of the radio source associated with GW170817 changed in time.

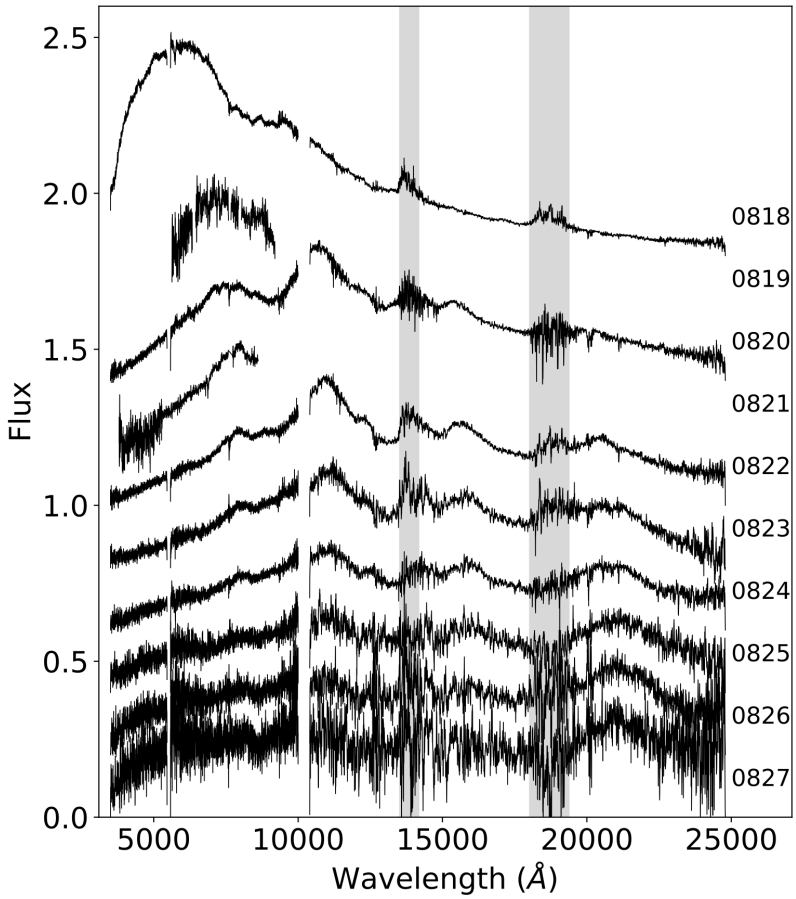

Figure 2.14: Time evolution of the AT2017gfo spectrum. [45]

This is not compatible with an isotropic emission, as we would expect an expanding but fixed source, implying that the choked jet scenario is unlikely. Moreover Ghirlanda et al. [44] found that the radio source remained rather compact over time, also disfavouring a choked jet scenario. In conclusion, GRB 170817 is most likely a canonical GRB observed off-axis by about $15 - 30$ degrees.

2.6.3 The kilonova AT2017gfo

After 11 hours from the merger a UV-optical-NIR transient (named AT2017gfo) was detected in association with GW170817. The signal rapidly evolved from blue colours peaked at UV wavelength on a timescale of a day to red colours peaked around $1.5\,\mu$m on a timescale of several days. This transient is consistent with current models for thermal emission from kilonovae, with the peaks timescale matching the expected ones given by Equation 2.5.1. The time evolution of the AT2017gfo

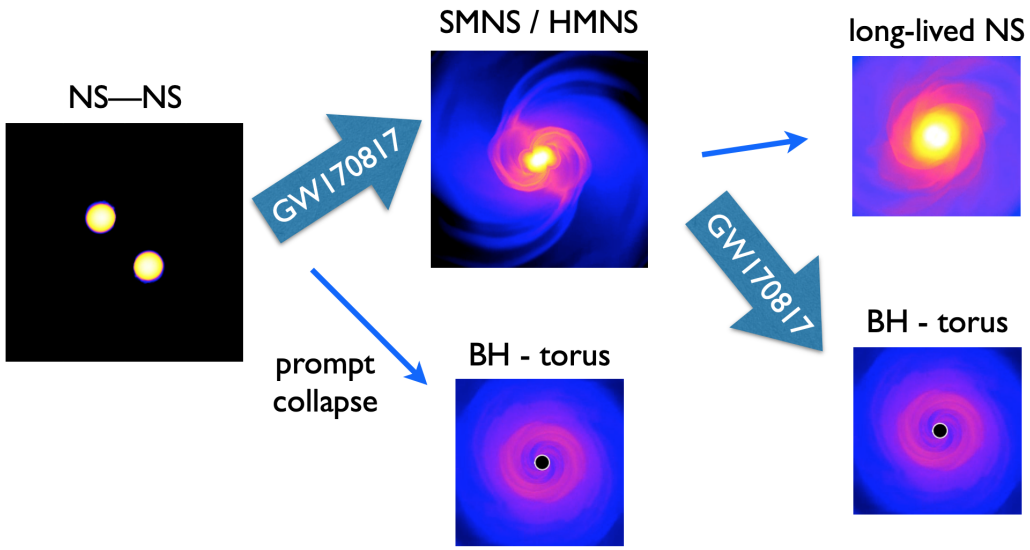

Figure 2.15: Overview of the phenomenology of a BNS merger, highlighting the most likely path for GW170817. [47]

spectrum is shown in Figure 2.14.

At the beginning the spectrum is peaked at blue wavelength. The blue component is characterized by a total luminosity of 3.2×10^{41} erg/s [45], ejecta mass of $\sim 10^{-2}\, M_{\odot}$, velocity $\sim 0.2\, c$ and opacity $\sim 0.5\, \mathrm{cm}^2/\mathrm{g}$. Such values are indicative of a lanthanide-poor ejecta. Further modelling of the event showed that the blue emission of AT2017gfo is compatible with magnetically driven winds ejecta in the early post merger phase (e.g. [46]).

The red component emerged after few days, with mass of $\sim 10^{-2}$ and velocity of $0.1\, c$ and showed an opacity increasing with time up to $10\, \mathrm{cm}^2/\mathrm{g}$, indicating a lanthanide-rich ejecta originating from disk outflows [47].

The most likely evolution path of GW170817 is depicted in Figure 2.15. To produce magnetically driven winds the BNS should have merged into a meta-stable NS, but the lifetime of this remnant should not be too long. In fact, if the remnant NS survives too much (more than a few hundred ms), strong neutrino emission would raise the electron fraction of the disk outflows, turning their kilonova blue. In conclusion, while the GW data alone cannot exclude a prompt collapse to a BH nor a very long-lived NS remnant, the properties of the kilonova AT2017gfo strongly favour a short-lived massive remnant NS collapsing to a BH within a few hundreds of ms.

3 Numerical approach to General Relativity

General Relativity is a very challenging framework to work within. In fact, very few analytical solutions to Einstein's equations (EE) are known, and they can be found only in ideal cases (e.g. the Schwarzschild solution for a non-rotating black hole). Since we want to explore the extreme physics of a BNS merger, we should be able to write down the initial conditions of the system and evolve it through EE. While we will focus on the initial conditions in Chapter 4, here we want to understand how to perform the evolution of a system in General Relativity without knowing the explicit solutions of EE. Thanks to modern supercomputers we are able to numerically solve EE, but first we need to write them in a suitable way for numerical integration.

In the following we will derive the fundamental equations governing the evolution of spacetime in the 3+1 formalism. We will find a different but equivalent form for EE, which is more suitable for integration. In particular we will present the BSSNOK formalism, which is the one implemented in the code we use. After that we will introduce the fundamental equations of magnetohydrodynamics and the Valencia formulation. In the last section we will review some numerical methods of our interest.

3.1 The 3+1 decomposition of Einstein's Equations

The problem we are facing can be posed in terms of a traditional Cauchy problem. The evolution of a general relativistic gravitational field is determined by the metric quantities $g_{\mu\nu}$ and their time derivative $\partial_t g_{\mu\nu}$, as in classical dynamics for a given system it is determined by the initial positions and velocities of its constituents. We have then to specify those metric quantities on every point in space at a given initial time. Then, provided we can obtain from EE expressions for $\partial_t^2 g_{\mu\nu}$, we can compute $g_{\mu\nu}$ and $\partial_t g_{\mu\nu}$ on a new spacelike hypersurface at some time $t + \delta t$ integrating them. To obtain such expressions for $\partial_t^2 g_{\mu\nu}$ is not so trivial. We need 10 second derivatives, and it seems we have 10 field equations, but recalling the Bianchi identity for which $D_\nu G^{\mu\nu} = 0$, we see that

$$\partial_t G^{\mu 0} = -\partial_i G^{\mu i} - G^{\nu\rho}\Gamma^{\mu}_{\nu\rho} - G^{\mu\nu}\Gamma^{\rho}_{\nu\rho}.$$

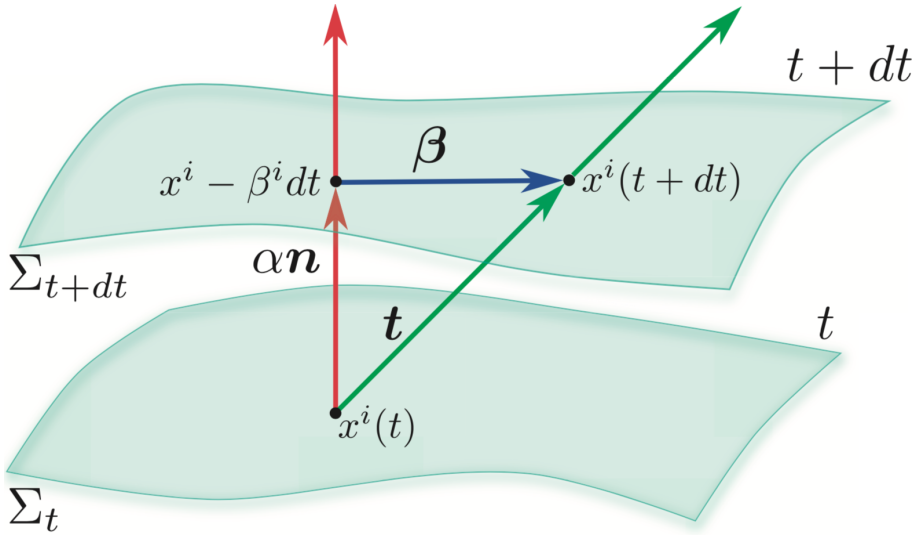

Figure 3.1: A foliation of the spacetime M [48].

Since on the right hand side there are not third time derivatives nor higher, $G^{\mu 0}$ cannot contain second time derivatives, so the 4 equations $G^{\mu 0} = 8\pi T^{\mu 0}$ will not furnish any information required for the dynamical evolution. They will rather supply constraints for the initial data, giving four relations between $g_{\mu\nu}$ and their time derivatives which have to be fulfilled on the initial hypersurface. The information we need are then to be extracted from the six $G^{ij} = 8\pi T^{ij}$ equations. Apparently there is a mismatch between the number of required quantities (10), and the number of dynamical field equations (6), but since we are free to choose four different coordinates to label the points in our spacetime we can adopt, for example, Gaussian normal coordinates, and set $g_{00} = -1$ and $g_{0i} = 0$, reducing to six metric variables g_{ij} to evolve.

At this point we see that formulating the Cauchy problem in General Relativity logically involves the decomposition of spacetime into a three-dimensional space plus a one-dimensional time.

3.1.1 Foliations of spacetime

Let us consider a four-dimensional manifold M with metric $g_{\mu\nu}$. We assume that the spacetime $(M,\ g_{\mu\nu})$ can be foliated into a family of non-intersecting spacelike three-surfaces Σ, which arise, at least locally, as the level surfaces of a scalar function t that can be interpreted as a global time function (Figure 3.1). From the function t we can define the 1-form

$$\Omega_\mu = \nabla_\mu t, \tag{3.1.1}$$

which is closed by construction ($\nabla_{[\mu}\Omega_{\nu]} = 0$). We can compute the norm of Ω as

$$||\Omega||^2 = g^{\mu\nu}\nabla_\mu t \nabla_\nu t \equiv -\frac{1}{\alpha^2}. \tag{3.1.2}$$

We will see that α measures how much proper time elapses between neighboring slices along the normal vector Ω^μ to the slice, and is therefore called lapse function. We assume α to be positive such that Ω^μ is timelike and Σ is spacelike everywhere. We then define the unit normal vector to the slices as

$$n^\mu \equiv -g^{\mu\nu}\omega_\nu, \tag{3.1.3}$$

where $\omega_\mu \equiv \alpha\Omega_\mu$. The negative sign has been chosen so that n^μ points in the direction of increasing t. By construction n^μ is normalized and timelike, and thus can be thought as the four-velocity of an observer whose worldline is always normal to the slices Σ.

With n^μ we can proceed constructing the spatial metric $\gamma_{\mu\nu}$ induced by $g_{\mu\nu}$ on Σ:

$$\gamma_{\mu\nu} = g_{\mu\nu} + n_\mu n_\nu. \tag{3.1.4}$$

The tensor $\gamma_{\mu\nu}$ is then a projector which projects out all geometric objects lying along n^μ. We see by contracting with n^μ that $\gamma_{\mu\nu}$ is purely spatial, in fact $n^\mu\gamma_{\mu\nu} = 0$.

We now introduce two projection operators; the first one projects a 4-dimensional tensor into a spatial slice, and can be found raising one index of the spatial metric $\gamma_{\mu\nu}$

$$\gamma^\mu{}_\nu = g^\mu{}_\nu + n^\mu n_\nu = \delta^\mu{}_\nu + n^\mu n_\nu. \tag{3.1.5}$$

The second one is the normal operator, defined as

$$N^\mu{}_\nu \equiv -n^\mu n_\nu = \delta^\mu{}_\nu - \gamma^\mu{}_\nu \tag{3.1.6}$$

To project a higher rank tensor we have to contract any free index with a projection operator. By mean of these projectors we can split any tensor into a purely spatial part, which lies in the hypersurfaces Σ, and a timelike part, normal to the spatial surface.

We will also need a 3-dimensional covariant derivative, and it can be constructed by projecting all the indices of a 4-dimensional covariant derivative into Σ. For a generic tensor it is

$$D_\mu T^{\nu_1\ldots\nu_n}{}_{\rho_1\ldots\rho_n} = \gamma_\mu{}^\kappa \gamma_{\sigma_1}{}^{\nu_1}\ldots\gamma_{\sigma_n}{}^{\nu_n}\gamma^{\eta_1}{}_{\rho_1}\ldots\gamma^{\eta_n}{}_{\rho_n}\nabla_\kappa T^{\sigma_1\ldots\sigma_n}{}_{\eta_1\ldots\eta_n}. \tag{3.1.7}$$

Then, the 3-dimensional Riemann tensor associated with $\gamma_{\mu\nu}$, is given by

$$2D_{[\mu}D_{\nu]}v_\rho = R^\sigma{}_{\rho\nu\mu}v_\sigma \tag{3.1.8}$$

$$R^\sigma{}_{\rho\nu\mu}n_\sigma = 0, \tag{3.1.9}$$

for any spatial vector v_μ.

At this point we need to introduce another quantity called extrinsic curvature. In fact, from the 3-dimensional Riemann tensor we can extract information about the spatial slice Σ and its intrinsic curvature, but we have no information about its shape in the spacetime M. The extrinsic curvature can be found by projecting gradients of the normal vector into the slice Σ. We define it as

$$K_{\mu\nu} = -\gamma_\mu{}^\rho \gamma_\nu{}^\sigma \nabla_\rho n_\sigma. \tag{3.1.10}$$

By definition, the extrinsic curvature is symmetric and purely spatial. It can be easily seen that the extrinsic curvature is the Lie derivative along n^μ of the spatial metric $\gamma_{\mu\nu}$:

$$K_{\mu\nu} = -\frac{1}{2}\mathcal{L}_{\mathbf{n}}\gamma_{\mu\nu}. \tag{3.1.11}$$

The metric $\gamma_{\mu\nu}$ and the extrinsic curvature $K_{\mu\nu}$ cannot be chosen arbitrarily, but they have to satisfy certain constraints so that the spatial slices fit into the spacetime M. To find the relations that they must fulfil, we have to relate the 3-dimensional Riemann tensor of Σ to the four-dimensional one of M. For this purpose we take a completely spatial projection of ${}^{(4)}R^\mu{}_{\nu\rho\sigma}$, a projection with one index projected in the normal direction and a projection with two indices projected in the normal direction. Thanks to the symmetries of the Riemann tensor all the other projections vanish. This three projections give rise to the equations of Gauss, Codazzi and Ricci.

We start writing the definition of the 3-dimensional Riemann tensor

$$R^{\sigma\rho}{}_{\nu\mu} v_\sigma = 2D_{[\mu} D_{\nu]} v^\rho. \tag{3.1.12}$$

Given that

$$D_\mu D_\nu v^\rho = \gamma^a{}_\mu \gamma^b{}_\nu \gamma^\rho{}_c \nabla_a \nabla_b v^c - K_{\mu\nu}\gamma^\rho{}_c n^a \nabla_a v^c - K_\mu{}^\rho K_{\nu a} v^a, \tag{3.1.13}$$

we can substitute this expression into Equation 3.1.12 to find

$$R_{\sigma\rho\nu\mu} v^\sigma = \gamma^a{}_\mu \gamma^b{}_\nu \gamma^c{}_\rho \, {}^{(4)}R_{\sigma cba} v^\sigma - 2K_{\rho[\mu} K_{\nu]\sigma} v^\sigma, \tag{3.1.14}$$

where we used the fact that $K_{\mu\nu}$ is symmetric and we inserted the definition of the 4-dimensional Riemann tensor. Since this relation must hold for any spatial vector v^μ, we have

$$R_{\mu\nu\rho\sigma} + K_{\mu\rho}K_{\nu\sigma} - K_{\mu\sigma}K_{\nu\rho} = \gamma^a{}_\mu \gamma^b{}_\nu \gamma^c{}_\rho \gamma^d{}_\sigma \, {}^{(4)}R_{abcd}. \tag{3.1.15}$$

Equation 3.1.15 is called Gauss' equation. It relates the full spatial projection of ${}^{(4)}R^\mu{}_{\nu\rho\sigma}$ to the 3-dimensional Riemann tensor and terms quadratic in the extrinsic curvature.

The next equation we need can be derived considering a spatial derivative of the extrinsic curvature

$$D_\mu K_{\nu\rho} = \gamma^a{}_\mu \gamma^b{}_\nu \gamma^c{}_\rho \nabla_a K_{bc} = -\gamma^a{}_\mu \gamma^b{}_\nu \gamma^c{}_\rho \left(\nabla_a \nabla_b n_c + \nabla_a \left(n_b a_c\right)\right), \tag{3.1.16}$$

where $a_\mu = n^\nu \nabla_\nu n_\mu$, and we wrote $K_{\mu\nu}$ as $K_{\mu\nu} = -\nabla_\mu n_\nu - n_\mu a_\nu$. Antisymmetrizing the previous equation, and noting that $\gamma^\mu{}_\nu n_\mu = 0$, we get

$$D_\nu K_{\mu\rho} - D_\mu K_{\nu\rho} = \gamma^a{}_\mu \gamma^b{}_\nu \gamma^c{}_\rho n^d \, {}^{(4)}R_{abcd}. \tag{3.1.17}$$

This is known as the Codazzi's equation. Equations 3.1.15 and 3.1.17 depends only on the spatial metric, the extrinsic curvature and their spatial derivative; they can be thought as the integrability conditions which allow the embedding of a spatial slice inside a 4-dimensional manifold. It is clear that we need one more equation to describe the time evolution of our quantities.

Let's consider the remaining projection of the 4-dimensional Riemann tensor, the one with two indices projected in the normal direction. We begin with the Lie derivative of $K_{\mu\nu}$

$$\mathcal{L}_{\mathbf{n}} K_{\mu\nu} = n^\rho \nabla_\rho K_{\mu\nu} + 2 K_{\rho(\mu} \nabla_{\nu)} n^\rho. \tag{3.1.18}$$

Inserting the definition of ${}^{(4)}R^\mu{}_{\nu\rho\sigma}$ and of $K_{\mu\nu}$ as we did in Equation 3.1.16, we can simplify the expression on the right-hand side to obtain

$$\mathcal{L}_{\mathbf{n}} K_{\mu\nu} = -n^\sigma n^\rho \, {}^{(4)}R_{\sigma\nu\mu\rho} - \nabla_\mu a_\nu - n^\rho n_\mu \nabla_\rho a_\nu - a_\mu a_\nu - K^\rho{}_\nu K_{\mu\rho} - K_{\rho\mu} n_\nu a^\rho. \tag{3.1.19}$$

This expression can be further simplified projecting the two free indices and using the fact that $D_\mu a_\nu = -a_\mu a_\nu + \frac{1}{\alpha} D_\mu D_\nu \alpha$, with α the lapse function. Since the left-hand side is purely spatial, the projection leaves it unchanged. We finally get

$$\mathcal{L}_{\mathbf{n}} K_{\mu\nu} = n^\sigma n^\rho \gamma^a{}_\mu \gamma^b{}_\nu \, {}^{(4)}R_{\sigma a \rho b} - \frac{1}{\alpha} D_\mu D_\nu \alpha - K^\rho{}_\nu K_{\mu\rho}. \tag{3.1.20}$$

Equation 3.1.20 is Ricci's equation, which relates the time derivative of the extrinsic curvature to a projection of the 4-dimensional Riemann tensor with two indices projected in the time direction.

At this point we have the three fundamental equations that we need to cast Einstein's field equations in the 3+1 formalism. What we have to do then is to use the equations of Gauss, Codazzi and Ricci to rewrite the 4-dimensional Riemann tensor in terms of the 3-dimensional one into EE. We need to use EE as we were dealing only with geometry, while now we want to link the geometry of spacetime to physics. After some steps one finds

$$R + K^2 - K_{\mu\nu} K^{\mu\nu} = 16\pi\rho, \tag{3.1.21}$$

$$D_\nu K^\nu{}_\mu - D_\mu K = 8\pi J_\mu, \tag{3.1.22}$$

$$\begin{aligned}\mathcal{L}_{\mathbf{t}} K_{\mu\nu} = &-D_\mu D_\nu \alpha + \alpha \left(R_{\mu\nu} - 2K_{\mu\rho}K^\rho{}_\nu + K K_{\mu\nu}\right) \\ &-8\pi\alpha\left(S_{\mu\nu} - \frac{1}{2}\gamma_{\mu\nu}\left(S-\rho\right)\right) + \mathcal{L}_\beta K_{\mu\nu}\end{aligned} \tag{3.1.23}$$

and

$$\mathcal{L}_{\mathbf{t}} \gamma_{\mu\nu} = -2\alpha K_{\mu\nu} + \mathcal{L}_\beta \gamma_{\mu\nu}. \tag{3.1.24}$$

Equation 3.1.21 is the Hamiltonian constraint. We have defined the energy density ρ to be the total energy density as measured by a normal observer n^μ, $\rho \equiv n_\mu n_\nu T^{\mu\nu}$. Equation 3.1.22 is the momentum constraint. The quantity J_μ is the momentum density, also measured by a normal observer, and it is defined as $J_\mu \equiv -\gamma^\nu{}_\mu n^\rho T_{\nu\rho}$. Equation 3.1.23 is the evolution equation for the extrinsic curvature, and $S_{\mu\nu} \equiv \gamma^\rho{}_\mu \gamma^\sigma{}_\nu T_{\rho\sigma}$ is the spatial stress-energy tensor, with S being its trace.
Equation 3.1.24 is the evolution equation for the spatial metric.

Note that in both the evolution equations 3.1.23 and 3.1.24 the Lie derivative is not along $\mathbf{n}$, which would not lead to a "natural" time derivative. We use instead $t^\mu = \alpha n^\mu + \beta^\mu$, such that $t^\mu \Omega_\mu = 1$ for any vector β^μ, which is called shift vector. In this way we are connecting neighbouring spatial slices (i.e. Σ_t with Σ_{t+dt}), as the change in t along the vector t^μ is $dt = t^\mu \nabla_\mu t = 1$ for every point on Σ_t.

Equations 3.1.21, 3.1.22, 3.1.23 and 3.1.24 together are completely equivalent to Einstein's field equations.

3.1.2 ADM equations

The equations we derived in the previous section can be simplified choosing a particular coordinate basis. We introduce a basis of three spatial vectors $e^\mu_{(i)}$ $(i = 1, 2, 3)$ that reside in a particular time slice Σ, such that

$$\Omega_\mu e^\mu_{(i)} = 0. \tag{3.1.25}$$

To extend them to other slices we Lie drag them along t^μ. As the fourth basis vector we pick $e^\mu_{(0)} = t^\mu = (1, 0, 0, 0)$. This means that the Lie derivative along t^μ reduces to a partial derivative with respect to t: $\mathcal{L}_{\mathbf{t}} = \partial_t$.

As $e^\mu_{(i)}$ span Σ, Equation 3.1.25 implies that the covariant spatial components of the normal vector have to vanish, $n_i = 0$. This also means that all components of a spatial tensor with a contravariant index equal to zero must vanish, for example

$$\beta^\mu = \left(0, \beta^i\right). \tag{3.1.26}$$

From the definition of $t^\mu = \alpha n^\mu + \beta^\mu$ we find

$$n^\mu = \left(\alpha^{-1}, -\alpha^{-1}\beta^i\right), \tag{3.1.27}$$

and since $n_\mu n^\mu = 1$

$$n_\mu = (-\alpha, 0, 0, 0)\,. \tag{3.1.28}$$

It follows that

$$\gamma_{ij} = g_{ij}, \tag{3.1.29}$$

so the metric on Σ is the spatial part of the full metric. As the zeroth components of a spatial contravariant tensor have to vanish we also have $\gamma^{\mu 0} = 0$. The inverse metric is then

$$g^{\mu\nu} = \gamma^{\mu\nu} - n^\mu n^\nu = \begin{pmatrix} -\alpha^{-2} & \alpha^{-2}\beta^i \\ \alpha^{-2}\beta^j & \gamma^{ij} - \alpha^{-2}\beta^i\beta^j \end{pmatrix}. \tag{3.1.30}$$

Inverting the previous expression we find the components of the four dimensional metric

$$g_{\mu\nu} = \begin{pmatrix} -\alpha^2 + \beta_\lambda\beta^\lambda & \beta_i \\ \beta_j & \gamma_{ij} \end{pmatrix}. \tag{3.1.31}$$

Moreover, as $\gamma^{ik}\gamma_{kj} = \delta^i{}_j$, γ_{ij} can be used to raise and lower spatial indices of spatial tensors.

The line element then can be written as

$$ds^2 = -\alpha^2 dt^2 + \gamma_{ij}\left(dx^i + \beta^i dt\right)\left(dx^j + \beta^j dt\right), \tag{3.1.32}$$

which is the metric in the 3+1 form.

As a consequence of the choice of the coordinate basis we did, the entire content of any spatial tensor is available from their spatial components. This is obviously true for contravariant components, as the 0-component vanishes, but it holds for covariant components too. By mean of these considerations, we can rewrite EE in the 3+1 formalism in a simplified form. The Hamiltonian constraint 3.1.21 becomes

$$R + K^2 + K_{ij}K^{ij} = 16\pi\rho, \tag{3.1.33}$$

while the momentum constraint 3.1.22 is

$$D_j\left(K^{ij} - \gamma^{ij}K\right) = 8\pi J^i. \tag{3.1.34}$$

The evolution equation for the extrinsic curvature 3.1.23 can be rewritten as

$$\begin{aligned} \partial_t K_{ij} = &-D_i D_j\alpha + \alpha\left(R_{ij} - 2K_{ik}K^k{}_j + KK_{ij}\right) \\ &-8\pi\alpha\left(S_{ij} - \frac{1}{2}\gamma_{ij}\left(S - \rho\right)\right) + \beta^k D_k K_{ij} \qquad (3.1.35) \\ &+K_{ik}D_j\beta^k + K_{kj}D_i\beta^k, \qquad (3.1.36) \end{aligned}$$

while the evolution equation for the spatial metric 3.1.24 becomes

$$\partial_t\gamma_{ij} = -2\alpha K_{ij} + D_i\beta_j + D_j\beta_i. \tag{3.1.37}$$

Equations 3.1.33, 3.1.34, 3.1.35 and 3.1.37 are called ADM equations after Arnowitt, Deser and Misner.

3.1.3 BSSNOK formalism

The ADM formulation of EE unfortunately does not behave very well on long simulations. If fact, due to the mathematical structure of the equations, they tend to form instabilities and lead the code to crash. In the 80s and 90s several groups worked to new formalism to develop a formulation of the EE more stable for long term simulations. The new formalism is known as the BSSNOK from its authors (Baumgarte, Shapiro, Shibata, Nakamura, Oohara and Kojima). To derive this formulation we start introducing the conformal metric $\bar{\gamma}_{ij}$ defined as

$$\bar{\gamma}_{ij} = e^{-4\phi}\gamma_{ij}. \tag{3.1.38}$$

We require the determinant of the conformal metric to be equal to the determinant of the flat metric η_{ij}, i.e.

$$\phi = \frac{1}{12}\ln\left(\frac{\gamma}{\eta}\right). \tag{3.1.39}$$

We will adopt a Cartesian coordinate system, such that $\bar{\gamma} = \eta = 1$.

We define the traceless extrinsic curvature as

$$A_{ij} \equiv K_{ij} - \frac{1}{3}\gamma_{ij}K, \tag{3.1.40}$$

and its conformally related tensor as

$$\bar{A}_{ij} = e^{-4\phi}A_{ij}. \tag{3.1.41}$$

From Equations 3.1.37 and 3.1.35 we find the evolution equations for ϕ and K, which are

$$\partial_t\phi = -\frac{1}{6}\alpha K + \beta^i\partial_i\phi + \frac{1}{6}\partial_i\beta^i \tag{3.1.42}$$

and

$$\partial_t K = -\gamma^{ij}D_jD_i\alpha + \alpha\left(\bar{A}_{ij}\bar{A}^{ij} + \frac{1}{3}K^2\right) + 4\pi\alpha\left(\rho + S\right) + \beta^i\partial_i K. \tag{3.1.43}$$

Subtracting 3.1.42 from 3.1.37 and 3.1.35 from 3.1.23 leaves the traceless part of the evolution equations for $\bar{\gamma}_{ij}$ and $\bar{A}_{ij}$:

$$\partial_t\bar{\gamma}_{ij} = -2\alpha\bar{A}_{ij} + \beta^k\partial_k\bar{\gamma}_{ij} + \bar{\gamma}_{ik}\partial_j\beta^k + \bar{\gamma}_{kj}\partial_i\beta^k - \frac{2}{3}\bar{\gamma}_{ij}\partial_k\beta^k, \tag{3.1.44}$$

$$\begin{aligned}\partial_t\bar{A}_{ij} = e^{-4\phi}\left[-\left(D_iD_j\alpha\right) + \alpha\left(R_{ij} - 8\pi S_{ij}\right)\right]^{\mathrm{TF}} + \alpha\left(K\bar{A}_{ij} - 2\bar{A}_{il}\bar{A}^l{}_j\right)\\ +\beta^k\partial_k\bar{A}_{ij} + \bar{A}_{ik}\partial_j\beta^k + \bar{A}_{kj}\partial_i\beta^k - \frac{2}{3}\bar{A}_{ij}\partial_k\beta^k.\end{aligned} \tag{3.1.45}$$

The superscript TF denotes the trace-free part of a tensor, e.g. $T_{ij}^{\rm TF} = T_{ij} - \gamma_{ij}T/3$.

Finally, to complete the BSSNOK formulation, we introduce a new quantity Γ^i, defined as

$$\bar{\Gamma}^i \equiv \bar{\gamma}^{jk}\bar{\Gamma}^i_{jk}, \tag{3.1.46}$$

where $\bar{\Gamma}^i_{jk}$ are the connection coefficients associated with $\bar{\gamma}_{ij}$. From the definition of the Ricci tensor, using the transformation law 3.1.38, we find that R_{ij} can be written as

$$\bar{R}_{ij} = \bar{R}_{ij} + R^{\phi}_{ij}, \tag{3.1.47}$$

where $\bar{R}_{ij}$ is the conformal Ricci tensor and R^{ϕ}_{ij} is a function of ϕ only. If we formally compute the Ricci tensor from the definition we would end up with mixed second derivatives which we want to avoid to maintain the stability of the code. Thanks to the new variable $\bar{\Gamma}^i$ we can write the Ricci tensor masking the second derivatives behind first derivatives of $\bar{\Gamma}^i$. The Ricci tensor then becomes

$$\bar{R}_{ij} = -\frac{1}{2}\bar{\gamma}^{lm}\partial_m\partial_l\bar{\gamma}_{ij} + \bar{\gamma}_{k(i}\partial_{j)}\bar{\Gamma}^k + \bar{\Gamma}^k\bar{\Gamma}_{(ij)k} + \bar{\gamma}^{lm}\left(2\bar{\Gamma}^k_{l(i}\bar{\Gamma}_{j)km} + \bar{\Gamma}^k_{im}\bar{\Gamma}_{klj}\right). \tag{3.1.48}$$

Having introduced a new independent variable, we need an evolution equation to evolve it. As in Cartesian coordinates it holds that

$$\bar{\Gamma}^i = -\partial_j\bar{\gamma}^{ij}, \tag{3.1.49}$$

we can easily derive the evolution equation for $\bar{\Gamma}^i$, inverting spatial with time derivative in 3.1.44 and using the momentum constraint 3.1.34 to simplify. We find

$$\begin{aligned}\partial_t\bar{\Gamma}^i = &-2\bar{A}^{ij}\partial_j\alpha + 2\alpha\left(\bar{\Gamma}^i_{jk}\bar{A}^{kj} - \frac{2}{3}\bar{\gamma}^{ij}\partial_j K - 8\pi\bar{\gamma}^{ij}J_j + 6\bar{A}^{ij}\partial_j\phi\right)\\ &+\beta^j\partial_j\bar{\Gamma}^i - \bar{\Gamma}^j\partial_j\beta^j + \frac{2}{3}\bar{\Gamma}^i\partial_j\beta^j + \frac{1}{3}\bar{\gamma}^{li}\partial_l\partial_j\beta^j + \bar{\gamma}^{lj}\partial_j\partial_l\beta^i.\end{aligned} \tag{3.1.50}$$

Evolution equations 3.1.42, 3.1.43, 3.1.44, 3.1.45 and 3.1.50, together with the constraint 3.1.33, 3.1.34 and 3.1.49, make the BSSNOK formulation of EE. As already pointed out, this formulation in completely equivalent to the ADM formulation, but it performs better in numerical implementation and remains stable where the other fails.

3.1.4 Gauge conditions

In the previous sections we derived the Einstein's field equations in the 3+1 formalism, and we have seen that these can be split into two constraint equations and two evolutions equations. The constraint equations relate quantities on a given $t =$ constant spacelike hypersurface, while the evolution equations contain first-order

time derivatives and they describe how the fields change from one hypersurface to the next one. By the way these equations are not ready for numerical integrations; we note that the evolution equations depend on the lapse function α and the shift vector β^μ, which must be specified. In fact, we have to impose coordinate conditions, since α and β^μ are two gauge variables that need to be chosen arbitrarily. The choice we make will affect the performance of the code. In particular, we have to avoid singularities. If a singularity arises in our spacetime, the result will be one or more field variables blowing up to infinities, leading to underflows and overflows in the output and eventually causing the code to crash (unless the code is designed to managed singularities).

As an example let's consider the simplest possible choice:

$$\alpha = 1,\ \beta^i = 0. \tag{3.1.51}$$

This gauge choice is called geodesic slicing, and the resulting coordinates are known as Gaussian normal coordinates. The coordinate observers move with four-velocity $u^\mu = t^\mu$ and, since $\beta^i = 0$, they coincide with normal observers (as $u^\mu = n^\mu$). Since their acceleration in given by $a_\mu = D_\mu \ln \alpha$ and thus is equal to zero, normal observers are freely falling and so they follow geodesics, hence the name of this gauge. The problem of this choice is evident as geodesics tend to focus in the presence of a gravitational field source. Observers approach to each other and collide, forming a coordinate singularity. This can be see from the evolution equation for the trace of the extrinsic curvature (assuming geodesic slicing and a comoving perfect fluid)

$$\partial_t K = K_{ij} K^{ij} + 4\pi \left(\rho + 3P\right) \geq 0, \tag{3.1.52}$$

from which we see that K grows monotonically in time. The expansion of normal observers

$$\nabla_\mu n^\mu = -K, \tag{3.1.53}$$

then decreases in time. The evolution equation for the metric gives

$$\partial_t \ln \gamma^{1/2} = -K, \tag{3.1.54}$$

which shows that the coordinate volume element goes to zero with the growth of K. This will result in a coordinate singularity.

Modern numerical simulations adopt a hyperbolic slicing condition knows as Bona-Massò slicing [49], which in general can be written as

$$\partial_t \alpha - \beta^k \partial_k \alpha = -f\left(\alpha\right) \alpha^2 \left(K - K_0\right), \tag{3.1.55}$$

where $K_0 \equiv K\left(t = 0\right)$ and $f\left(\alpha\right) > 0$. For $f = p/\alpha$ we get the so-called "1-log" slicing condition, where p is an integer (an usual choice is $p = 2$) and $\alpha = h\left(x^i\right) + \ln \gamma^{p/2}$, with $h\left(x^i\right)$ a positive function.

For the shift vector an usually implemented condition is the hyperbolic Gamma-driver [50], given by

$$\partial_t^2 \beta^i = k \partial_t \bar{\Gamma}^i - (\eta - \partial_t k)\, \partial_t \beta^i, \tag{3.1.56}$$

where η is a damping term introduced to avoid strong oscillations in the shift vector due to rapid and large gauge variations.

3.2 The sources of gravitational field

In the previous section we dealt with the geometry of spacetime. Now we need to consider the source term and develop a set of equations to evolve it in numerical simulations. Many properties of relativistic stars are described by a hydrodynamic fluid, and since our framework consists into two highly magnetized NSs, we will need a general relativistic formulation of magnetohydrodynamics.

3.2.1 Relativistic hydrodynamics

Let's consider the stress-energy tensor of a perfect gas

$$T^{\mu\nu} = \rho_0 h u^\mu u^\nu + p g^{\mu\nu}, \tag{3.2.1}$$

where u^μ is the fluid 4-velocity, ρ_0 is the rest-mass density, p is the pressure and $h = 1 + \epsilon + p/\rho_0$ is the specific enthalpy, with ϵ being the specific internal energy density. The total mass-energy density as measured by a comoving observer is given by $\rho = \rho_0 (1 + \epsilon)$.

The equations of motion governing the fluid can be derived by the local conservation laws for energy-momentum

$$\nabla_\mu T^{\mu\nu} = 0, \tag{3.2.2}$$

and for rest mass

$$\nabla_\mu (\rho_0 u^\mu) = 0. \tag{3.2.3}$$

The solutions of these equations can be cast in different forms, depending on the variables chosen for numerical integration. One of the most straightforward schemes is the Wilson scheme, introduced by Wilson in 1972 [51]. It easily lends itself to numerical integration, however it is a non-conservative formulation and it needs to be modified to handle the appearance of shock discontinuities, which arise for example in stellar collapses.

Wilson introduced a rest-mass density variable

$$D \equiv \rho_0 u^t, \tag{3.2.4}$$

an internal energy density variable

$$E \equiv \rho_0 u^t \epsilon, \tag{3.2.5}$$

and a momentum density variable

$$S_\mu \equiv \rho_0 h u^t u_\mu. \tag{3.2.6}$$

The conservation laws can be recast in terms of these new variables as

$$\frac{1}{\sqrt{-g}}\partial_t\left(\sqrt{-g}D\right) + \frac{1}{\sqrt{-g}}\partial_i\left(\sqrt{-g}Dv^i\right) = 0 \tag{3.2.7}$$

and

$$\partial_t\left(\sqrt{-g}E\right) + \partial_i\left(\sqrt{-g}Ev^i\right) + p\partial_\mu\left(\sqrt{-g}u^t v^\mu\right) = 0, \tag{3.2.8}$$

$$\frac{1}{\sqrt{-g}}\partial_t\left(\sqrt{-g}S_\mu\right) + \frac{1}{\sqrt{-g}}\partial_i\left(\sqrt{-g}S_\mu v^i\right) + \partial_\mu p + \frac{1}{2}\left(\partial_\mu g^{\alpha\beta}\right)\left(\frac{S_\alpha S_\beta}{S^t}\right), \tag{3.2.9}$$

where $v^i = u^i/u^t$ is the fluid 3-velocity with respect to a coordinate observer and $v^0 = 1$. As pointed out previously, this formalism requires the addition of an artificial viscosity term to lead to stable solutions in the presence of discontinuities like shock waves. Due to the non-linear coupling of the artificial viscosity with the fluid velocity, the addition of such term could not be sufficient to produce satisfactory results for ultra-relativistic flows.

A different approach to handle shocks involves recasting the equations in a flux-conservative form, adopting a "high resolution shock-capturing scheme" [52]. Such schemes can manage shock waves without the need of introducing artificial viscosity. One divides the spatial domain into a set of contiguous cells, keeping track of the fluid variables at the centre of each cell as they evolve. The variables are treated as constants in each cell, while the discontinuous fluid variables at the grid interfaces serve as initial conditions for a local Riemann shock tube problem. The solution to this idealized problem is known [53], and this has motivated the development of flux-conservative schemes.

In such formalisms the conservation laws are written as

$$\partial_t \mathcal{U} + \partial_i \mathcal{F}^i = \mathcal{S}, \tag{3.2.10}$$

where $\mathcal{U}$ is the state vector of conserved variables built out of the primitive fluid variables (ρ_0, v^i, p), $\mathcal{F}^i$ are the flux vectors and $\mathcal{S}$ is the source vector which does not contain any derivatives of the fluid variables, which is a key feature of flux-conservative schemes.

To evolve the system we have to integrate Equations 3.2.10 from the time t to $t + \Delta t$, and extract the primitive fluid variables at the new time from the evolved conserved variables. This has to be done simultaneously with the integration of the 3+1 EE to determine a self-consistent background gravitational field.

Valencia formulation A useful choice of conserved variables was introduced by Martí, Ibáez and Miralles [54] and is known as the "Valencia" formulation. This formulation is the one implemented in the Whisky code used in our simulations [55]. The primitive variables (the rest mass-density ρ_0, the pressure p, the fluid 3-velocity v^i, the internal energy ϵ and the Lorentz factor W) are mapped into the following conserved quantities

$$D \equiv \sqrt{\gamma} W \rho_0, \tag{3.2.11}$$

$$S_j \equiv \sqrt{\gamma} \alpha T^0_{\ j}, \tag{3.2.12}$$

and

$$\tau = \sqrt{\gamma} \alpha^2 T^{00} - D, \tag{3.2.13}$$

where γ is the determinant of the spatial metric and $T^{\mu\nu}$ is the stress-energy tensor for a perfect fluid (Equation 3.2.1). The Lorentz factor between the normal and fluid observer W is defined as $W = -n^\mu u_\mu$ and satisfies $W = (1 - \gamma_{ij} v^i v^j)^{-1/2}$. With this choice the equations of motions are described by 3.2.10 with

$$\mathcal{U} = \begin{pmatrix} D \\ S_j \\ \tau \end{pmatrix} \tag{3.2.14}$$

and the flux vectors $\mathcal{F}^i$ and the source vector $\mathcal{S}$ given by

$$\mathcal{F}^i = \begin{pmatrix} D v^i \\ \alpha \sqrt{\gamma} T^i_{\ j} \\ \alpha^2 \sqrt{\gamma} T^{0i} - D v^i \end{pmatrix} \tag{3.2.15}$$

$$\mathcal{S} = \begin{pmatrix} 0 \\ \frac{1}{2} \alpha \sqrt{\gamma} T^{\rho\sigma} \partial_j g_{\rho\sigma} \\ \alpha \sqrt{\gamma} \left(T^{\rho 0} \partial_\rho \alpha - {}^{(4)}\Gamma^0_{\rho\sigma} T^{\rho\sigma} \alpha \right). \end{pmatrix} \tag{3.2.16}$$

This formulation provides robustness and stability, and thus is widely implemented in modern numerical simulations.

3.2.2 Electromagnetic field dynamics

Another contribution to the sources of gravitational field comes from the electromagnetic (EM) field, which play a crucial role in NSs and BNSs dynamics. The EM field is completely described by the Faraday tensor $F^{\mu\nu}$ and Maxwell's equations

$$\nabla_\nu F^{\mu\nu} = 4\pi \mathcal{J}^\mu \tag{3.2.17}$$

and

$$\nabla_\nu {}^*F^{\mu\nu} = 0, \tag{3.2.18}$$

where $\mathcal{J}^\mu$ is the charge current and ${}^*F^{\mu\nu}$ is the dual of $F^{\mu\nu}$ defined as

$$ {}^*F^{\mu\nu} = \frac{1}{2}\varepsilon^{\mu\nu\rho\sigma}F_{\rho\sigma}, \tag{3.2.19} $$

with $\varepsilon^{\mu\nu\rho\sigma}$ being the Levi-Civita tensor. The charge current $\mathcal{J}^\mu$ in general can be written as

$$ \mathcal{J}^\mu = qu^\mu + \sigma F^{\mu\nu}u_\nu, \tag{3.2.20} $$

where q is the charge density of the fluid moving with 4-velocity u^μ and σ is the electric conductivity. In our model we assume perfect conductivity ($\sigma \to \infty$) such that $F^{\mu\nu}u_\nu = 0$ (i.e. the electric field measured by a comoving observer is zero). In this limit the Faraday tensor can be expressed exclusively in term of the magnetic field b^μ measured in the comoving frame

$$ F^{\mu\nu} = \varepsilon^{\alpha\beta\mu\nu}b_\alpha u_\beta, \tag{3.2.21} $$

$$ {}^*F^{\mu\nu} = b^\mu u^\nu - b^\nu u^\mu, \tag{3.2.22} $$

and Maxwell's equations become

$$ \nabla_\nu {}^*F^{\mu\nu} = \frac{1}{\sqrt{g}}\partial_\nu\left(\sqrt{g}\left(b^\mu u^\nu - b^\nu u^\mu\right)\right) = 0. \tag{3.2.23} $$

We need a relation between the magnetic field measured by a comoving observer and the quantities measured by a normal observer (with 4-velocity n^μ), which are given by

$$ E^\mu = F^{\mu\nu}n_\nu \tag{3.2.24} $$

and

$$ B^\mu = {}^*F^{\mu\nu}n_\nu. \tag{3.2.25} $$

The relation we look for is [56]

$$ \mathcal{B}^i = \sqrt{4\pi\gamma}W\left(b^i - v^i b^t\right), \tag{3.2.26} $$

in which $\mathcal{B}^i = \sqrt{\gamma}B^i$, $v^i = u^i/u^t$ and $v^0 = 1$. The time component of Equation 3.2.23 yields the divergence-free condition for the magnetic field

$$ \partial_i \mathcal{B}^i = 0, \tag{3.2.27} $$

while the spatial part gives

$$ \partial_t \mathcal{B}^i = \partial_j\left(v^i\mathcal{B}^j - v^j\mathcal{B}^i\right), \tag{3.2.28} $$

which is the magnetic field evolution equation.

3.3 Relativistic magnetohydrodynamics

Now that we have a relativistic formulation for both hydrodynamics and EM field dynamics we can write down the complete set of equation that we need to evolve our system. We consider a perfect fluid in the ideal conductor limit, and we adopt the metric 3.1.32. The stress-energy tensor will be given by

$$T^{\mu\nu} = T^{\mu\nu}_{\text{perfect fluid}} + T^{\mu\nu}_{\text{EM}}, \tag{3.3.1}$$

with

$$T^{\mu\nu}_{\text{perfect fluid}} = \rho_0 h u^\mu u^\nu + p g^{\mu\nu} \tag{3.3.2}$$

and

$$T^{\mu\nu}_{\text{EM}} = b^2 u^\mu u^\nu + \frac{1}{2} b^2 g^{\mu\nu} - b^\mu b^\nu. \tag{3.3.3}$$

The evolution equations follow from 3.2.2, 3.2.3 and 3.2.28. As in [57], we will rewrite them in the conservative form

$$\frac{1}{\sqrt{-g}} \left[\partial_t \left(\sqrt{\gamma} \mathcal{U} \right) + \partial_i \left(\sqrt{-g} \mathcal{F}^i \right) \right] = \mathcal{S}, \tag{3.3.4}$$

with $\mathcal{U}$, $\mathcal{F}^i$ and $\mathcal{S}$ given by

$$\mathcal{U} = \begin{pmatrix} D \\ S_j \\ \tau \\ B^k \end{pmatrix}, \tag{3.3.5}$$

$$\mathcal{F}^i = \begin{pmatrix} D v^i/\alpha \\ S_j v^i/\alpha + (p + b^2/2)\, \delta^i{}_j - b_j B^i/W \\ \tau v^i/\alpha + (p + b^2/2)\, \tilde{v}^i - \alpha b^0 B^i/W \\ B^k v^i/\alpha - B^i v^k/\alpha \end{pmatrix}, \tag{3.3.6}$$

$$\mathcal{S} = \begin{pmatrix} 0 \\ T^{\mu\nu} \left(\partial_\mu g_{\nu j} - \Gamma^\rho_{\nu\mu} g_{\rho j} \right) \\ \alpha \left(T^{\mu 0} \partial_\mu \ln \alpha - T^{\mu\nu} \Gamma^0_{\nu\mu} \right) \\ 0^k \end{pmatrix}, \tag{3.3.7}$$

where we have defined the conserved variables

$$D \equiv \rho_0 W, \tag{3.3.8}$$

$$S_j \equiv \left(\rho_0 h + b^2 \right) W^2 \tilde{v}_j - \alpha b^0 b_j, \tag{3.3.9}$$

$$\tau \equiv \left(\rho_0 h + b^2 \right) W^2 - \left(p + \frac{b^2}{2} \right) - \alpha^2 \left(b^0 \right)^2 - D, \tag{3.3.10}$$

and $0^k = (0,0,0)^{\mathrm{T}}$. The quantity $\tilde{v}^i = \frac{\left(g^i{}_\mu + n^i n_\mu \right) u^\mu}{-u^\mu n_\mu}$ is the 3-velocity of the fluid as measured by a normal observer.

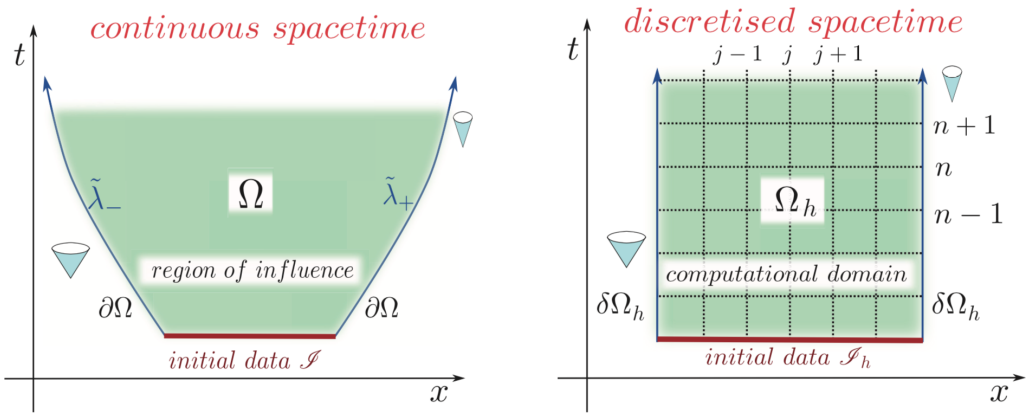

Figure 3.2: Schematic representation of the discretization of spacetime for an initial value problem. On the left: continuous spacetime with solutions Ω, with edges $\partial\Omega$ marking the limits of the region of influence. On the right: discretized spacetime and space of solutions Ω_h, whose edges $\delta\Omega_h$ are timelike boundaries in causal contact with the solution [48].

3.4 Numerical methods

In this section we will review some numerical methods usually employed in simulations. As we pointed out at the beginning of this chapter, the non-linear nature of the Einstein's field equations, together with the magnetohydrodynamics equations, does not allow us to find analytical solutions. Moreover, the non-linearity of the equations results in the natural onset of discontinuities during the evolution. Discontinuities represent an issue in some numerical approaches; in fact, we need appropriate methods to manage them, otherwise our code will produce unphysical results. We will focus on the so called grid-based methods, which compute and evolve hydrodynamical equations on a discretized spacetime.

We start introducing the discretization of spacetime and some useful concepts.

For the spacetime, discretization is performed on space and time separately after the foliation process (Figure 3.2). We have

$$t^n \equiv t^0 + n\Delta t, \qquad n = 0, 1, \ldots, N_y \tag{3.4.1}$$

and

$$x_j \equiv x_0 + j\Delta x, \qquad j = 0, 1, \ldots, J, \tag{3.4.2}$$

where Δt is the separation between two spacelike slices, Δx is a function of space and time and the set x_j makes the gridpoints. A continuous function $u\,(x,t)$ can be discretized to a set of values u_j^n, such that

$$u_j^n \approx u\left(x_j^n\right) = u\,(x_j, t^n) \equiv U_j^n. \tag{3.4.3}$$

This means that we take a discrete set of values u_j^n that approximate the exact value U_j^n of the function u at the gridpoints x_j^n. For a continuous differential operator we have $\mathcal{L}(u) \rightarrow L_h\left(u_j^n\right)$. The discretized one-norm is defined as

$$||u(t^n)||_1 = \frac{1}{J}\sum_{j=0}^{J}\left|u_j^n\right|, \tag{3.4.4}$$

Before introducing the concept of convergence we want to define consistency and stability. Let us consider a generic system of PDE in the form

$$\mathcal{L}(u) = \mathcal{F}, \tag{3.4.5}$$

described by a given grid-scheme $(\Delta x, \Delta t)$, such that

$$\mathcal{L}(u) = \mathcal{F} \quad \rightarrow \quad L_h\left(u_j^n\right) = F_h. \tag{3.4.6}$$

The scheme is globally consistent [58] if

$$\epsilon_h = \left|\left|L_h\left(U_j^n\right) - F_h\right|\right|_1 \rightarrow 0 \quad \text{for} \quad \Delta x, \Delta t \rightarrow 0. \tag{3.4.7}$$

In the previous expression, ϵ_h is called truncation error. With $h \equiv \Delta x \sim \Delta t$ we indicate a generic discretization interval as most discretization methods require that time and spatial discretization are comparable. We then say that a scheme is consistent if the truncation error is zero in the limit of vanishing grid-spacing. The scheme is said to be stable if there exists a constant K and a value h_0 such that

$$||L_h^n||_1 \leq K, \quad \text{for all} \quad nh \leq T;\, h < h_0 \tag{3.4.8}$$

for each time $T = t^n$, where with L_h^n we indicate the n-th application of the operator L_h. What we require for a scheme to be stable is that the application of this operator should be such that the error accumulated does not grow unbounded.

Finally, L_h satisfies the global convergence criterion if

$$\lim_{h\rightarrow 0}\left|\left|E_j^{(h)}\right|\right|_1 = \lim_{h\rightarrow 0} Kh^p = 0, \tag{3.4.9}$$

where p is the global convergence order, K is a real constant and $E_j^{(h)} = U_j - u_j^{(h)}$ is the global error. The Lax equivalence theorem states that for a consistent finite difference method for a well-posed linear initial value problem, the method is convergent if and only if it is stable.

3.4.1 Finite differences methods

The most used grid-based methods are finite difference methods. This class of methods are based on the fact that the solution to the PDE at a specific point of spacetime can be Taylor expanded around the point itself; all the derivatives can then be expressed as differences between values at neighbouring gridpoints.

To ensure stability of a finite difference method, we have to choose an appropriate time-step Δt. In fact, the numerical domain of dependence of any point in space and time must include the analytical domain of dependence to assure that the scheme can access the information required to form the solution. This choice is regulated by the Courant–Friedrichs–Lewy (CFL) condition, which in one dimension is

$$C = \frac{u\Delta t}{\Delta x} \leq C_{\max}, \tag{3.4.10}$$

where u is the propagation speed of the solutions of the PDE. C is called the Courant factor, while $C_{\max}$ depends on the method employed (usually $C_{\max} = 1$).

The first finite difference scheme we discuss is the upwind scheme. Let's consider the one-dimensional scalar advection equation

$$\partial_t u + \lambda \partial_x u = 0, \tag{3.4.11}$$

where λ is the advection velocity and $u = u_0 (x - \lambda t)$ a general solution. By Taylor expanding the solution around (x_j, t^n) we find

$$u (x_j, t^n + \Delta t) = u (x_j, t^n) + \partial_t u (x_j, t^n) \Delta t + \mathcal{O}\left(\Delta t^2\right), \tag{3.4.12}$$

and after discretization it becomes

$$u_j^{n+1} = u_j^n + \partial_t u|_j^n \Delta t + \mathcal{O}\left(\Delta t^2\right). \tag{3.4.13}$$

Equation 3.4.13 yields the first-order finite difference approximation for the time derivative as

$$\partial_t u|_j^n = \frac{u_j^{n+1} - u_j^n}{\Delta t} + \mathcal{O}(\Delta t). \tag{3.4.14}$$

In the same way we can obtain a first-order approximation for the spatial derivative; we find

$$\partial_x u|_j^n = \frac{u_{j+1}^n - u_j^n}{\Delta x} + \mathcal{O}(\Delta x). \tag{3.4.15}$$

$$\partial_x u|_j^n = \frac{u_j^n - u_{j-1}^n}{\Delta x} + \mathcal{O}(\Delta x). \tag{3.4.16}$$

Here we have an ambiguity, unlike the time derivative, as the first-order term can be expressed in terms of u_{j+1}^n or equivalently in terms of u_j^n. In the case in exam, since

the transport properties are known, the ambiguity is easily removed considering that each point in the initial solution translates to a new one $x + \lambda\Delta t$ over the time interval Δt. Depending on the sign of λ we have then two finite-difference representation of Equation 3.4.11

$$\frac{u_j^{n+1} - u_j^n}{\Delta t} = -\lambda \left(\frac{u_j^n - u_{j-1}^n}{\Delta x} \right) + \mathcal{O}\left(\Delta t, \Delta x\right) \quad \text{for} \quad \lambda > 0, \tag{3.4.17}$$

$$\frac{u_j^{n+1} - u_j^n}{\Delta t} = -\lambda \left(\frac{u_{j+1}^n - u_j^n}{\Delta x} \right) + \mathcal{O}\left(\Delta t, \Delta x\right) \quad \text{for} \quad \lambda < 0. \tag{3.4.18}$$

Then, the finite-difference algorithms to determine the solution at a new time-level will be

$$u_j^{n+1} = u_j^n - C\left(u_j^n - u_{j-1}^n\right) + \mathcal{O}\left(\Delta t^2, \Delta x \Delta t\right) \quad \text{for} \quad \lambda > 0, \tag{3.4.19}$$

$$u_j^{n+1} = u_j^n - C\left(u_{j+1}^n - u_j^n\right) + \mathcal{O}\left(\Delta t^2, \Delta x \Delta t\right) \quad \text{for} \quad \lambda < 0, \tag{3.4.20}$$

where $C \equiv \lambda \frac{\Delta t}{\Delta x}$ is the Courant factor. We will briefly see other examples of finite-difference scheme.

The Lax-Friedrichs scheme was proposed as a modification of the FTCS (Forward-Time-Centered-Space) scheme, which is proven to be unstable. The idea is to replace in the FTSC algorithm u_j^n with its spatial average, i.e. $u_j^n \to u_j^n = \left(u_{j+1}^n + u_{j-1}^n\right)/2 + \mathcal{O}\left(\Delta x^2\right)$, finding

$$u_j^{n+1} = \frac{1}{2}\left(u_{j+1}^n + u_{j-1}^n\right) - \frac{C}{2}\left(u_{j+1}^n - u_{j-1}^n\right) + \mathcal{O}\left(\Delta x^2\right). \tag{3.4.21}$$

This makes the Lax-Friedrichs a stable first-order scheme.

The leapfrog scheme is a stable second-order scheme. With a similar approach to the advection equation, but employing a higher-order discretization of the time derivative, i.e.

$$\partial_t u|_j^n = \frac{u_j^{n+1} - u_j^{n-1}}{2\Delta t} + \mathcal{O}\left(\Delta t^2\right), \tag{3.4.22}$$

we find the algorithm

$$u_j^{n+1} = u_j^{n-1} - C\left(u_{j+1}^n - u_{j-1}^n\right)\mathcal{O}\left(\Delta x^2\right). \tag{3.4.23}$$

An interesting second-order scheme is the Lax-Wendroff scheme. This is a two-level scheme obtained from a combination of the Lax-Friedrichs and the leapfrog schemes. For the advection equation the first step is

$$u_{j\pm\frac{1}{2}}^{n+\frac{1}{2}} = \frac{1}{2}\left(u_j^n + u_{j\pm1}^n\right) \mp \frac{C}{2}\left(u_{j\pm1}^n - u_j^n\right) + \mathcal{O}\left(\Delta x^2\right), \tag{3.4.24}$$

which is a Lax-Friedrichs "half step" at a fictitious intermediate position $j \pm 1/2$ and time-level $n + 1/2$. The second step is given by

$$u_j^{n+1} = u_j^n - C\left(u_{j+\frac{1}{2}}^{n+\frac{1}{2}} - u_{j-\frac{1}{2}}^{n+\frac{1}{2}}\right) + \mathcal{O}\left(\Delta x^2\right), \tag{3.4.25}$$

which is a leapfrog "half step". This scheme can be cast as a one-level scheme as

$$u_j^{n+1} = u_j^n - \frac{C}{2}\left(u_{j+1}^n - u_{j-1}^n\right) + \frac{C^2}{2}\left(u_{j+1}^n - 2u_j^n + u_{j-1}^n\right) + \mathcal{O}\left(\Delta x^2\right), \tag{3.4.26}$$

where only quantities at real time-levels and spatial positions appear.

3.4.2 High-resolution shock capturing methods

An important class of methods is represented by the Godunov methods. In the original approach, formulated by Godunov in 1959 to manage discontinuities [59], one approximate continuous solutions with a piecewise constant function, creating a series of Riemann problems, which consist of determining the proper state value of a variable at a discontinuous interface. For a linear system Godunov's method reduces to the upwind scheme, yielding a simple solution to the Riemann problems. For a nonlinear set of equations instead, accurate Riemann solvers are needed. The main problem with Godunov's method is that, due to the piecewise constant function, it is only first-order accurate. Modern Godunov methods combine sophisticated strategies for the computation of the left and right states of the local Riemann problems with approximate solutions of such Riemann problems. The resulting methods are now widely adopted and are known as high-resolution shock capturing (HRSC) methods. Three common blocks are behind every HRSC method based on Godunov methods:

- reconstruction of the left and right state of a local Riemann problem at each cell boundary;
- use of an approximate Riemann solver;
- use of a time-update algorithm of at least second-order accuracy.

The reconstruction method employed in our simulations is a piecewise-parabolic method. This method adopts a parabolic interpolation of the variables inside the cells. We start considering the initial averaged values of the general quantity U between $x_{j-1/2}$ and $x_{j+1/2}$ over a uniform spatial grid

$$U_j^n = \frac{1}{\Delta x}\int_{x_{j-1/2}}^{x_{j+1/2}} U\left(x, t^n\right) dx, \tag{3.4.27}$$

where $\Delta x = x_{j+1/2} - x_{j-1/2}$. We then build an interpolating parabola inside each cell with equation

$$\Phi(\xi) = a\xi^2 + b\xi + c, \tag{3.4.28}$$

with $\xi = \left(x - x_{j-1/2}\right)/\Delta x$, $x \in \left[x_{j-1/2}, x_{j+1/2}\right]$, and a, b and c constants to be determined. The interpolation must be conservative, so

$$U_j^n = \int_0^1 \Phi(\xi)\, d\xi. \tag{3.4.29}$$

Another constraint is that no new extrema appear in the parabola which did not already appear in U_j^n. So together with the condition 3.4.29 we can choose the values U_j^- and U_j^+ of the interpolating parabola at the left and right edges of the j-th numerical cell. They are found by imposing that (i) they do not fall outside the range of two adjacent values U_j^n and U_{j+1}^n, (ii) in smooth parts $U_{j+1}^- = U_j^+ = U_{j+1/2}^n$, so the interpolating function is continuous at $x_{j+1/2}$, (iii) the interpolating parabola is monotone in each cell.

The second step involves the use of an approximate Riemann solver. We adopt approximate solvers as exact Riemann solvers requires very high computational resources thus making its application in present multidimensional codes unrealistic. Approximate solvers can be divided into complete and incomplete; complete solvers contain all the characteristic fields of the exact solution, while incomplete solvers contain only a subset of them. Our simulations employs the HLLE solver [60, 61], which is a widely used approximate incomplete Riemann solver. The solver is based on the assumption that after the decay of the initial discontinuity of the local Riemann problem only two waves propagate in two opposite directions, with velocities λ_{L} and λ_{R}, generating a single and constant state between them as

$$\mathcal{U}(x,t) = \begin{cases} \mathcal{U}_{\mathrm{L}} & \text{if} \quad x/t < \lambda_{\mathrm{L}} \\ \mathcal{U}^{\mathrm{HLLE}} & \text{if} \quad \lambda_{\mathrm{L}} < x/t < \lambda_{\mathrm{R}} \\ \mathcal{U}_{\mathrm{R}} & \text{if} \quad x/t > \lambda_{\mathrm{R}} \end{cases}. \tag{3.4.30}$$

If we consider the conservation equation $\partial_t \mathcal{U} + \nabla \mathcal{F}(\mathcal{U}) = 0$, with $\mathcal{F}_{\mathrm{L}} = \mathcal{F}(\mathcal{U}_{\mathrm{L}})$ and $\mathcal{F}_{\mathrm{R}} = \mathcal{F}(\mathcal{U}_{\mathrm{R}})$, it can be found that

$$\mathcal{U}^{\mathrm{HLLE}} = \frac{\lambda_{\mathrm{R}}\mathcal{U}_{\mathrm{R}} - \lambda_{\mathrm{L}}\mathcal{U}_{\mathrm{L}} + \mathcal{F}_{\mathrm{L}} - \mathcal{F}_{\mathrm{R}}}{\lambda_{\mathrm{R}} - \lambda_{\mathrm{L}}}, \tag{3.4.31}$$

$$\mathcal{F}^{\mathrm{HLLE}} = \frac{\lambda_{\mathrm{R}}\mathcal{F}_{\mathrm{R}} - \lambda_{\mathrm{L}}\mathcal{F}_{\mathrm{L}} + \lambda_{\mathrm{R}}\lambda_{\mathrm{L}}(\mathcal{U}_{\mathrm{R}} - \mathcal{U}_{\mathrm{L}})}{\lambda_{\mathrm{R}} - \lambda_{\mathrm{L}}}, \tag{3.4.32}$$

where $\mathcal{F}^{\mathrm{HLLE}}$ is the HLLE flux to be used in the Godunov method according to

$$\mathcal{F}^{\mathrm{HLLE}} = \begin{cases} \mathcal{F}_{\mathrm{L}} & \text{if} \quad x/t < \lambda_{\mathrm{L}} \\ \mathcal{F}^{\mathrm{HLLE}} & \text{if} \quad \lambda_{\mathrm{L}} < x/t < \lambda_{\mathrm{R}} \\ \mathcal{F}_{\mathrm{R}} & \text{if} \quad x/t > \lambda_{\mathrm{R}} \end{cases}. \tag{3.4.33}$$

This solver is effective for its simplicity, and performs well at critical sonic rarefactions, but produces excessive smearing at contact with discontinuities as the middle waves are ignored in the solution. It also needs to be coupled with an algorithm for the calculation of the wave speeds.

The last step regards the time evolution of the system. The most widely adopted methods for time-update are the Runge-Kutta methods. Let's consider an equation in the form $\partial_t U = -\partial_x F(U) + S(U) = Q(U)$. Integrating in space we obtain

$$\frac{d}{dt}U_j(t) = \frac{1}{\Delta x}\left(F\left[U\left(x_{j-1/2},t\right)\right] - F\left[U\left(x_{j+1/2},t\right)\right]\right) + S_j \equiv L(U_j) + S_j, \quad (3.4.34)$$

where U_j and S_j are the spatial averages of the solution and of the source term, given by

$$U_j = \frac{1}{\Delta x}\int_{x_{j-1/2}}^{x_{j+1/2}} U(x,t)\,dx, \qquad S_j = \frac{1}{\Delta x}\int_{x_{j-1/2}}^{x_{j+1/2}} S(x,t)\,dx. \quad (3.4.35)$$

At first-order Equation 3.4.34 can be integrated as (we will drop the j index)

$$U^{n+1} = U^n + \Delta t Q(U^n). \quad (3.4.36)$$

The i-th substep is

$$U^{(i)} = \sum_{k=0}^{i-1}\left(\alpha_{ik}U^{(k)} + \Delta t\beta_{ik}Q\left(U^{(k)}\right)\right), \qquad i = 1,\ldots,n+1, \quad (3.4.37)$$

$$U^{(0)} = U^n, \quad (3.4.38)$$

with α_{ik} and β_{ik} constant coefficients. The second-order Runge-Kutta (RK2) is given by

$$U^{(1)} = U^n + \Delta t Q(U^n), \quad (3.4.39)$$

$$U^{n+1} = \frac{1}{2}\left[U^n + U^{(1)} + \Delta t Q\left(U^{(1)}\right)\right], \quad (3.4.40)$$

while the third-order update (RK3) is

$$U^{(1)} = U^n + \Delta t Q(U^n), \quad (3.4.41)$$

$$U^{(2)} = \frac{1}{4}\left[3U^n + U^{(1)} + \Delta t Q\left(U^{(1)}\right)\right], \quad (3.4.42)$$

$$U^{n+1} = \frac{1}{3}U^n + \frac{2}{3}U^{(2)} + \frac{2}{3}\Delta t Q\left(U^{(2)}\right). \quad (3.4.43)$$

4 Initial conditions and models

As mentioned in the previous chapter, in order to start a simulation we need to establish the initial conditions of the system, i.e. we have to build a physically consistent representation of the BNS at the starting point of the evolution we want to follow. This translates into giving the positions, masses, gravitational fields, velocities etc. of the two NSs at a given initial separation, which will then be evolved in time. In this chapter we focus on this aspect, discussing the NS EOS employed in our models, the tools to generate the initial conditions, and the specific choices made for the simulations we performed.

4.1 The equation of state

The EOS is a fundamental ingredient to build models of NSs, yet affected by big uncertainties. Since the extreme conditions in the inner regions of a NS cannot be reproduced on Earth, the EOS is essentially unknown. In turn, NSs are excellent laboratories for studying the behaviour of matter at such high densities, allowing us to test different theoretical EOS against the observational data (e.g. see Figure 4.1).

An EOS can be parametrized specifying the stiffness of the star at different density intervals measured by the adiabatic index $\Gamma = d\log p/d\log\rho$, where p is the pressure and ρ the density of the star. When Γ is taken as a constant the EOS is called polytrope, while the parametrized EOS becomes piecewise-polytropic when assuming different Γ values in different density intervals, i.e.

$$p = K_i\,\rho_i^{\Gamma_i} \qquad \text{for} \quad \rho_i \leq \rho \leq \rho_{i+1}, \tag{4.1.1}$$

where the pressure is still determined for every density (continuity is required between two adjacent intervals). A wide collection of EOS candidates exist, mainly obtained from relativistic mean field theory (RMFT) and non-relativistic many body theory (NMBT) with relativistic corrections. In RMFT the strong interaction is modelled as mesons exchange between nucleons. In NMBT an effective hamiltonian for the two- and three-body interaction is employed. The free parameters in these effective models are defined by low-energy experiments and extrapolated to higher nuclear densities. Regarding the particle content, we can distinguish two classes of EOSs, the first including only plain nuclear matter (n, p, e, μ), while the second including hyperons, pion and kaon condensates, or quarks. In our simulations we adopt a piecewise-polytropic parametrization of the APR4 EOS [62], which includes only plain nuclear matter. The parameters defining each layer are listed in Table 4.1.

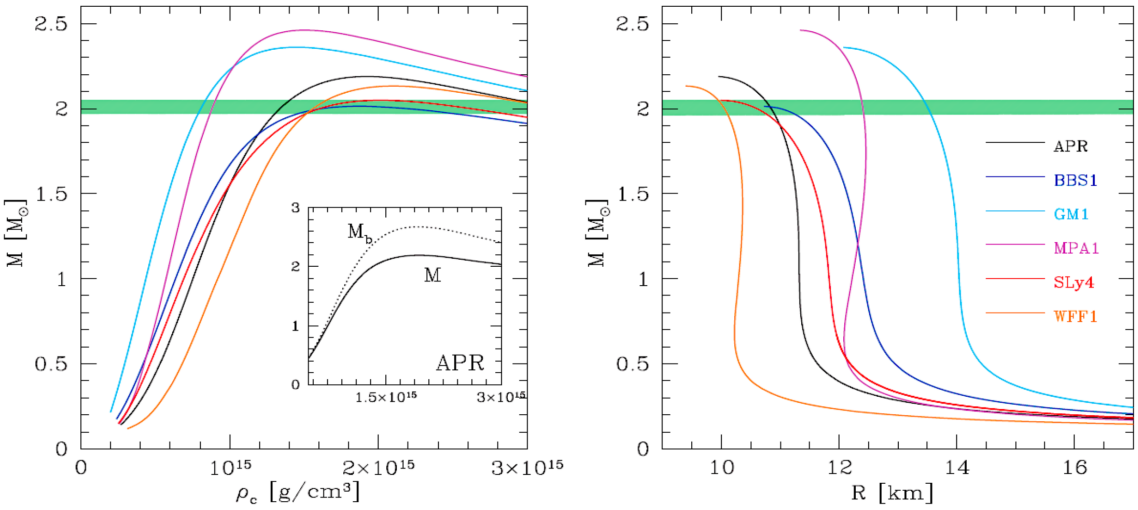

Figure 4.1: Mass in function of central density (left) and radius (right) for different EOSs. The green strip sets the range for the largest NS mass reported. In the left panel inset we see the difference between the baryonic mass and the gravitational mass for the APR EOS, the latter being smaller as it accounts for the gravitational binding energy.

The values from $i = 0$ to $i = 6$ are taken from [63]. The causality condition in the APR4 EOS holds up to $\rho_c = 1.45 \times 10^{15}\,\mathrm{g/cm^3}$, above which the sound speed becomes superluminal. The segments $i = 7, 8$ have been introduced by [12] to preserve causality even above ρ_c. The resulting modified EOS is fully causal but it may not be completely realistic in the very high density regime. In Figure 4.2 we can see the pressure (given by Equation 4.1.1) as function of the rest mass density for the APR4 EOS and other popular EOSs. The pressure profile shows important differences in the high-density parts (i.e. in the NS core) as shown in the inset of the figure. In order to include thermal effects (e.g., shock heating), an additional component is added via an ideal-fluid EOS with adiabatic index $\Gamma_{\mathrm{th}} = 1.8$, which gives the final EOS

$$p\left(\rho, \epsilon\right) = p_{\mathrm{cold}}\left(\rho\right) + \left(\Gamma_{\mathrm{th}} - 1\right)\left(\epsilon - \epsilon_{\mathrm{cold}}\left(\rho\right)\right)\rho, \tag{4.1.2}$$

where ϵ is the specific internal energy.

i	ρ_i	K_i	Γ_i
0	-	6.801×10^{-09}	1.584
1	2.440×10^{7}	1.062×10^{-06}	1.287
2	3.784×10^{11}	$5.327 \times 10^{+01}$	0.622
3	2.628×10^{12}	3.999×10^{-08}	1.357
4	1.513×10^{14}	5.174×10^{-29}	2.830
5	5.012×10^{14}	4.713×10^{-38}	3.445
6	1.000×10^{15}	1.344×10^{-36}	3.347
7	1.400×10^{15}	2.507×10^{-31}	3.000
8	1.610×10^{15}	4.036×10^{-16}	2.000

Table 4.1: Parameters for the piecewise-polytropic parametrization of the APR4 EOS. Γ_i is dimensionless, ρ_i is in g/cm^3, K is in cgs units such that p results in dyne/cm^2.

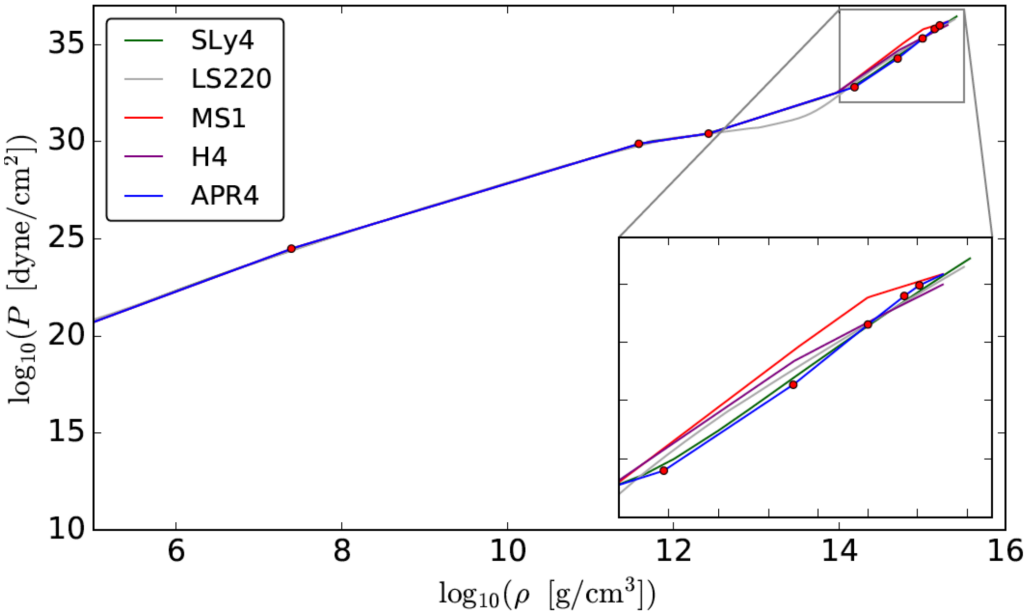

Figure 4.2: Pressure in function of rest mass density for the APR4 EOS compared with other EOS. [12]

4.2 The LORENE code

The initial configuration of the BNS is computed by means of the publicly available code LORENE (*Langage Objet pour la RElativité NumériquE*). The code consists of a set of C++ classes to solve various problems in numerical relativity, providing tools to solve the related partial differential equations.

We considered a fixed chirp mass of value $\mathcal{M} = 1.186\,M_\odot$, according to GW170817. The chirp mass can be written in terms of the masses of the two objects and the mass ratio $q = m_1/m_2$ as

$$\mathcal{M} = \left[\frac{q}{(q+1)^2}\right]^{3/5} (m_1 + m_2)\,. \tag{4.2.1}$$

In our simulations we investigated the equal mass case, i.e. $q = 1.0$, and the case $q = 0.9$. From 4.2.1 we can then calculate the mass of the two companions, obtaining two NSs with mass $m_{\rm NS} = 1.36\,M_\odot$ for $q = 1.0$ and $m_1 = 1.44\,M_\odot$, $m_2 = 1.29\,M_\odot$ for $q = 0.9$. The "Rot_star" code (which stands for *rotating star*) in the LORENE library let us build a single NS with the required parameters. In particular, we tune the central enthalpy input value in order to obtain a gravitational mass equal to the ones calculated above. As in our simulations we want to consider irrotational NSs, we set the angular frequency to zero. The APR4 EOS is set by giving the parameters for each polytropic segment, as shown in Table 4.1. The output parameters computed by the code include the baryonic mass, which is equal to the gravitational mass plus the absolute value of the gravitational binding energy, the mean and circumferential radius ($R_{\rm m}$ and $R_{\rm c}$), the compactness parameter ($m_{\rm NS}/R_{\rm c}$), the moment of inertia, the surface area and more.

To build a binary system LORENE includes the code "Bin_star" (*binary star*). As input we give the initial conditions of the binary, in particular the calculated baryonic masses (calculated via Rot_star) and the required coordinate separation distance, which we set to 45 km. The configuration given as output is then evolved by the Einstein Toolkit and WhiskyMHD codes.

4.3 Magnetic field implementation

The LORENE code cannot compute equilibrium configurations for a magnetized system. The magnetic field has to be added manually to the initial configuration of the BNS. Since the magnetic field structure in NSs is not well-known, we adopt an analytical prescription for the vector potential, i.e.

$$A_\phi = \bar{\omega}^2 A_b \max\left(p - p_{\rm cut}, 0\right)^{n_s}\,, \tag{4.3.1}$$

where $\bar{\omega}$ is the coordinate distance from the NS spin axis, A_b is a constant, $\max(p)$ is the maximum pressure in the NS, $p_{\rm cut} = 0.04 \max(p)$ determines the cut-off where the magnetic field becomes zero inside the NS, and $n_s = 2$ sets the degree of differentiability of the magnetic field strength. This prescription generates a dipole-like field confined inside the NSs while the field value remains zero on the outside. The constant A_b is set to ~ 1191 such that the corresponding initial maximum magnetic field strength is 5×10^{15} G. The magnetic field acts as a small perturbation even at such high values, and the impact on the NS structure can be neglected at first approximation. The resulting initial magnetic field strength is $10^2 - 10^4$ times higher than the actual values in NSs binaries. High resolution GRMHD simulations of BNS mergers confirmed that magnetic field amplification mechanisms such as Kelvin-Helmholtz instability, if well-resolved, can produce magnetic strength of order 10^{15} G and higher. Since our simulations are run in a low-resolution mode we cannot resolve these instabilities, thus resulting in lower magnetic field amplification. The choice of such high values for the initial magnetic field strength is intended to partially compensate for this lack of resolution, allowing us to explore more realistic post merger magnetic fields. We point out that this approach is by no means equivalent to evolving lower and more realistic initial field strengths with the appropriate resolution (which is computationally prohibitive given the current capabilities of the available HPC clusters).

4.4 Final setup and evolution codes

The initial conditions, as we discussed above, are generated with the LORENE code and evolved with the Einstein Toolkit and WhiskyMHD codes. The Einstein Toolkit is a framework devoted to solving the Einstein's equations in the BSSNOK formalism (see Chapter 3). A "moving box" mesh refinement is implemented via the Carpet driver, employing six refinement levels. During the inspiral phase, the two finest levels follow the NSs. During the merger, it switches to a fixed-mesh refinement centred at the merger site. The grid spacing in the finest refinement is $dx = dy = dz = 255$ m. In order to save computational resources we assume a reflection symmetry across the $z = 0$ plane.

WhiskyMHD is used to solve the GRMHD equations, i.e. to inform the right-hand side of Einstein equations. The GRMHD equations are written in a flux conservative form, following the so-called Valencia formulation, already discussed in Section 3.3. Moreover, WhiskyMHD implements high-resolution shock-capturing schemes (see 3.4.2).

5 Results

Our simulations extend up to 60 ms after the merger, making them the longest simulations ever done in GRMHD for BNS mergers ending up in a long-lived except for one simulation of 100 ms recently published by Ciolfi et al [64]. Exploring the evolution of these systems several tens of milliseconds after the merger allowed us to reveal effects that one could not see with shorter simulations.

5.1 General dynamics

We start by looking at the general dynamics. Figures 5.1 and 5.2 show the rest-mass density in the meridional and equatorial plane for the q_{10} and q_{09} models respectively. The ejected material, i.e. the thrown away material that has sufficient velocity to leave the system, is highlighted by the contours. To determine which material is effectively unbound we adopt the geodesic criterion (see e.g. [65]). We consider as unbound each point that has $|u_t| > 1$, where u^t is the t-component of the four-velocity. We can immediately distinguish the q_{10} model from the q_{09} in the first frame at 1 ms before the merger. The q_{10} model in fact exhibits a symmetric distribution of the tidal ejecta, as the system is completely symmetric. The q_{09} model instead shows an asymmetric distribution, with the bigger tidal tail corresponding to the lighter NS. This is due to the fact that in the q_{09} case the lighter NS is in part tidally disrupted by the companion, i.e. it partially "spreads" on the heavier one. In the q_{10} case on the contrary the two stars experience a symmetric collision. The differences between the two models are even more evident in the second frame, at 1 ms after the merger. Here we see the shock-wave ejecta that assume a more symmetric distribution in the q_{10} case, while in the q_{09} case they are expelled by asymmetric shock-waves. The third box is a snapshot at 60 ms after the merger. Here the differences in the rest-mass density distribution is almost gone, and the remnant stabilizes in a nearly axisymmetric state.

Figure 5.3 shows the time evolution of the rest-mass density distribution with respect to the distance from the centre of the grid. The red line indicates the average radius of the matter distribution. The two models present a similar behaviour, with the q_{09} case showing a slightly more expanded lower density outer layers after merger.

Figure 5.4 shows instead the maximum rest-mass density evolution for the two models. A significant jump is observed at merger, showing how the central density of the remnant object is in general higher than that of the two progenitor NSs. The oscillations triggered at merger indicate radial oscillations of the newly-formed remnant NS.

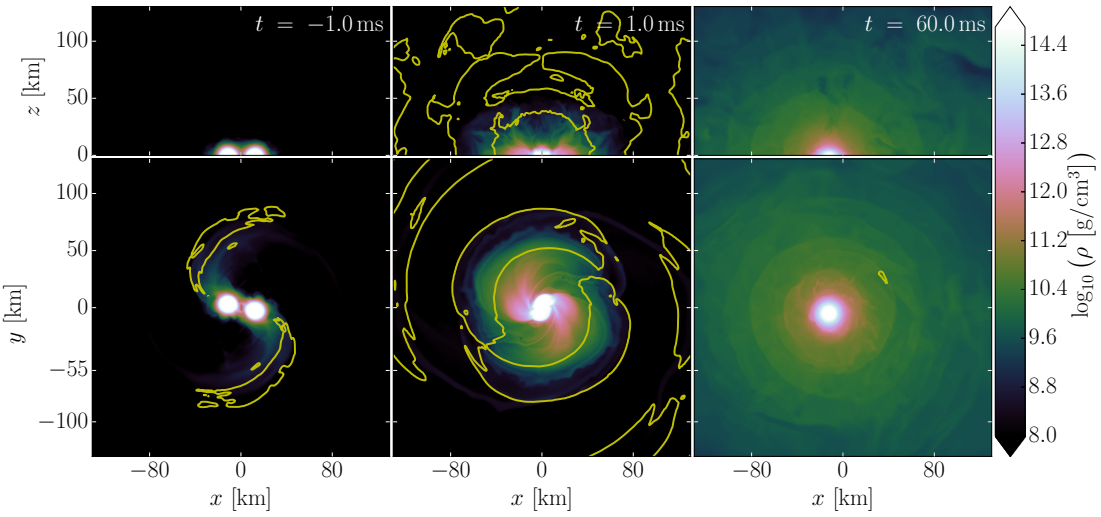

Figure 5.1: Rest-mass density evolution snapshots in the meridional (top panels) and equatorial (bottom panels) planes for model q_{10}, before, during and after the merger. The contours highlight unbound matter. Here $t = 0$ corresponds to the time of merger.

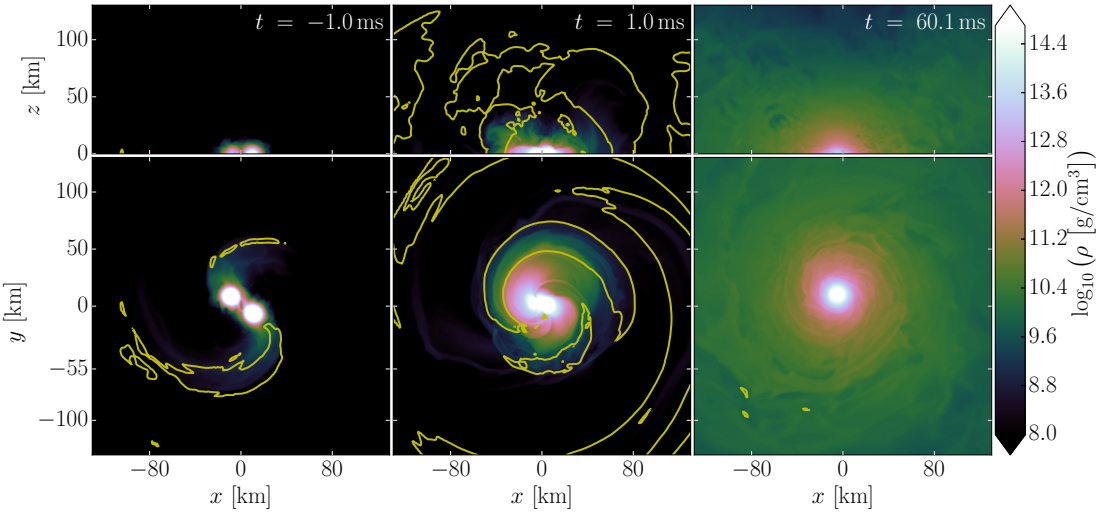

Figure 5.2: Rest-mass density evolution snapshots in the meridional (top panels) and equatorial (bottom panels) planes for model q_{09}, before, during and after the merger. The contours highlight unbound matter. Here $t = 0$ corresponds to the time of merger.

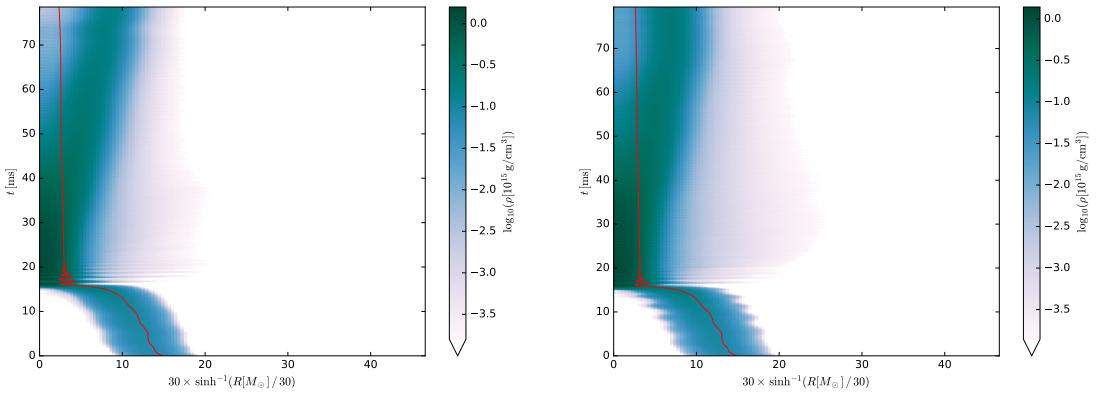

(a) q_{10} **(b)** q_{09}

Figure 5.3: Time vs. radius diagram of the baryon mass density (angle-averaged on spherical shells). Radial distance is represented using the function $\sinh^{-1}$ to show both small and large scales. The red line marks the average radius of the matter distribution.

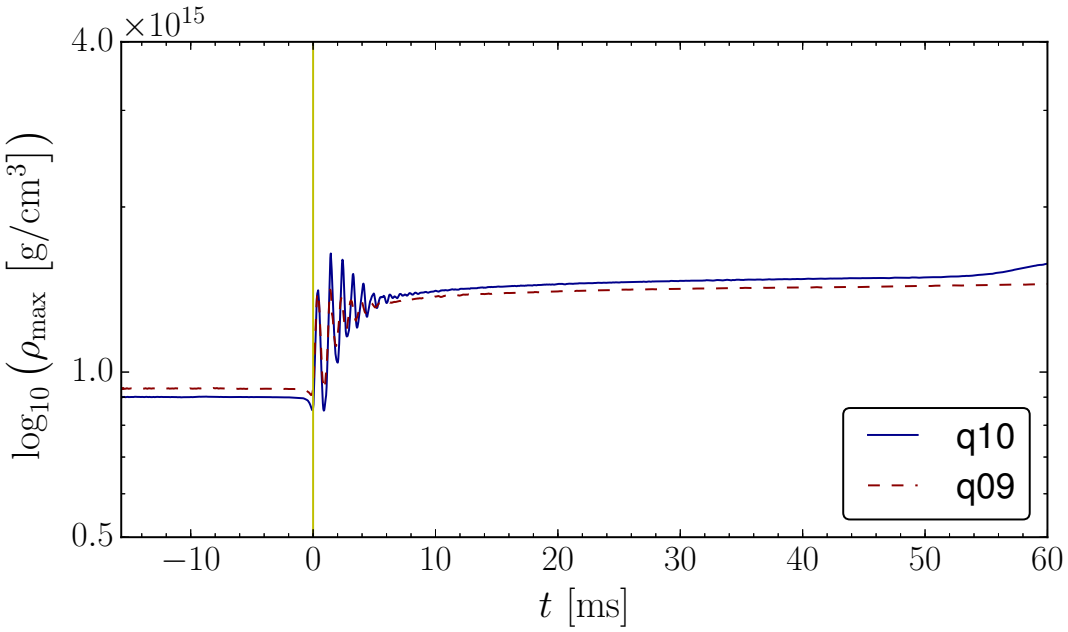

Figure 5.4: Time evolution of maximum rest mass density. The vertical line indicates the merger time.

5.2 Magnetic field evolution

We now turn to discuss the magnetic field evolution. During our discussion we should keep in mind that in the ideal MHD limit (i.e. infinite conductivity), in which we are working, the magnetic field lines are "frozen" inside the fluid, in other words they can be thought as "painted" on the fluid itself. This peculiar property of ideal MHD gives rise to interesting effects in the magnetic field evolution that we will discuss, as a motion of a fluid element will the magnetic field with it.

We start by looking at Figure 5.5, that shows the magnetic energy and the maximum magnetic field strength respectively, for both q_{10} and q_{09} models. The pre-merger amplification that is present also in other simulations (e.g. [64]) is still under debate. In fact the physical mechanism responsible for such amplification is still unclear, and we cannot exclude possible non physical effects due to the numerical setup or the initial data. A possible physical explanation, on the other hand, could be that the amplification is due to fluid motions (and consequent magnetic field rearrangement) inside the NSs caused by the tidal deformation to which they are subject in the pre-merger phase, at distances small enough the tidal effects of the gravitational field are not negligible.

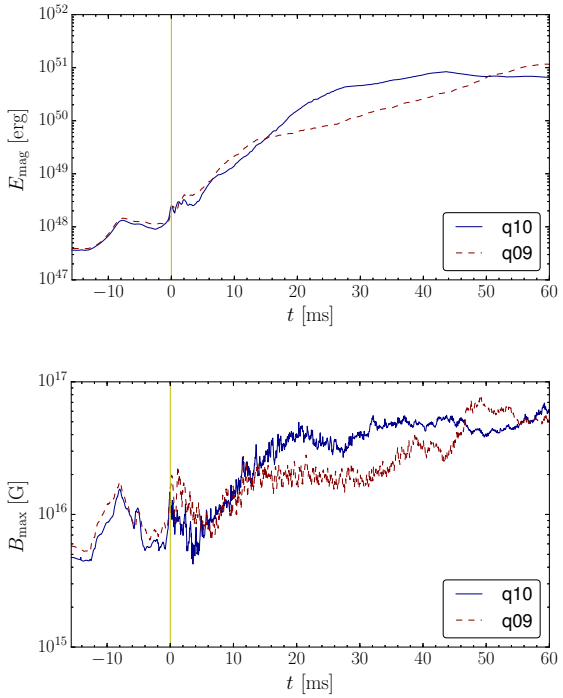

Figure 5.5: Time evolution of the magnetic energy (top) and of the maximum magnetic field strength (bottom). The vertical line indicates the merger time.

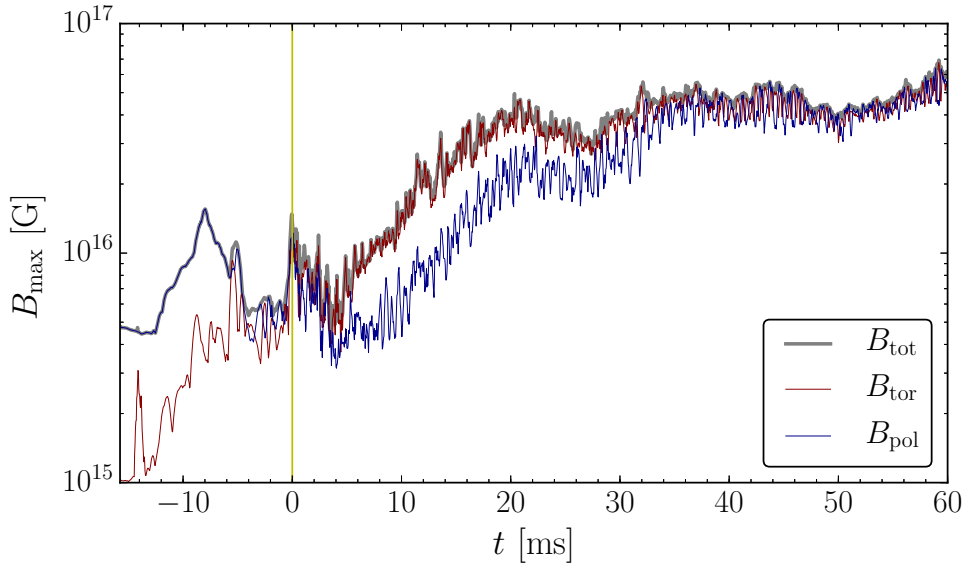

Figure 5.6: Time evolution of the maximum magnetic field strength, with toroidal and poloidal components, for model q_{10}. The vertical line indicates the merger time.

The early post-merger amplification is dominated by the Kelvin-Helmholtz instability (KHI), that is active for about 10 ms after the merger. The KHI is a purely hydrodynamic effect that can appear at the interface between two fluids with opposite velocities. This mechanism produces twist-like structures at the interface, that in our case will correspond to creating the same structures in the magnetic field lines. This will result in an amplification of the magnetic field, and we expect in particular an amplification in the toroidal component. In fact Figure 5.6 shows that the amplification in this phase involves mostly the toroidal component of the magnetic field. This mechanism is not well resolved in modern simulations, and we would expect a higher amplification in comparison to the one we get. For this reason we need to start with higher than typical magnetic fields for the single NSs to reach the expected level of post-merger magnetization (that have been studied in other simulations with higher resolution [66]).

After the two stars have merged into a single object the KHI gradually becomes less relevant. The dominating effect in the magnetic field amplification is then the magnetorotational instability (MRI). This mechanism relies on a particular property of the magnetic field in the ideal MHD limit, briefly, that the force between two fluid elements has a spring-like nature. It requires differential rotation with decreasing angular velocity with increasing radial distance, which excludes, as we will see, the

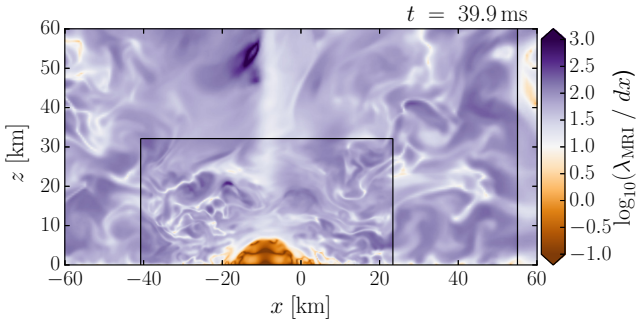

(a) q_{10}

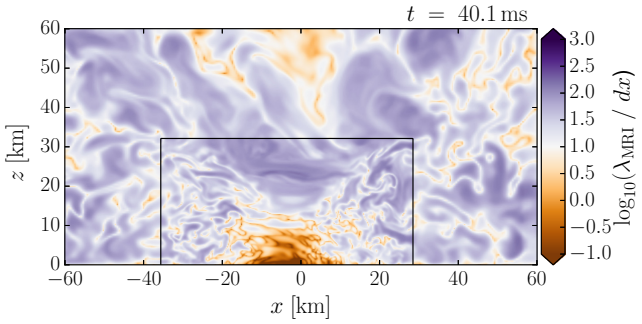

(b) q_{09}

Figure 5.7: Number of grid points covering the characteristic length of the magnetorotational instability, λ_{MRI}. Inner black contour marks the extension of the finest refinement boundary.

central core of the remnant NS. The MRI is well resolved if the wavelength of its fastest growing mode $\lambda_{\mathrm{MRI}} \approx \frac{2\pi}{\Omega}\frac{B}{\sqrt{4\pi\rho}}$, where Ω is the angular velocity and B the magnetic field strength, is covered by at least 10 gridpoints. Figure 5.7 shows that this condition is fulfilled in almost all the domain (except for the central region, in which however the MRI does not take place) at $t = 40\,\mathrm{ms}$, so we can trust the evolution of the magnetic field at least from this point on. An interesting feature that was not revealed in previous simulations (as they were too short) is the saturation that wee see in the magnetic energy and the maximum magnetic field. Both models reach similar values of about $10^{51}\,\mathrm{erg}$. The fact that q_{10} reaches the plateau earlier can be due to the fact that the more symmetric configuration fasten up the rearrangement of the remnant.

Figures 5.9 and 5.10 confirm the evolution described above, showing that during and shortly after the merger we have a toroidal component that is emerging, while at

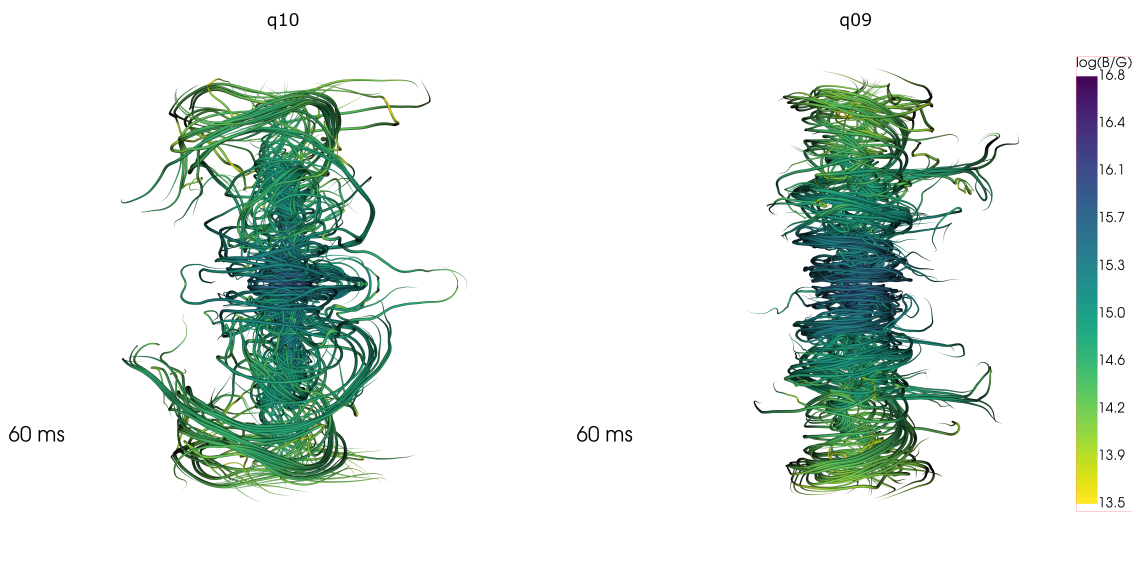

Figure 5.8: Magnetic field line structure in 3D for both models at 60 ms after the merger, with colour-coded field strength. The vertical extension of the frames covers about ±100 km along the z-axis.

later time the poloidal and toroidal components reach similar values. Moreover, as we can see better in Figure 5.8, the magnetic field strength is higher in the equatorial plane. In the right panels of Figures 5.9 and 5.10, in the equatorial plane, we see that the magnetic field strength in the central core of the remnant is ~ 2 orders of magnitude higher in the q_{09} case. This difference may be possibly attributed to the fact that the q_{09} model has a steeper rotational profile in the central region (see Figure 5.13), which is responsible for a stronger magnetic field amplification.

A closer look at Figure 5.8 reveals that an ordered structure is emerging in the field lines, even though the field is still largely incoherent. We will come back to this figure in the next section.

Figures 5.11 and 5.12 show the magnetic-to-fluid pressure ratio, i.e. the ratio between the magnetic pressure and the fluid pressure. The first frame, before the merger, shows that (as expected) the magnetic pressure is negligible. In the second frame the magnetic pressure is starting to dominate in the meridional plane, while in the equatorial plane it is still negligible. The third frame shows that after the merger the magnetic pressure becomes important in certain regions, especially in the meridional plane. In particular, this shows how the slow and continuous matter outflow around the remnant NS, a nearly isotropic post-merger baryon wind, is in fact magnetically-driven.

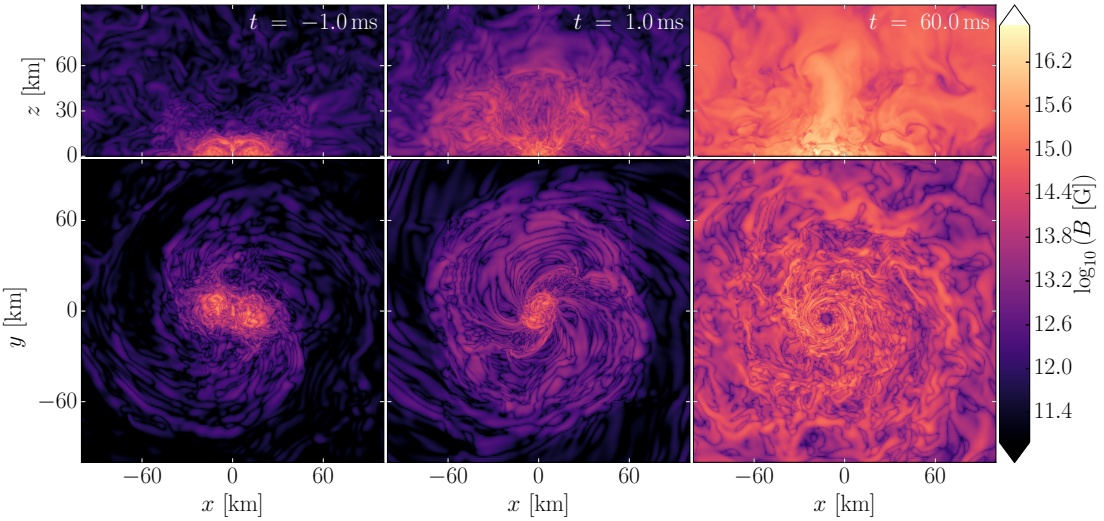

Figure 5.9: Magnetic field strength evolution snapshots in the meridional (top panels) and equatorial (bottom panels) planes for model q_{10}, before, during and after the merger. Here $t = 0$ corresponds to the time of merger.

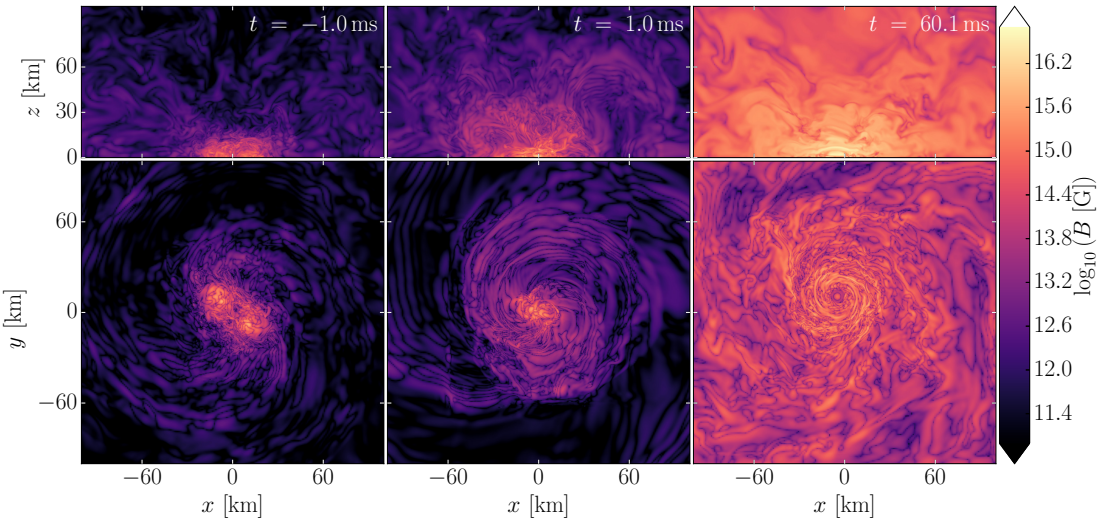

Figure 5.10: Magnetic field strength evolution snapshots in the meridional (top panels) and equatorial (bottom panels) planes for model q_{09}, before, during and after the merger. Here $t = 0$ corresponds to the time of merger.

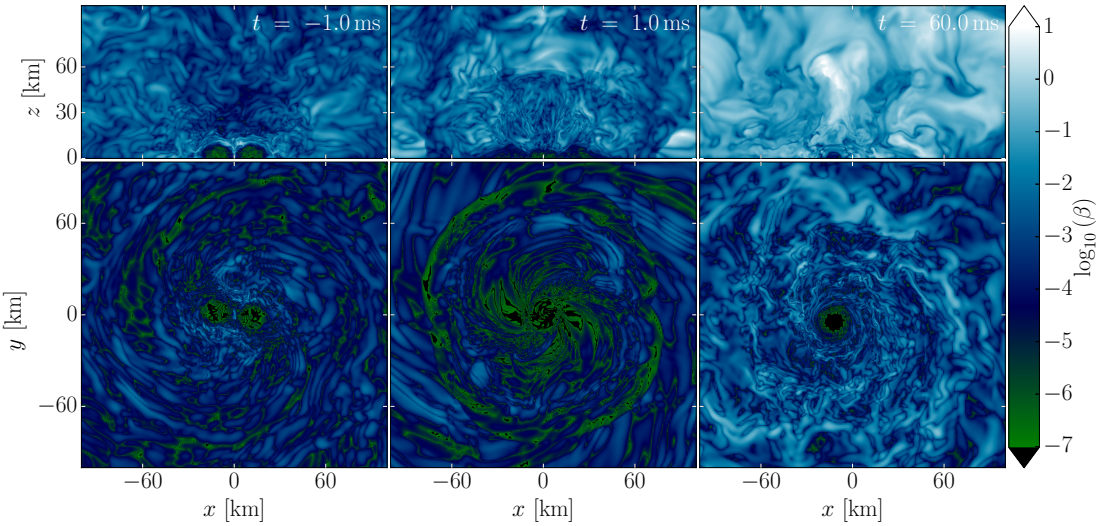

Figure 5.11: Magnetic-to-fluid pressure ratio β evolution snapshots in the meridional (top panels) and equatorial (bottom panels) planes for model q_{10}, before, during and after the merger. Here $t = 0$ corresponds to the time of merger.

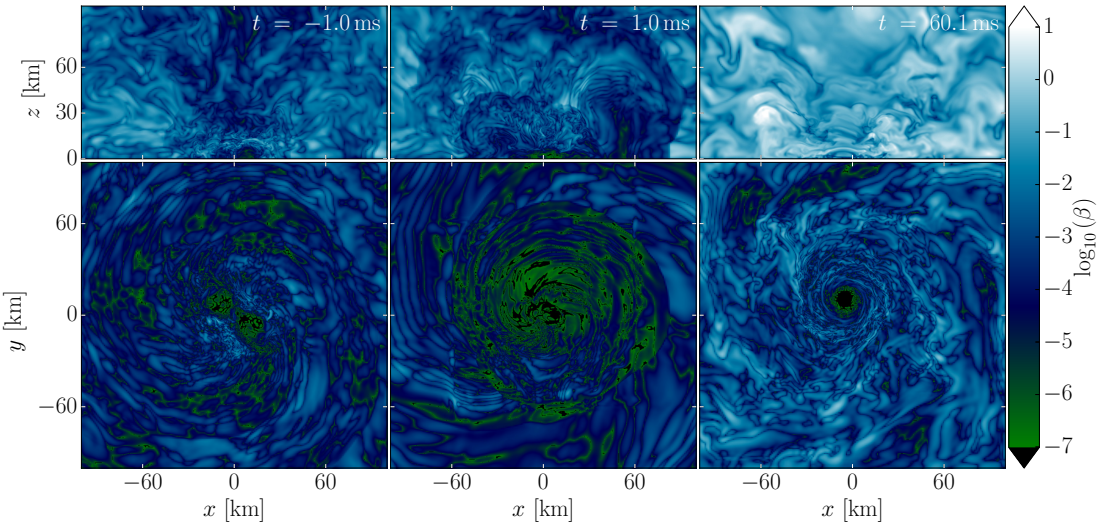

Figure 5.12: Magnetic-to-fluid pressure ratio β evolution snapshots in the meridional (top panels) and equatorial (bottom panels) planes for model q_{09}, before, during and after the merger. Here $t = 0$ corresponds to the time of merger.

5.3 Remnant structure and rotational profile

We now focus the attention on the remnant properties. Figure 5.13 shows the rotational profile of the remnant in the two cases. Both exhibit differential rotation in the core, while above about 10 km distance from the rotation axis we have a nearly keplerian profile, thus it is not "weighing" on the star but orbiting around it. As we anticipated before, the MRI requires decreasing angular velocities with increasing radius, so it does not take place for $r \lesssim 10\,\mathrm{km}$, that is also the region in which λ_{MRI} is not well resolved. In both models we expect the differential rotation to fade away and the core reaching uniform rotation in about 120 ms.

Figures 5.14 and 5.15 show the rest mass density in the meridional plane at 10 and 60 milliseconds after the merger, for q_{10} and q_{09} models respectively. The contours highlight selected iso-density surfaces. In the q_{09} plot, on the 60 ms frame, the central region appears less dense. This is a consequence of the motion acquired by the remnant after the merger, that in the q_{09} case was along the y-axis and thus the xz-plane does not cut anymore through the centre of the object. Anyway, both figures suggest that shortly after merger a torus-like structure is forming, but within few tens of milliseconds this structure disappears and the remnant with its surroundings acquires a more spherical shape. This behaviour is in agreement with [64], and overturns the common idea that a NS remnant would be surrounded by an accretion disk (see, e.g., [67]).

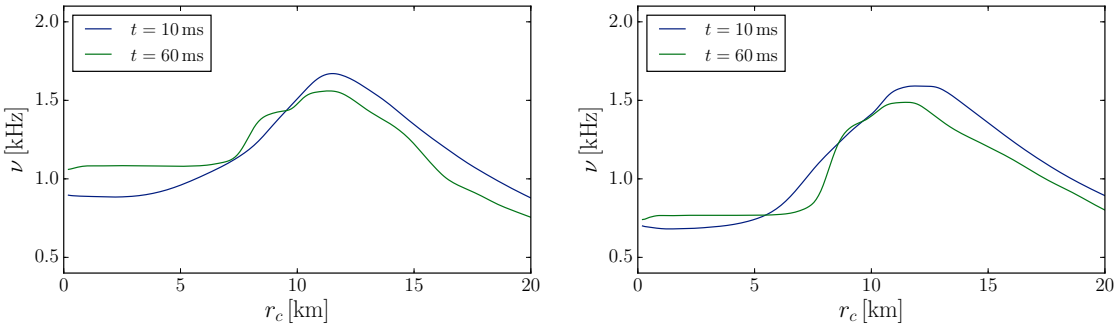

(a) q_{10} **(b)** q_{09}

Figure 5.13: Rotational profile on the equatorial plane at different times for model both models.

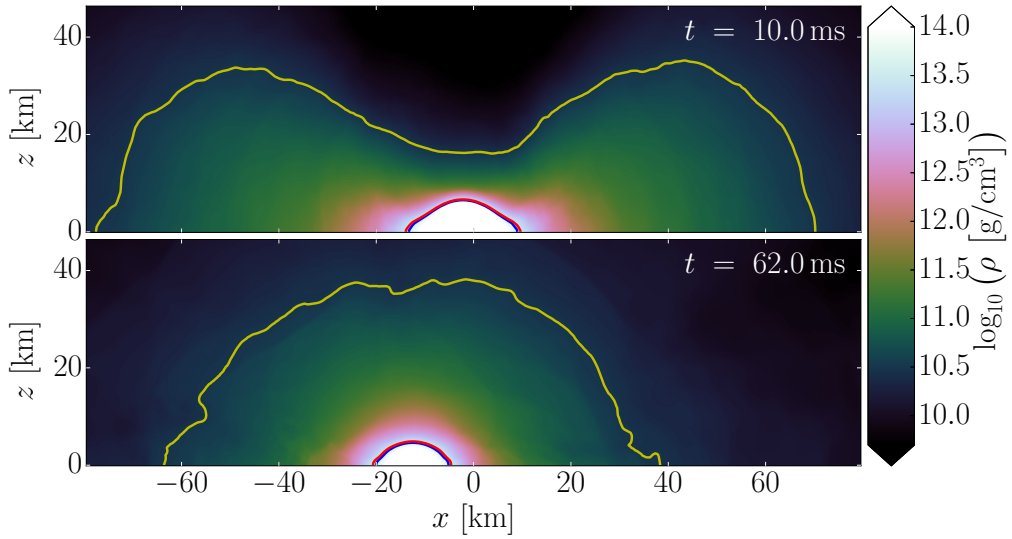

Figure 5.14: Remnant profile for model q_{10} at different times. The contours highlight iso-density surfaces, at $\rho = 3.0 \times 10^{10}$ (yellow), $\rho = 3.0 \times 10^{13}$ (red) and $\rho = 4.0 \times 10^{10}$ (blue).

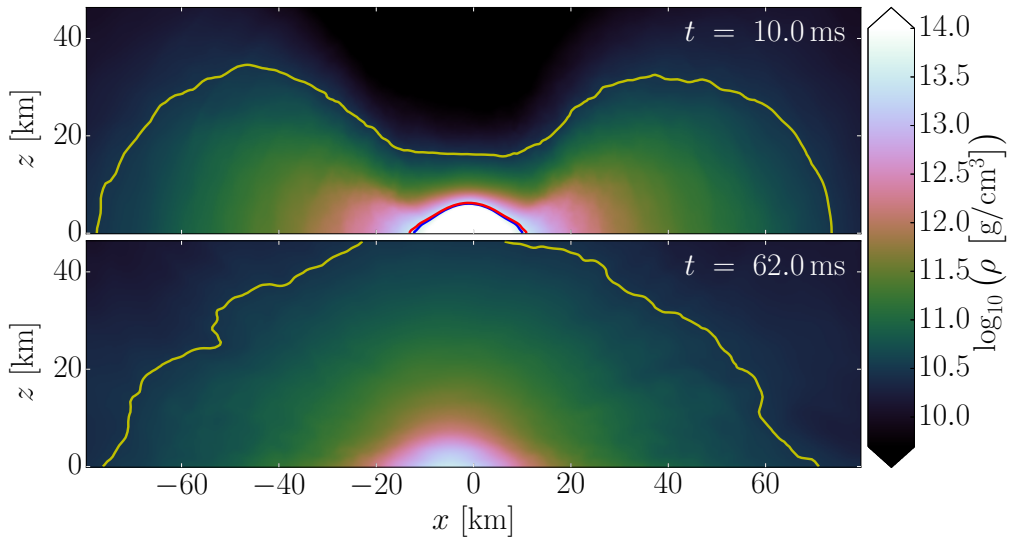

Figure 5.15: Remnant profile for model q_{09} at different times. The contours highlight iso-density surfaces, at $\rho = 3.0 \times 10^{10}$ (yellow), $\rho = 3.0 \times 10^{13}$ (red) and $\rho = 4.0 \times 10^{10}$ (blue).

5.4 Prospects of SGRB jet formation

One on the main purpose of our simulations was to determine whether or not a long-lived NS remnant generated in a merger event compatible with GW170817 is able to power a SGRB. From the magnetic energy evolution we saw that after the merger the energy saturates reaching magnitudes of 10^{51} erg. This suggests that in principle our systems have sufficient energy to power a relativistic jet. Considering the three-dimensional representation in Figure 5.8 of the magnetic field lines, however, we see that even if a sort of ordered structure is emerging, the typical helicoidal structure along the rotation axis that is needed to accelerate an outflow along the rotational axis is not present, as the field is still rather incoherent after 60 ms. The q_{09} model looks more ordered, so it could be that on longer timescales it will have better chances to launch a jet.

The density plot in the meridional plane for q_{10} as seen in Figure 5.17 shows that the environment is dense, with a baryon wind expanding from the merger site, and a tail left by dynamical ejecta during the merger process outside the wind. This slow wind represents a potential obstacle for the propagation of a jet, assuming that the latter could emerge at later times. At 60 ms after merger, we have anyway no signs that a jet is forming.

Figure 5.16 shows the velocity of the fluid for q_{10} , and this also excludes the formation of any jet-like structure. Furthermore, as the remnant is not surrounded by an accretion disk, as we saw in Figure 5.14 and Figure 5.15, we can exclude the possibility to launch a jet via accretion.

While there is still a possibility for a magnetically driven mechanism, up to now we have no evidence of SGRB formation, and we can conclude that the systems in these conditions cannot launch a jet.

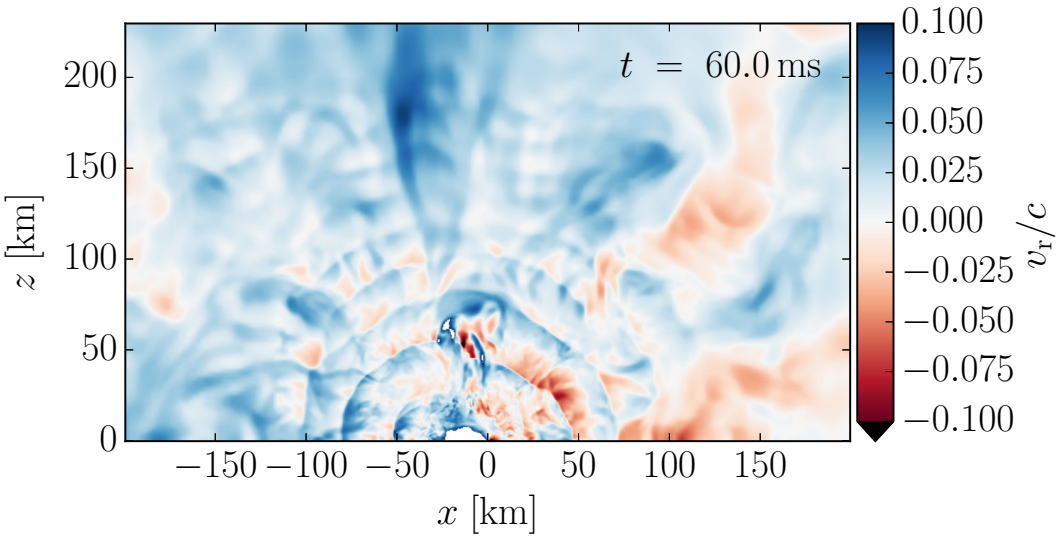

Figure 5.16: Radial velocity in the xz-plane for model q_{10}.

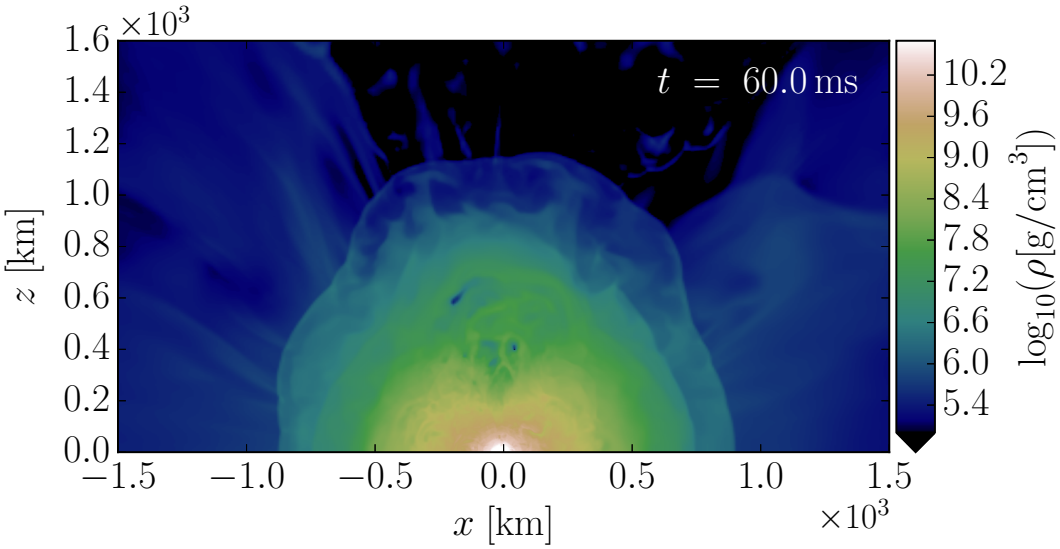

Figure 5.17: Rest-mass density distribution in the xz-plane for model q_{10}.

5.5 Gravitational waves

In this final section we discuss the gravitational wave signal. To extract the GW signal a widely used technique, that is implemented in our code, is based on the Newmann-Penrose scalars (see [68] for a detailed description of the different methods for the GW signal extraction). The quantity of our interest is calculated from the Weyl tensor

$$C_{\alpha\beta\mu\nu} = R_{\alpha\beta\mu\nu} - g_{\alpha[\mu}R_{\nu]\beta} + g_{\beta[\mu}R_{\nu]\alpha} + \frac{1}{3}g_{\alpha[\mu}g_{\nu]\beta}R, \tag{5.5.1}$$

contracting it appropriately with an orthonormal null tetrad l^μ, n^μ, m^μ, $\bar{m}^\mu$. The tetrad choice for the computation is described in [69]. For our purpose we are interested into the Weyl scalar ψ_4, which is defined by

$$\psi_4 = -C_{\alpha\beta\mu\nu}n^\alpha\bar{m}^\beta n^\mu\bar{m}^\nu, \tag{5.5.2}$$

that in the asymptotic limit describes the outgoing gravitational radiation. In particular, in the TT-gauge it holds that

$$\psi_4 = \ddot{h}_+ - \ddot{h}_\times. \tag{5.5.3}$$

It can be proven that the Weyl tensor can be written in terms of spatial quantities only (to be consistent with the 3+1 formalism), and it takes the form

$$\psi_4 = \left(R_{ij} - KK_{ij} + K_i{}^kK_{ij} - i\epsilon_i{}^{kl}\nabla_l K_{jk}\right)\bar{m}^i\bar{m}^j, \tag{5.5.4}$$

where K_{ij} is the extrinsic curvature. While from this expression one could estimate ψ_4, results are rarely reported in this form. In fact, ψ_4 is usually decomposed into spin-weighted spherical harmonics, as

$$\psi_4 = \sum_{l\geq 2,|m|\leq l} \psi_4^{lm} - {}_2Y^{lm}, \tag{5.5.5}$$

where $\psi_4^{lm} = \int_{S^2}\psi_4 - {}_2\bar{Y}^{lm}d\Omega$. Einstein Toolkit code framework provides the routines to perform this decomposition and then integrates twice ψ_4^{lm} to obtain h^{lm}. We then compute the h_{22} component of the gravitational wave strain as it provides the dominant contribution to the signal.

Figure 5.18 and 5.19 show the GW signal for both models. Before the merger, indicated by the vertical dashed line, we can clearly see the inspiral waveform and its characteristic chirp (i.e. amplitude and frequency increasing with time), with the maximum amplitude corresponding to the merger. The merger exhibits a rapid decreasing in the amplitude, while the frequency keeps increasing. In fact, the post-merger signal is characterized by a single dominant frequency, above 3 kHz,

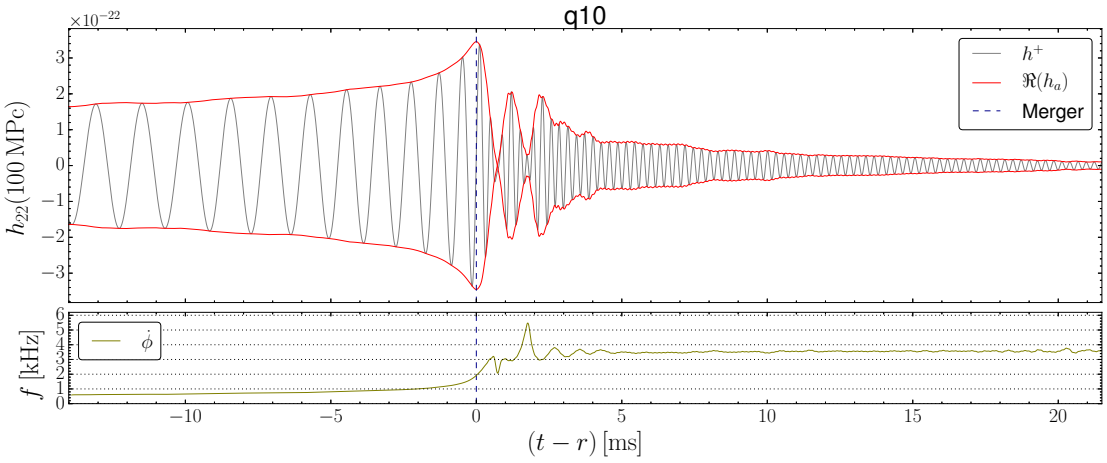

Figure 5.18: Gravitational wave signal for model q_{10}. The top panel shows the strain at a nominal distance of 100 Mpc. The lower panel shows the instantaneous frequency.

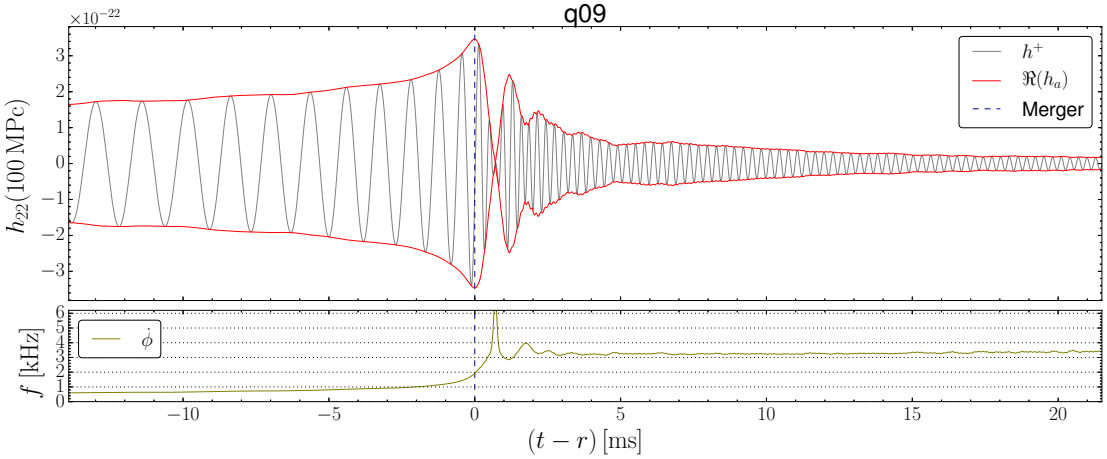

Figure 5.19: Gravitational wave signal for model q_{09}. The top panel shows the strain at a nominal distance of 100 Mpc. The lower panel shows the instantaneous frequency.

that is significantly higher than the GW frequency prior to merger. The post-merger amplitude oscillations correlate with the first, strong radial oscillations of the remnant, that can be seen in the first ~ 3 ms in the plot. Just after the merger we notice that the amplitude reaches the zero. This is due to an over-modulation of the phase that can occur during the remnant oscillations, i.e. the remnant is oscillating in shape and this induces rapid changes (jumps) in the phase of a perturbation

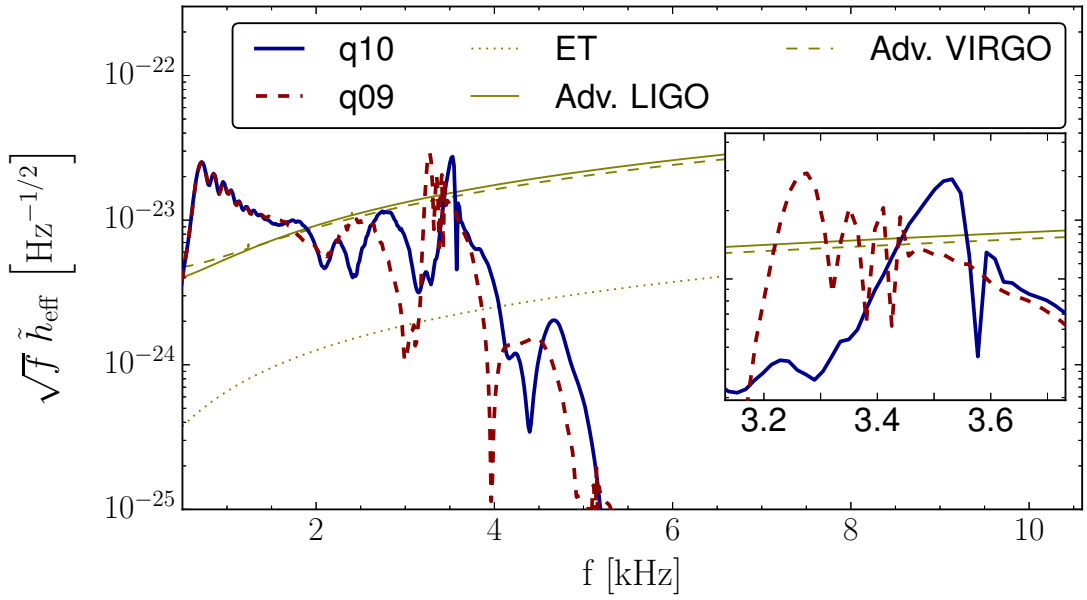

Figure 5.20: Gravitational wave spectra for both models in comparison to the design sensitivity curves of Advanced LIGO, Advanced Virgo, and ET detectors. The strain assumes a distance of 100 Mpc.

propagating on it. These jumps in turn cause a rapid change in the frequency of the signal, that can be see in the bottom row. The peaks in the frequency (or phase velocity) associated with these phase jumps are not physical, and one should take into account this effect when employing simulated signals like these as a test case for data analysis pipelines. As this is beyond the scope of this Thesis, we refer to [70] for further information on this phenomenon and on the techniques to clean up the signal.

Figure 5.20 shows the power spectrum for both models. The profile in the top left, descending from left to right, is associated with the inspiral phase and is suppressed at a certain initial frequency (< 1 kHz) simply because our simulation starts from a specific initial separation (45 km). After the merger, which happens around 2 kHz tick in this case, we note a dominant peak in the signal for both models. This post-merger peak corresponds to the characteristic oscillation frequency of the remnant, and thus carries important information about the EOS. While the dominant effect on the position of the peak is given by the EOS, we find that also the mass ratio has an impact on it.

6 Conclusions

The main purpose of this work was to investigate the binary neutron star merger event GW170817 via general relativistic magnetohydrodynamics simulations, trying to understand in particular (i) if such system can launch a short gamma-ray burst before the massive neutron star remnant has collapsed into a black hole, (ii) the role of magnetic fields in the dynamical evolution and the structure and rotational profile of the remnant, (iii) how the evolution depends on the mass ratio of the progenitor binary neutron star, which we consider either $q = 1$ (equal-mass) or $q = 0.9$. Our simulations provide extensive insights on these topics, also because we managed to explore longer timescales than previous simulations. In this section we summarize our results.

6.1 What we learned

The magnetic field evolution is rather similar for the two models. We saw that the magnetic energy exhibits a small rise in the pre-merger phase, that is almost equal for both models, even if the cause of this amplification is still under debate. The Kelvin-Helmholtz instability develops at merger, dominating the magnetic field amplification up to about 10 ms after merger. Later on, the magnetorotational instability sets in and provides further magnetic field amplification. From ~ 15 ms over, the two models showed a different evolution path for the magnetic energy. Our results seem to suggest that, due to the higher level of symmetry, the q_{10} model saturates earlier that the q_{09}. This is, however, in contrast with other simulations (e.g., [11]), in which the q_{09} saturates earlier. So we can conclude that the evolution of the magnetic field in the $15 - 40$ ms time-window is not mainly determined by the mass ratio but instead it depends on the particular case, while what is certain is that both models saturate at some point around a similar order of magnitude ($\sim 10^{51}$ erg). These energies are enough to power a relativistic outflow, but so far we had no signs of jet formation. The three-dimensional plot of the magnetic field lines in fact showed that in neither models the field acquired a coherent structure along the rotation axis, which is required to launch a jet. We also pointed out that in the q_{09} case a coherent structure is more likely to emerge on longer timescale, comparing the same time snapshots of the field lines for the two models.

Further investigations on the properties of the remnant and its surroundings after the merger indicate that the environment is baryon polluted, a condition that lowers the chances to launch a successful jet, and the velocity plot confirmed that there are no jet-like structures forming along the rotation axis. An interesting result, which overturns the common idea that a neutron star remnant will be surrounded

by an accretion disk, is that in both our simulations we start with the well known early remnant structure characterized by a torus-shaped "disk-like" outer envelope, but in a few tens of ms the remnant acquires a nearly isotropic shape, with no disk whatsoever. This excludes the possibility to power a short gamma-ray burst on longer timescales via an accretion mechanism. The magnetic-to-fluid pressure ratio plots indicate that the baryon winds in the surroundings are magnetically driven, and this is compatible with the possible explanation of the blue kilonova that was observed 11 hours after the GW170817 merger based on a fast, massive, and relatively neutron-poor ejecta component.

Finally, we showed that the mass ratio has a non negligible impact on the post-merger peak frequency in the power spectrum of the gravitational wave signal, even though the unknown equation of state could easily produce similar or larger displacements, making it impossible to distinguish the effect of the mass ratio, at least at present stage.

6.2 Outlook

Binary neutron star mergers represent the ultimate target for multi-messenger astrophysics, as they provide an extraordinary physics laboratory, and the breakthrough discovery of GW170817 paved the way for more observations of these events.

Numerical relativity simulations are the most powerful tool to unravel the dynamics of these systems and the associated mechanisms. In this Thesis we performed state-of-the-art simulations of highly magnetized binary neutron star systems evolving them on timescales that are significantly longer than most of the simulations reported in literature, and this allowed us to gain novel hints on a variety of aspects.

However, there is still ample room for improvements. For example, one could develop numerical codes to allow for initial magnetic fields extending outside the neutron stars, which represents a more realistic configuration, and perform simulations with higher resolution to better resolve and understand the different magnetic field amplification mechanisms. It would be also interesting to further evolve these systems in time to monitor the structure of the magnetic field and determine if they will be able to launch a jet. Moreover, one could perform the same simulations with different equations of state, and compare the results with our work. Finally, including the contribution of neutrinos would allow for a more precise study of the environment properties and the kilonova emission.

With the increasing sensitivity of the gravitational wave detectors and the enlargement of the network (KAGRA is about to join LIGO/Virgo), we expect a number of new multi-messenger observations of binary neutron star mergers. Therefore, the further advancement of theoretical modelling and simulations of these systems,

necessary to exploit the richness of information coming from the forthcoming detections, has never been as urgent as today.

Bibliography

[1] W. Baade and F. Zwicky. 'On Super-novae'. In: *Proceedings of the National Academy of Science* 20 (May 1934), pp. 254–259. DOI: 10.1073/pnas.20.5.254.

[2] A. Hewish et al. 'Observation of a Rapidly Pulsating Radio Source'. In: *Nature* 217 (Feb. 1968), pp. 709–713. DOI: 10.1038/217709a0.

[3] T. Gold. 'Rotating Neutron Stars as the Origin of the Pulsating Radio Sources'. In: *Nature* 218 (May 1968), pp. 731–732. DOI: 10.1038/218731a0.

[4] F. Pacini. 'Rotating Neutron Stars, Pulsars and Supernova Remnants'. In: *Nature* 219 (July 1968), pp. 145–146. DOI: 10.1038/219145a0.

[5] Richard C. Tolman. 'Static Solutions of Einstein's Field Equations for Spheres of Fluid'. In: *Physical Review* 55.4 (Feb. 1939), pp. 364–373. DOI: 10.1103/PhysRev.55.364.

[6] J. R. Oppenheimer and G. M. Volkoff. 'On Massive Neutron Cores'. In: *Physical Review* 55.4 (Feb. 1939), pp. 374–381. DOI: 10.1103/PhysRev.55.374.

[7] *Neutron stars structure*. URL: https://heasarc.gsfc.nasa.gov/Images/nicer/ (visited on 02/10/2019).

[8] D. R. Lorimer. 'Binary and Millisecond Pulsars'. In: *Living Reviews in Relativity* 11 (Nov. 2008). DOI: 10.12942/lrr-2008-8. arXiv: 0811.0762.

[9] *Gravitational wave signal waveform for coalescing binaries*. URL: https://www.soundsofspacetime.org/coalescing-binaries.html (visited on 30/09/2019).

[10] L. Baiotti and L. Rezzolla. 'Binary neutron-star mergers: a review of Einstein's richest laboratory'. In: *ArXiv e-prints* (July 2016). arXiv: 1607.03540 [gr-qc].

[11] R. Ciolfi et al. 'General relativistic magnetohydrodynamic simulations of binary neutron star mergers forming a long-lived neutron star'. In: *Physical Review D* 95.6, 063016 (Mar. 2017), p. 063016. DOI: 10.1103/PhysRevD.95.063016. arXiv: 1701.08738 [astro-ph.HE].

[12] A. Endrizzi et al. 'General relativistic magnetohydrodynamic simulations of binary neutron star mergers with the APR4 equation of state'. In: *Classical and Quantum Gravity* 33.16, 164001 (Aug. 2016), p. 164001. DOI: 10.1088/0264-9381/33/16/164001. arXiv: 1604.03445 [astro-ph.HE].

[13] W. Kastaun and F. Galeazzi. 'Properties of hypermassive neutron stars formed in mergers of spinning binaries'. In: *Physical Review D* 91.6, 064027 (Mar. 2015), p. 064027. DOI: 10.1103/PhysRevD.91.064027. arXiv: 1411.7975 [gr-qc].

[14] Charles W. Misner, Kip S. Thorne and John A. Wheeler. *Gravitation*. 1973.

[15] Sean M. Carroll. *Spacetime and geometry: An introduction to general relativity*. Cambridge University Press, 2019. ISBN: 0805387323, 9780805387322, 9781108488396, 9781108775557. URL: http://www.slac.stanford.edu/spires/find/books/www?cl=QC6:C37:2004.

[16] Alexandre Le Tiec and Jérôme Novak. 'Theory of Gravitational Waves'. In: *An Overview of Gravitational Waves* (Feb. 2017), pp. 1–41. DOI: 10.1142/9789813141766_0001. URL: http://dx.doi.org/10.1142/9789813141766_0001.

[17] *Gravitational wave from inspiral phase*. URL: http://www.ligo.org/science/GW-Overview/images/inspiral.jpg (visited on 10/04/2019).

[18] A. I. MacFadyen, S. E. Woosley and A. Heger. 'Supernovae, Jets, and Collapsars'. In: *The Astrophysical Journal* 550.1 (Mar. 2001), pp. 410–425. ISSN: 1538-4357. DOI: 10.1086/319698. URL: http://dx.doi.org/10.1086/319698.

[19] J. S. Bloom et al. 'The Host Galaxy of GRB 970508'. In: *The Astrophysical Journal* 507.1 (Nov. 1998), pp. L25–L28. ISSN: 0004-637X. DOI: 10.1086/311682. URL: http://dx.doi.org/10.1086/311682.

[20] A. S. Fruchter et al. 'Long γ-ray bursts and core-collapse supernovae have different environments'. In: *Nature* 441.7092 (May 2006), pp. 463–468. ISSN: 1476-4687. DOI: 10.1038/nature04787. URL: http://dx.doi.org/10.1038/nature04787.

[21] T. J. Galama et al. 'An unusual supernova in the error box of the γ-ray burst of 25 April 1998'. In: *Nature* 395.6703 (Oct. 1998), pp. 670–672. ISSN: 1476-4687. DOI: 10.1038/27150. URL: http://dx.doi.org/10.1038/27150.

[22] Ramesh Narayan, Bohdan Paczynski and Tsvi Piran. 'Gamma-ray bursts as the death throes of massive binary stars'. In: *The Astrophysical Journal* 395 (Aug. 1992), p. L83. ISSN: 1538-4357. DOI: 10.1086/186493. URL: http://dx.doi.org/10.1086/186493.

[23] E. Berger. 'Short-Duration Gamma-Ray Bursts'. In: *ARA&A* 52 (Aug. 2014), pp. 43–105. DOI: 10.1146/annurev-astro-081913-035926. arXiv: 1311.2603 [astro-ph.HE].

[24] N. R. Tanvir et al. 'A 'kilonova' associated with the short-duration γ-ray burst GRB 130603B'. In: *Nature* 500 (Aug. 2013), pp. 547–549. DOI: 10.1038/nature12505. arXiv: 1306.4971 [astro-ph.HE].

[25] E. Berger, W. Fong and R. Chornock. 'An r-process Kilonova Associated with the Short-hard GRB 130603B'. In: *The Astrophysical Journal Letters* 774, L23 (Sept. 2013), p. L23. DOI: 10.1088/2041-8205/774/2/L23. arXiv: 1306.3960 [astro-ph.HE].

[26] D. Eichler et al. 'Nucleosynthesis, neutrino bursts and gamma-rays from coalescing neutron stars'. In: *Nature* 340 (July 1989), pp. 126–128. DOI: 10.1038/340126a0.

[27] J. M. Lattimer and D. N. Schramm. 'Black-hole-neutron-star collisions'. In: *The Astrophysical Journal Letters* 192 (Sept. 1974), pp. L145–L147. DOI: 10.1086/181612.

[28] J. M. Lattimer et al. 'The decompression of cold neutron star matter'. In: *The Astrophysical Journal* 213 (Apr. 1977), pp. 225–233. DOI: 10.1086/155148.

[29] Li-Xin Li and Bohdan Paczyński. 'Transient events from neutron star mergers'. In: *The Astrophysical Journal Letters* 507.1 (1998), p. L59.

[30] Roger D Blandford and Roman L Znajek. 'Electromagnetic extraction of energy from Kerr black holes'. In: *Monthly Notices of the Royal Astronomical Society* 179.3 (1977), pp. 433–456.

[31] Oliver Just et al. 'Neutron-star merger ejecta as obstacles to neutrino-powered jets of gamma-ray bursts'. In: *The Astrophysical Journal Letters* 816.2 (2016), p. L30.

[32] Albino Perego, Hannah Yasin and Almudena Arcones. 'Neutrino pair annihilation above merger remnants: implications of a long-lived massive neutron star'. In: *Journal of Physics G: Nuclear and Particle Physics* 44.8 (2017), p. 084007.

[33] Kip S Thorne et al. *Black holes: the membrane paradigm*. Yale university press, 1986.

[34] M. Ruiz et al. 'Binary Neutron Star Mergers: A Jet Engine for Short Gamma-Ray Bursts'. In: *The Astrophysical Journal Letters* 824, L6 (June 2016), p. L6. DOI: 10.3847/2041-8205/824/1/L6. arXiv: 1604.02455 [astro-ph.HE].

[35] N. Gehrels et al. 'The Swift Gamma-Ray Burst Mission'. In: *The Astrophysical Journal* 611.2 (2004), p. 1005. URL: http://stacks.iop.org/0004-637X/611/i=2/a=1005.

[36] Riccardo Ciolfi and Daniel M. Siegel. 'Short Gamma-Ray Bursts in the "Time-reversal" Scenario'. In: *The Astrophysical Journal Letters* 798.2 (2015), p. L36. URL: http://stacks.iop.org/2041-8205/798/i=2/a=L36.

[37] Brian D. Metzger. *Kilonovae*. 2019. arXiv: 1910.01617 [astro-ph.HE].

[38] Benjamin P Abbott et al. 'GW170817: observation of gravitational waves from a binary neutron star inspiral'. In: *Physical Review Letters* 119.16 (2017), p. 161101.

[39] B. P. Abbott et al. 'Properties of the Binary Neutron Star Merger GW170817'. In: *Physical Review X* 9.1 (Jan. 2019). ISSN: 2160-3308. DOI: 10.1103/physrevx.9.011001. URL: http://dx.doi.org/10.1103/PhysRevX.9.011001.

[40] B. P. Abbott et al. 'GW170817: Measurements of Neutron Star Radii and Equation of State'. In: *Physical Review Letters* 121.16, 161101 (Oct. 2018), p. 161101. DOI: 10.1103/PhysRevLett.121.161101. arXiv: 1805.11581 [gr-qc].

[41] BP Abbott et al. 'LIGO Scientific and Virgo and Fermi-GBM and INTEGRAL Collaborations'. In: *Astrophys. J* 848.2 (2017), p. L13.

[42] Riccardo Ciolfi. 'Short gamma-ray burst central engines'. In: *International Journal of Modern Physics D* 27.13, 1842004 (Jan. 2018), p. 1842004. DOI: 10.1142/S021827181842004X. arXiv: 1804.03684 [astro-ph.HE].

[43] K. P. Mooley et al. 'Superluminal motion of a relativistic jet in the neutron-star merger GW170817'. In: *Nature* 561.7723 (Sept. 2018), pp. 355–359. ISSN: 1476-4687. DOI: 10.1038/s41586-018-0486-3. URL: http://dx.doi.org/10.1038/s41586-018-0486-3.

[44] G. Ghirlanda et al. 'Compact radio emission indicates a structured jet was produced by a binary neutron star merger'. In: *Science* 363.6430 (Feb. 2019), pp. 968–971. ISSN: 1095-9203. DOI: 10.1126/science.aau8815. URL: http://dx.doi.org/10.1126/science.aau8815.

[45] E. Pian et al. 'Spectroscopic identification of r-process nucleosynthesis in a double neutron-star merger'. In: *Nature* 551.7678 (Oct. 2017), pp. 67–70. ISSN: 1476-4687. DOI: 10.1038/nature24298. URL: http://dx.doi.org/10.1038/nature24298.

[46] Brian D. Metzger, Todd A. Thompson and Eliot Quataert. 'A Magnetar Origin for the Kilonova Ejecta in GW170817'. In: *The Astrophysical Journal* 856.2 (Mar. 2018), p. 101. ISSN: 1538-4357. DOI: 10.3847/1538-4357/aab095. URL: http://dx.doi.org/10.3847/1538-4357/aab095.

[47] Daniel M. Siegel. *GW170817–the first observed neutron star merger and its kilonova: implications for the astrophysical site of the r-process*. 2019. arXiv: 1901.09044 [astro-ph.HE].

[48] Luciano Rezzolla and Olindo Zanotti. *Relativistic Hydrodynamics*. 2013.

[49] Carles Bona et al. 'New Formalism for Numerical Relativity'. In: *Physical Review Letters* 75.4 (July 1995), pp. 600–603. DOI: 10.1103/PhysRevLett.75.600. arXiv: gr-qc/9412071 [gr-qc].

[50] Miguel Alcubierre et al. 'Gauge conditions for long-term numerical black hole evolutions without excision'. In: *Physical Review D* 67.8, 084023 (Apr. 2003), p. 084023. DOI: 10.1103/PhysRevD.67.084023. arXiv: gr-qc/0206072 [gr-qc].

[51] J. R. Wilson. 'Numerical Study of Fluid Flow in a Kerr Space'. In: *The Astrophysical Journal* 173 (Apr. 1972), p. 431. DOI: 10.1086/151434.

[52] Jose Maria Martí and Ewald Müller. 'Numerical Hydrodynamics in Special Relativity'. In: *Living Reviews in Relativity* 2.1, 3 (Dec. 1999), p. 3. DOI: 10.12942/lrr-1999-3. arXiv: astro-ph/9906333 [astro-ph].

[53] R. Courant and K. O. Friedrichs. *Supersonic flow and shock waves*. 1948.

[54] José Ma. Martí, José Ma. Ibáez and Juan A. Miralles. 'Numerical relativistic hydrodynamics: Local characteristic approach'. In: *Physical Review D* 43.12 (June 1991), pp. 3794–3801. DOI: 10.1103/PhysRevD.43.3794.

[55] Luca Baiotti et al. 'A new three-dimensional general-relativistic hydrodynamics code'. In: *arXiv e-prints*, arXiv:1004.3849 (Apr. 2010), arXiv:1004.3849. arXiv: 1004.3849 [gr-qc].

[56] Thomas W. Baumgarte and Stuart L. Shapiro. *Numerical Relativity: Solving Einstein's Equations on the Computer*. 2010.

[57] Bruno Giacomazzo and Luciano Rezzolla. 'WhiskyMHD: a new numerical code for general relativistic magnetohydrodynamics'. In: *Classical and Quantum Gravity* 24.12 (June 2007), S235–S258. ISSN: 1361-6382. DOI: 10.1088/0264-9381/24/12/s16. URL: http://dx.doi.org/10.1088/0264-9381/24/12/S16.

[58] Robert D. Richtmyer and K. W. Morton. *Difference methods for initial-value problems*. 1994.

[59] S. K. Godunov. 'A difference method for numerical calculation of discontinuous solutions of the equations of hydrodynamics.' Russian. In: *Mat. Sb., Nov. Ser.* 47 (1959), pp. 271–306.

[60] Amiram Harten, Peter Lax and Bram van Leer. 'On Upstream Differencing and Godunov-Type Schemes for Hyperbolic Conservation Laws'. In: *SIAM Rev* 25 (Jan. 1983), pp. 35–61.

[61] Bernd Einfeldt. 'On Godunov-Type Methods for Gas Dynamics'. In: *Siam Journal on Numerical Analysis - SIAM J NUMER ANAL* 25 (Apr. 1988), pp. 294–318. DOI: 10.1137/0725021.

[62] A. Akmal, V. R. Pandharipande and D. G. Ravenhall. 'Equation of state of nucleon matter and neutron star structure'. In: *Physical Review C* 58.3 (Sept. 1998), pp. 1804–1828. ISSN: 1089-490X. DOI: 10.1103/physrevc.58.1804. URL: http://dx.doi.org/10.1103/PhysRevC.58.1804.

[63] Jocelyn S. Read et al. 'Constraints on a phenomenologically parametrized neutron-star equation of state'. In: *Physical Review D* 79.12 (June 2009). ISSN: 1550-2368. DOI: 10.1103/physrevd.79.124032. URL: http://dx.doi.org/10.1103/PhysRevD.79.124032.

[64] Riccardo Ciolfi et al. 'First 100 ms of a long-lived magnetized neutron star formed in a binary neutron star merger'. In: *Physical Review D* 100.2 (July 2019). ISSN: 2470-0029. DOI: 10.1103/physrevd.100.023005. URL: http://dx.doi.org/10.1103/PhysRevD.100.023005.

[65] Kenta Hotokezaka et al. 'Mass ejection from the merger of binary neutron stars'. In: *Physical Review D* 87.2 (Jan. 2013). ISSN: 1550-2368. DOI: 10.1103/physrevd.87.024001. URL: http://dx.doi.org/10.1103/PhysRevD.87.024001.

[66] Kenta Kiuchi et al. 'Efficient magnetic-field amplification due to the Kelvin-Helmholtz instability in binary neutron star mergers'. In: *Physical Review D* 92.12 (Dec. 2015). ISSN: 1550-2368. DOI: 10.1103/physrevd.92.124034. URL: http://dx.doi.org/10.1103/PhysRevD.92.124034.

[67] Albino Perego, Sebastiano Bernuzzi and David Radice. 'Thermodynamics conditions of matter in neutron star mergers'. In: *The European Physical Journal A* 55.8 (Aug. 2019). ISSN: 1434-601X. DOI: 10.1140/epja/i2019-12810-7. URL: http://dx.doi.org/10.1140/epja/i2019-12810-7.

[68] Nigel T. Bishop and Luciano Rezzolla. 'Extraction of gravitational waves in numerical relativity'. In: *Living Reviews in Relativity* 19.1, 2 (Oct. 2016), p. 2. DOI: 10.1007/s41114-016-0001-9. arXiv: 1606.02532 [gr-qc].

[69] Frank Löffler et al. 'The Einstein Toolkit: a community computational infrastructure for relativistic astrophysics'. In: *Classical and Quantum Gravity* 29.11 (May 2012), p. 115001. ISSN: 1361-6382. DOI: 10.1088/0264-9381/29/11/115001. URL: http://dx.doi.org/10.1088/0264-9381/29/11/115001.

[70] W. Kastaun et al. 'Structure of stable binary neutron star merger remnants: Role of initial spin'. In: *Physical Review D* 96.4 (Aug. 2017). ISSN: 2470-0029. DOI: 10.1103/physrevd.96.043019. URL: http://dx.doi.org/10.1103/PhysRevD.96.043019.